Università Degli Studi Di Catania
Dipartimento Di Scienze Fisiche Ed Astronomiche

Dottorato di Ricerca in Fisica – Ciclo XXXI

Ph.D. Thesis

Coupled Molecular Dynamics and Finite Element Methods for the simulation of interacting particles and fields

Ph.D. Student: Michele Cascio

Tutor: Prof. Giuseppe Falci

Co-tutor: Dott. Antonino La Magna

Coordinator: Prof. Vincenzo Bellini

ANNO ACCADEMICO 2017- 2018

Index

List of abbreviations pag. 1

Preface pag. 3

Chap. 1 Electromagnetic forces on dielectric particles immersed in a dielectric medium pag. 9

1.1 Force on an electric dipole pag. 10

1.2 Effective moment of a dielectric particle pag. 12

1.3 Standard Dielectrophoretic force pag. 14
1.3.1 Application potential of DEP pag. 17
1.3.2 Clausius-Mossotti factor and Standard DEP force pag. 21
1.3.3 Velocity field induced by DEP force pag. 22

1.4 DEP force calculated by the Maxwell Stress Tensor pag. 25

1.5 Remarks pag. 31

Chap. 2 Many pareticles thoeries of the electromechanical systems pag. 32

2.1 Mean field approach to many e.mec. particles kinetics pag. 33
2.1.1 Detrapping effects pag. 35
2.1.2 Cluster formation pag. 41

2.2 Analysis of stable configurations of e.mec. systems pag. 49
2.2.1 Monte Carlo study of the static configurations pag. 49
2.2.2 MST calculations of forces in few particles systems pag. 55

2.3 Conclusions pag. 58

Chap.3 The variational approach for the numerical solution of Partial Differential Equations pag. 60

3.1 Partial Differential Equations pag. 61

3.2 Boundaries value problems pag. 62
3.2.1 Boundary problem for the Poisson equation pag. 63

3.3 Variational method pag. 66
3.3.1 Solution of Laplace's problem by variational method pag. 70

3.4 FEM approximation pag. 73
3.4.1 Galerkin Method of FEM approximation pag. 74

3.5 FEniCS project, Gmsh, Salome pag. 75
3.5.1 FEniCS project pag. 75
3.5.2 Gmsh pag. 77
3.5.3 Salome pag. 78

3.6 Remarks pag. 80

Chap. 4 Coupled Molecular Dynamics-Finite Element Method algorithm pag. 81

4.1 Molecular Dynamics pag. 82
4.1.1 MD implementation pag. 83

4.2 Verlet integration pag. 86
4.2.1 Basic Verlet integration pag. 87

4.2.2 Velocity Verlet algorithm pag. 89

4.3 MD-FEM algorithm pag. 92

4.4 Conclusions pag. 97

Chap. 5 Simulated evolution of EMPs' systems pag. 98

5.1 Single particle external interactions pag. 100

5.2 Particle Model pag. 104

5.3 Model validation for simple configurations pag. 108

5.4 MD-FEM simulation results in many particle systems pag. 113
5.4.1 Case (a): MDA-MD-231 cells pag. 116
5.4.2 Case (b): two cells system MDA-MB-231 and B-Lymphocites pag. 127

5.5 Geometry's effects pag. 134
5.5.1 Case (c): MDA-MD-231 cells pag. 134
5.5.2 Case (b): two cells system MDA-MB-231 and B-Lymphocites pag. 136

5.6 Conclusions pag. 138

Chap. 6 Generalization of the MD-FEM formalism for particles of generic shape pag. 140

6.1 Rigid-body dynamics pag.140

6.2 Quaternions pag. 142
6.2.1 Algebra of quaternions pag. 144
6.2.2 Unit quaternions and rotations pag. 145

6.3 Rotational Velocity Verlet pag. 147

6.4 Control instruction in simulations of rotational motion of non-spherical particles pag. 150

6.4.1 Overlap between particles pag. 151

Conclusions pag. 154

Appendix A. Field due to a finite dipole pag. 157

Appendix B. Effective dipole moment of a dielectric particle pag. 160

Appendix C. Circulating Tumoral Cells and microfluidics technology pag. 164

C.1 Circulating Tumoral Cells pag. 164

C.1.1 Metsastasis pag. 165

C.1.2 CTCs analysis as a “liquid biopsy” pag 167

C.1.3 CTCs in breast cancer patients. MDA-MB – 231 cell line pag. 169

C.1.4 Techniques of CTCs isolation pag. 170

C.2 Microfluidics Technology pag. 173

Appendix D. Particle model pag. 178

Appendix E.MD-FEM code details pag. 182

E.1 Mesh generation pag. 182

E.2 Finite elements and Funcion Space generation pag. 183

E.3 Boundary conditions pag. 184

E.4 Solution of Laplace'problem pag. 185

E.5 Control instructions pag. 186
E.5.1 Particle-wall interaction pag. 186
E.5.2 Overlapping between particles pag. 187

Appendix F. Re$\{f_{CM}\}$ of MDA-MB231 cells and Lymphocites pag. 190

References pag. 194

List of pubblications and conference participations pag. 212

Acknowledgements pag. 216

List of abbreviations

AC	alternating current
CM	Clausius-Mossotti
CTCs	Circulating Tumor Cells
DC	direct current
DEP	dielectrophoresis
e.mec.	electromechanical
e.m	electromagnetic
EMPs	Electromechanical Particles
FEM	Finite Element Method
LOC	Lab-On-a-Chip
MC	Monte Carlo
MEMS	Micro Electro-Mechanical Systems
MD	Molecular Dynamics
MD-FEM	Molecular Dynamics - Finite Element Method
MST	Maxell Stress Tensor
n-DEP	negative - DEP
p-DEP	positive - DEP
μTAS	Micro Total Analysis Systems

Preface

The dynamical simulation of many particle systems is currently a widespread technique in many fields: e.g. nuclear and atomic physics, computational materials science, computational chemistry, molecular biology and pharmacology. Under the locution “Molecular Dynamics” (MD) we can regroup a variety of approaches and numerical codes, whereas the commonalities are: 1) the atomistic (or nuclear) resolution (i.e. particles are atoms or nucleons), 2) the force derivation, starting from the systems’ configuration, through semi-classical (also called semi-empirical) or quantum mechanics based theoretical frameworks, 3) the (generally explicit) numerical integration of the Newton-like equations of motion to simulate the system kinetics. Within this scheme methodology variations can be found in the literature, but it is undoubtedly valid to qualify the MD meaning in the field of the scientific computation.

The general scope of this Thesis work is the extension of the MD methods to the study of the kinetics of larger particles (i.e. from mesoscopic dimensions and above), where effective particle-particle interactions are mediated by **a field evolving self-consistently with the many particles system**. This objective is mainly motivated by the applications of the method to control and predict the manipulation of mesoscopic (electrically) neutral particles by means of electromagnetic (e.m.) interactions: i.e. exploiting the so called dielectrophoresis (DEP) phenomena in the systems of electromechanical particles (EMPs). This is the specific case of study

here considered, but in principle the methodology can applied after suitable adaptation to also other systems.

In the particular case of the DEP driven systems, which will be briefly introduced in the following, we believe that our modelling approach satisfies the requirement of the general accurate prediction of the kinetics evolution; whilst previous theoretical approaches have several limitations which limit the applicability only under particular conditions.

Applications of DEP range from bio-structure assembling [1, 2] and nanostructure deposition (e.g. nanocluster, nanowires or nanotube) [3] to filtering systems [4]. A branch of emerging applications is related to the controlled manipulation of micro and nano-sized particles dispersed in colloidal solutions (i.e. biological particles such as cells or DNA), since the strong selectivity of the response depends on the particle volume, shape and composition [5, 6]. In fact, the forces exerted by non-uniform AC electric fields, due to the frequency dependent responses, can be used to move and manipulate polarizable microparticles (such as cells, marker particles, etc.) suspended in liquid media. The DEP allows manipulation of suspended particles without direct contact: this is also significant for many applications in micro Total-Analysis Systems (μTAS) technology [7]. Manipulation includes cell partitioning/isolation [8] for the capture/separation without the use of biomarkers: in fact, cells can be collected, concentrated, separated and transported using the DEP forces arising from microelectrode structures having dimensions of the order of 1 to 100 μm [5]. One of the core strengths of DEP is therefore that the characterization of different cells depending only on the dielectric properties controlled by the particle's individual phenotype; hence, the process does not require specific tags or involve

chemical reactions. The DEP based on AC electro-kinetics has recently been given more attention in microfluidics [9] due to the development of novel microfabrication techniques. In a typical device for the capture/separation of cells, the non-uniform field for the generation of the DEP force, responsible for the particle's manipulation and control, is imposed by microelectrodes patterned on substrates (typically of glass) using fabrication techniques borrowed from Micro-Electro-Mechanical Systems (MEMS) [7]. The electric field is applied through the electrodes present in a microfluidic channel and the fluid flows through it.

As we will discuss in detail in Chapter 1, direct and rather straightforward numerical solutions of EMPs' kinetics can be obtained when the following approximations (which we can indicate as *single particle approximation*) are considered: a) diluted limit (i.e. negligible effective particle-particle interactions), b) point-like particles (i.e. neglecting steric interactions), c) large distance between the particles and the source of the electric field (electrodes). This theory could be used to estimate roughly the EMPs' [10, 11, 12]; however, in many real conditions these approximations are not verified and DEP is an example of field mediated force which can in principle induce a complex many particle behavior. Indeed, the forces acting on the particles depend in the general case on the overall system configuration since polarization alters locally the field which can be barely approximated by the external field generated by the sources. As a consequence, predictive theoretical studies of this large class of systems could be only possible thanks to the development of real-system models and numerical simulations. In order to study EMPs beyond the single particle approximation, computational studies of the DEP driven systems in

particular conditions have been recently presented in the scientific literature and they will be briefly presented in Chapter 2. In particular: stable configurations of particles dispersed in a static fluid [13] have been determined using Monte Carlo methods [14]; numerical models and simulations of the movement of cells in a moving fluid within a microfluidic channel introducing many-particle effects in the mean field approximation [15, 16] have been derived; finally, exact calculations of the forces by means of commercial tools [17] in the few-particles case have been reported.

Our contribution [18] aims to fully overcoming the single particle approximation, focusing on the theoretical study (see Chapters 4, 5 and appendices for the formalization of the method) of the dynamics of EMPs suspended in a colloidal solution in the presence of a non-uniform variable electric field. Our numerical simulations of a three-dimensional (3D) model system aim at providing predictions of both stable configurations of the particles and their dynamics in fully three-dimensional configurations, minimizing the approximations usually considered in models of mutual interactions. As a case of study, presented in Chapter 5, a system has been chosen consisting of biological cells dispersed in a colloidal solution (of which the typical characteristics of interest are reported in the literature) that flows into a microfluidic channel in the presence of e.m. fields.

3D simulations of DEP phenomena are rather rare in the literature, as they require large computational resources; moreover, most 3D DEP models are based on particles in the already discussed diluted solution limit. Nevertheless, in real applications, particle manipulation and characterization using dielectrophoresis are generally performed in a confined region close to

the electrodes, so that the interaction between the particles and the surrounding walls can be significant. Here we run a detailed study, with a non-approximate calculation of the forces, which are estimated by integrating the Maxwell Stress Tensor over the surfaces of the particles [19]. The dynamics are simulated by techniques borrowed from *Molecular Dynamics* (MD), which, as stated above, is a simulation method that has been successfully applied in the atomistic simulation field [20], whilst the *Finite Element Method* (FEM) is applied to obtain self-consistent numerical solutions of the partial differential equations regarding the e.m. field. The Coupled MD-FEM algorithm and its implementation in the FEniCS environment are also presented in the theoretical sections. The examples of the method's application will focus on DEP induced translation of spherical particles (in particular a dielectric model of: MDA-MB-231 tumor cells, B-Lymphocites and mixtures of them), however after suitable adaptation it can be applied in more general cases (i.e. non-spherical particles, roto-translation, mixed DEP and conventional electrophoresis).

After validation of the FEniCS developer team, the numerical code simulating EMPs kinetics by means the cited coupled MD-FEM methodology is distributed as an open source tool at the web page:

https://bitbucket.org/barolidavide/tumor_detection_dolfin/src/master/.

Open source distribution is possible thanks to the use of supporting frameworks (namely: FEniCS [21] for the PDE solutions, Gmsh [22] for the meshing and Salome for the graphical analysis) which are covered by GPL and/or LGPL licenses. The main modules are: a) the MD related routines, b)

the interface with Gmsh for the automatic meshing of the system configurations, c) the FEniCS interface for the force evaluation. The modules have been implemented from the scratch in the Python language while parallelization of the code has been obtained in an MPI environment.

Chapter 1

Electromagnetic forces on dielectric particles immersed in a dielectric medium

Particles with sizes that range from sub-micrometers to about one millimeter and with particular electrical and/or magnetic properties experience mechanical forces and torques when they are subjected to electromagnetic (e.m.) fields. Particles of this type are called "electromechanical particles" (EMPs) [23]. Mutual interactions between EMPs could also occur when they are close enough to modify the force field obtained in the isolated particle limit.

One of the phenomena that affect electromechanical (e.mec.) particles is the "*dielectrophoresis*" (DEP), which describes the force exerted by a non-uniform electric field on polarizable neutral particles [23]: in a uniform electric field, neutral particles experience the polarization (an electric dipole is induced) which does not cause acceleration, whereas in a non-uniform electric field the forces due to polarization are not balanced and motion occurs: the net force is directed towards areas with either a higher or a lower electric field intensity, depending on the polarization properties of the particle and the background medium. Herbert Pohl's first scientific publication defines DEP as "the natural movement of neutral bodies caused by polarization in an uneven electric field" [24].

In this chapter we will resume the theory of the e.m. forces deriving some concepts and expressions used in the next chapters. The following

themes will be presented: the formulation for the electromagnetic force acting on an electric dipole immersed in an external electric field, the concept of the effective dipole moment of a polarized particle, the standard (approximate) dielectrophoretic force acting on a particle and the more accurate dielectrophoretic force calculated by the use of the Maxwell Stress Tensor.

1.1 Force on an electric dipole

A finite dipole consists in two-point charges $+q$ and $-q$ separated by a vector distance $\boldsymbol{d}$. In the limit where $|\boldsymbol{d}| \to 0$ and $q \to \infty$ such that the qd product remains finite, the point dipole is defined. We consider in the following discussion a dipole with a finite spacing between the two charges, immersed in a non-uniform electric field $\mathbf{E}(\boldsymbol{r})$ which includes no contributions due to the dipole itself. The dipole moment is defined as follows:

$$\mathbf{p} = q\boldsymbol{d}. \tag{1.1}$$

In general, the two charges experience different values of force and the dipole will be subject to a net force equal to:

$$\mathbf{F} = q\mathbf{E}(\boldsymbol{r} + \boldsymbol{d}) - q\mathbf{E}(\boldsymbol{r}), \tag{1.2}$$

where $\boldsymbol{r}$ is the position vector of the charge –q. Figure 1 shows this case.

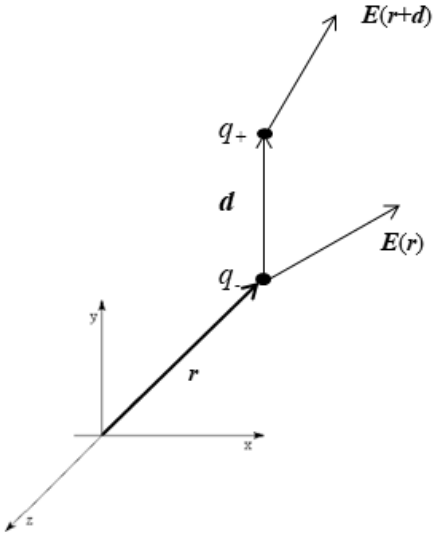

Fig. 1.1 A small dipole in a non-uniform electric field.

If $|\boldsymbol{d}|$ is small compared to the characteristic dimension of the electric field nonuniformity, $\mathbf{E}$ can be expanded about position $\boldsymbol{r}$ using the Taylor series expansion:

$$\mathbf{E}(\boldsymbol{r}+\boldsymbol{d}) = \mathbf{E}(\boldsymbol{r}) + \boldsymbol{d}\cdot\nabla\mathbf{E}(\boldsymbol{r}) + \cdots \tag{1.3}$$

By replacing Eq. (1.3) in Eq. (1.2):

$$\mathbf{F} = q[\boldsymbol{d}\cdot\nabla]\mathbf{E}(\boldsymbol{r}) + \cdots \tag{1.4}$$

In the limit $|\boldsymbol{d}| \to 0$ but such that $\mathbf{p}$ remains finite, neglecting terms of the order greater than the first and substituting the definition of Eq. (1.1) in Eq. (1.4), the force on a dipole results:

$$\mathbf{F}_{dip} = [\mathbf{p} \cdot \nabla]\mathbf{E}(\boldsymbol{r}). \tag{1.5}$$

The dipole therefore experiences a net force only if the external imposed electric field is non-uniform. Eq. (1.5) represents an approximation for the force exerted on any physical dipole, such as a polarized particle of finite size. The approximation used is called *dielectrophoretic approximation* [23].

1.2 Effective moment of a dielectric particle

In the derivation of Eq. (1.5), no reference is made to the nature of the dipole moment $\mathbf{p}$, which can be the permanent moment of a polar particle or might be induced in a particle by an imposed electric field. In this Thesis, the latter case is considered. In general, the moment-induced field depends on both externally imposed and mutual field contributions (due to the presence of other particles).

The moment must relate to the electric field and to the particle parameters so that it can be used in Eq. (1.5). It is fundamental to identify the correct expression for the dipole moment to be used in formulation for the force (Eq. (1.5)) in the case of polarized particle. It is consequently useful to introduce the concept of *effective dipole moment*, p_{eff}. The effective dipole moment of a dielectric particle immersed in a medium is

defined as the moment of an equivalent, free-charge point dipole that causes the same dipolar electrostatic potential if it is immersed in the same medium and occupies the same position as the center of the particle.

The electrical potential Φ_{dip}, due to a finite dipole centered in the origin of a Cartesian reference system and aligned with the z axis, immersed in a linear dielectric medium of permittivity ε_m, in the point with coordinates (r, ϑ), radial and polar respectively, assumes the following form (see Appendix A):

$$\Phi_{dip}(r, \vartheta) = \frac{qd\cos\vartheta}{4\pi\varepsilon_m r^2}\,. \tag{1.6}$$

As a consequence, the formula of the electric potential produced by the polarized dielectric particle will contain the effective moment instead of the term qd:

$$\Phi(r, \vartheta) = \frac{p_{eff}\cos\vartheta}{4\pi\varepsilon_m r^2}. \tag{1.7}$$

The expression of p_{eff} for the case of a spherical particle is presented below. Consider an isolated homogeneous dielectric particle of radius R, permittivity ε_p and conductivity σ_p, immersed in a dielectric fluid medium of permittivity ε_m and conductivity σ_m. The particle and the medium are therefore characterised by the ohmic conductivity with no dielectric loss.

The calculated potential of the sphere can be expressed in the form of Eq. (1.7); and indicating with **E** the electric field in which the dipole is immersed, the effective moment is (see Appendix B):

$$\mathbf{p}_{eff} = 4\pi\varepsilon_m f_{CM} R^3 \mathbf{E}, \tag{1.8}$$

where

$$f_{CM} = \frac{\tilde{\varepsilon}_p - \tilde{\varepsilon}_m}{\tilde{\varepsilon}_p + 2\tilde{\varepsilon}_m} \tag{1.9}$$

is the so-called Clausius-Mossotti factor, which contains the complex dielectric constants of the particle and of the medium, defined as it follows (see Appendix B):

$$\tilde{\varepsilon}_m = \varepsilon_m - i\frac{\sigma_m}{\omega}, \tag{1.10.a}$$

$$\tilde{\varepsilon}_p = \varepsilon_p - i\frac{\sigma_p}{\omega}. \tag{1.10.b}$$

f_{CM} is therefore a complex quantity, dependent on the angular frequency ω.

1.3 Standard Dielectrophoretic force

The discussion carried out in the previous sections reveals implications for the so-called ponderomotive force exerted by a non-uniform electric field upon dielectric materials.

It is assumed that the motion of EMPs is induced by a sinusoidally time-varying and non-uniform electric field and consequently exponential notation can be used [25]:

$$\mathbf{E}(\boldsymbol{r},t) = \mathrm{Re}\left\{\mathbf{E}(\boldsymbol{r})e^{-i\omega t}\right\}. \tag{1.11}$$

By replacing in Eq. (1.5) $\mathbf{p}$ with $\mathbf{p}_{eff}$ and $\mathbf{E}(\boldsymbol{r})$ with the expression of the electric field of Eq. (1.11), the time dependent force acting on the dielectric particle, called *Standard DEP force* and here indicated with $\boldsymbol{F}^{STD}$, is obtained:

$$\boldsymbol{F}^{STD} = \left[\mathbf{p}_{eff}\cdot\nabla\right]\mathbf{E}(\boldsymbol{r},t). \tag{1.12}$$

This force consists of a constant average component and a time-varying term. The latter term is usually damped because of the viscosity of the suspension medium in the cases of particles with size in the range from 1 to 1000 μm. Consequently, the only relevant term is the one averaged over time. Starting from the previous equation, this term can be written [1]:

$$\langle\boldsymbol{F}^{STD}\rangle = \frac{1}{2}\mathrm{Re}\left\{\left[\mathbf{p}_{eff}\cdot\nabla\right]\mathbf{E}^{*}(\boldsymbol{r})\right\} \tag{1.13}$$

where $\langle\ \ \rangle$ indicates the time-average and the asterisk indicates the complex conjugation. By inserting Eq. (1.8) in Eq. (1.13), using the vector identity:

$$\nabla\cdot(\mathbf{A}\cdot\mathbf{B}) = (\mathbf{A}\cdot\nabla)\mathbf{B} + (\mathbf{B}\cdot\nabla)\mathbf{A} + \mathbf{B}\wedge(\nabla\wedge\mathbf{A}) + \mathbf{A}\wedge(\nabla\wedge\mathbf{B})$$

and the condition $\nabla \wedge \mathbf{E} = 0$ (irrotationality of the field $\mathbf{E}$), the force assumes the form:

$$\langle \boldsymbol{F}^{STD} \rangle = 2\pi\varepsilon_m \mathrm{Re}\{f_{CM}\} R^3 \nabla(|\mathbf{E}_{RMS}|^2), \qquad (1.14)$$

where $\mathbf{E}_{RMS}$ is the root mean square of electric field.
The Eq. (1.14) predicts the fundamental phenomenology of dielectrophoresis relative to spherical dielectric particles. The following are the main characteristics of the dielectrophoretic force acting on a lossless dielectric spherical particle immersed in a lossless medium:

- the intensity of $\langle \boldsymbol{F}^{STD} \rangle$ is proportional to particle volume, ε_m, $\mathrm{Re}\{f_{CM}\}$ and $\nabla(|\mathbf{E}_{RMS}|^2)$;

- the sign of $\langle \boldsymbol{F}^{STD} \rangle$ depends upon the sign of $\mathrm{Re}\{f_{CM}\}$;

- depending on $\mathrm{Re}\{f_{CM}\}$, by Eq.s (1.9), (1.10a) and (1.10b) it follows that $\langle \boldsymbol{F}^{STD} \rangle$ depends on the frequency;

- particles experience a DEP force only when the electric field is non-uniform;

- $\langle \boldsymbol{F}^{STD} \rangle$ does not depend on the polarity of the electric field and is observed with AC as well as DC excitation;

- the $\langle \boldsymbol{F}^{STD} \rangle$ vector is directed along $\nabla(|\mathbf{E}_{RMS}|^2)$ and therefore can have any orientation with respect to the electric field vector;

- DEP is usually observed for particles with diameters ranging from approximately 1 to 1000 μm.

1.3.1 Application potential of DEP

$\langle \mathbf{F}^{\mathrm{STD}} \rangle$ depends on the shape and size of the particle, the intensity and frequency of the oscillating electric field and the dielectric properties of the particle and medium. A distinction can be made between *positive dielectrophoresis* (p-DEP) and *negative dielectrophoresis* (n-DEP), defined as follows:

a) p-DEP: $\mathrm{Re}\{f_{CM}\} > 0$, particles are attracted toward the electric field intensity maxima and repelled from the minima;

b) n-DEP: $\mathrm{Re}\{f_{CM}\} < 0$, particles are attracted toward electric field intensity minima and repelled from the maxima.

$\mathrm{Re}\{\mathrm{f_{CM}}\}$ represents the effects of the arrangement of electrical charges, depending on the permittivity and conductivity values of the particle and the medium. Phenomenology is explained as follows. When a particle is suspended in a medium (typically an electrolyte) in the presence of an

electric field, the charges inside the particle and inside the medium will be redistributed at the particle-medium interface depending on their polarizability. Two cases can be distinguished, corresponding to the previous definitions a) and b) respectively:

A) the polarizability of the particle is higher than that of the medium: an excess of charge will accumulate at the particle's side;

B) the polarizability of the medium is higher than that of the particle: an excess of charge will accumulate at the medium's side.

In both cases, the resulting charge distribution is non-uniform and involves a difference in the charge density on either side of the particle. An induced dipole across the particle, aligned with the applied electric field, is therefore generated. When the particle-medium system is in the presence of a non-uniform electric field, the particle feels different forces at each end. Figure 1.2 shows this situation in an example where a pair of electrodes of different shape generates a non-uniform electric field. The difference in force at both ends generates a net force with direction depending on the polarizability of the particle and the medium.

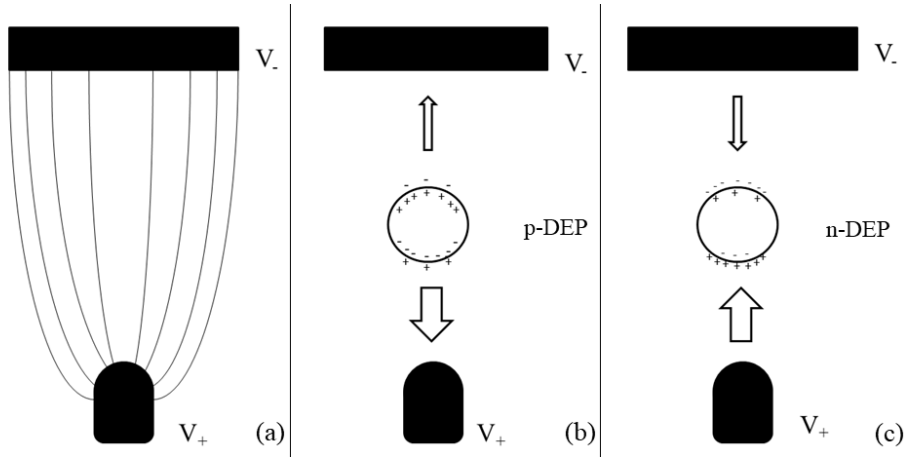

Fig. 1.2 (a): Field lines of a non-uniform electric field generated by a pair of electrodes with different shape. (b) and (c): Dielectric particle in a medium in the presence of the non-uniform electric field (the field lines are not shown); the arrows indicate the forces acting on the charge distributions; the width of the arrows indicates the intensity of the forces; qualitative electric charge arrangements at the particle-medium interface are shown. In (b) the dielectric parameters of the particle and the medium result in $\mathrm{Re}\{f_{CM}\} > 0$ and the electric charge arrangement generates p-DEP, with a net force directed towards the electric field intensity maxima. In the case (c) instead $\mathrm{Re}\{f_{CM}\} < 0$ and n-DEP is generated, with a net force directed towards the electric field intensity minima.

Due to all its characteristics, the DEP force allows the control and manipulation of particles of micrometric size dispersed in colloidal solutions. It is very remarkable, for practical applications, the ability of DEP to induce both negative and positive forces. Thanks to this prerogative, the DEP force allows the separation of particles: in sorting operation mode, when two types of particles are present, the frequency can be chosen for the capturing and separations so as one cell type experiences n-DEP moving away from the electrodes, and the second type experiences p-DEP, moving towards the electrodes, as can be seen in Eq. (1.14).

As will be seen in Chap. 5, the control/separation by DEP of particles dispersed in a liquid medium will be the subject of computational studies in this Thesis.

1.3.2 Clausius-Mossotti factor and Standard DEP force

In this next section, further considerations on the link between f_{CM} and $\langle \boldsymbol{F}^{STD} \rangle$ are given.

The explicit form of the Clausius-Mossotti factor is:

$$f_{CM} = \frac{\tilde{\varepsilon}_p - \tilde{\varepsilon}_m}{\tilde{\varepsilon}_p + 2\tilde{\varepsilon}_m} = \frac{\varepsilon_p - \varepsilon_m - i\frac{\sigma_p - \sigma_m}{\omega}}{\varepsilon_p + 2\varepsilon_m - i\frac{\sigma_p + 2\sigma_m}{\omega}}. \tag{1.15a}$$

The real and imaginary parts are:

$$\mathrm{Re}\{f_{CM}\} = \mathrm{Re}\left\{\frac{\tilde{\varepsilon}_p - \tilde{\varepsilon}_m}{\tilde{\varepsilon}_p + 2\tilde{\varepsilon}_m}\right\} = \frac{(\varepsilon_p - \varepsilon_m)(\varepsilon_p + 2\varepsilon_m) - \frac{1}{\omega^2}(\sigma_m - \sigma_p)(\sigma_p + 2\sigma_m)}{(\varepsilon_p + 2\varepsilon_m)^2 + \frac{1}{\omega^2}(\sigma_p + 2\sigma_m)^2}, \tag{1.15b}$$

$$\mathrm{Im}\{f_{CM}\} = \mathrm{Im}\left\{\frac{\tilde{\varepsilon}_p - \tilde{\varepsilon}_m}{\tilde{\varepsilon}_p + 2\tilde{\varepsilon}_m}\right\} = \frac{(\sigma_m - \sigma_p)(\varepsilon_p + 2\varepsilon_m) - \frac{1}{\omega}(\varepsilon_p - \varepsilon_m)(\sigma_p + 2\sigma_m)}{(\varepsilon_p + 2\varepsilon_m)^2 + \frac{1}{\omega^2}(\sigma_p + 2\sigma_m)^2}. \tag{1.15c}$$

It was seen by Eq. (1.14) that the sign of the time-average DEP force direction depends on the sign of $\mathrm{Re}\{f_{CM}\}$, which contains all frequency dependence of the force. The frequency value at which $\mathrm{Re}\{f_{CM}\}$ becomes zero is called the *crossover frequency,* ν_c. By varying the frequency and exceeding this value, the force changes sign and the DEP response switches between n-DEP and p-DEP (or between p-DEP and n-DEP). From Eq. (1.15b), it can be seen that its form is:

$$\nu_c = \frac{1}{2\pi}\sqrt{\frac{(\sigma_m-\sigma_p)(\sigma_p+2\sigma_m)}{(\varepsilon_p-\varepsilon_m)(\varepsilon_p+2\varepsilon_m)}}. \quad (1.16)$$

The high- and low-frequency limits for $\mathrm{Re}\{f_{CM}\}$ are:

$$\lim_{\omega\to\infty} \mathrm{Re}\{f_{CM}\} = \frac{\varepsilon_p-\varepsilon_m}{\varepsilon_p+2\varepsilon_m}, \quad (1.17a)$$

$$\lim_{\omega\to 0} \mathrm{Re}\{f_{CM}\} = \frac{\sigma_p-\sigma_m}{\sigma_p+2\sigma_m}. \quad (1.17b)$$

From these expressions for the limits, it can be seen that DC conduction governs the low-frequency DEP behaviour, and dielectric polarization governs the high-frequency one. These conditions will be referred in Chap. 2.

1.3.3 Velocity field induced by the DEP force

Particles in colloidal solution in a liquid medium, which move under the action of the DEP force, undergo the effect of the drag force stemming from the viscosity of the medium. For a spherical object of radius *R*, in the case of a static fluid, the drag force is given by [26]:

$$\boldsymbol{F}_{drag} = 6\pi\eta R\boldsymbol{v}, \quad (1.18)$$

where η is the dynamic viscosity and $\boldsymbol{v}$ is the instantaneous velocity of the particle. Eq. (1.18) is referred as the Stokes law [27].

Assuming the validity of the single particle approximation, which is valid when the particles are far away from each other and from the electric field sources, it is possible to obtain each particle's velocity field induced by DEP, here indicated by $\boldsymbol{v}_{DEP}$. The DEP force is counterbalanced by the drag force due to the liquid if each particle subjected to the DEP force reaches very quickly a steady regime of motion [28] and, as a result, the electric and fluid components are completely uncoupled. By replacing $\boldsymbol{v}$ with $\boldsymbol{v}_{DEP}$ in Eq. (1.18) and equating with the dielectrophoretic force of Eq. (1.14):

$$2\pi\varepsilon_m \mathrm{Re}\{f_{CM}\} R^3 \nabla(|\mathbf{E}_{RMS}|^2) = 6\pi\eta R \boldsymbol{v}_{DEP},$$

the following expression for the velocity field is obtained:

$$\boldsymbol{v}_{DEP} = \frac{\varepsilon_m R^2 \mathrm{Re}\{f_{CM}\}}{3\eta} \nabla(|\mathbf{E}|^2) = \mu_{DEP} \nabla(|\mathbf{E}|^2), \tag{1.19}$$

where

$$\mu_{DEP} = \frac{\varepsilon_m R^2 \mathrm{Re}\{f_{CM}\}}{3\eta} \tag{1.20}$$

is the so-called "*DEP mobility*".
In the case of a moving fluid, $\boldsymbol{v}$ in Eq. (1.18) must be replaced with $\boldsymbol{u} - \boldsymbol{v}$, being $\boldsymbol{u}$ the local velocity of the fluid.

In DEP applications, microfluidic devices equipped with electrodes are often used (see Fig. 1.3 for a schematic from Ref. [6], while additional details on this type of device will be presented in Chapter 5) and the

expressions here derived are used to numerically evaluate an approximate kinetics of these systems of EMPs. Indeed, the velocity field of Eq. (1.19) can be determined by the numerical solution of the electric field equation and used to derive the trajectories of suspended particles, as shown in the example of Fig. 1.4 (from the Ref. [28]).

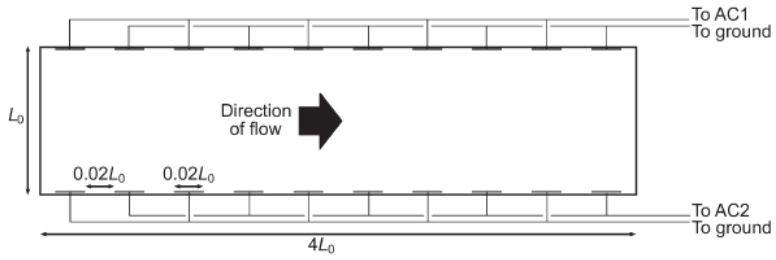

Fig. 1.2 Schematic of the model system of the DEP device. (Figure taken from: F. Aldaeus, Y. Lin, J. Roeraade, and G. Amberg, Electrophoresis **26**, 2005).

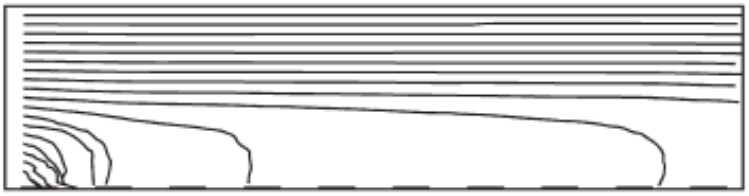

Fig. 1.3 Particle trajectories in a medium liquid in the device operating in p-DEP condition only at the bottom of the channel. (Figure taken from: F. Aldaeus, Y. Lin, J. Roeraade, and G. Amberg, Electrophoresis **26**, 2005).

1.4 DEP force calculated by the Maxwell Stress Tensor

The term “dielectrophoresis” is commonly used (and probably not correctly) to indicate two types of forces [23]:

- the forces exerted upon individual noninteracting particles by an externally imposed nonuniform electric field;

- the mutual attractive or repulsive force between two or more closely spaced particles.

The two types are basically related but distinctively observable. The first type of forces was the subject of the previous sections, while the second one will be detailed below.

In the models based on particles in the diluted solution limit (isolated particles), the first order dipole approximation, on which the Eq. (1.14) is based, is reasonable. This limit is valid in the case where particle-particle and particle-electrode interactions can be neglected (i.e. isolated particles). However, particle manipulation and characterization using DEP is generally performed in a confined region where particles accumulate and mutual forces occur, for example close to the electrodes of a Lab-on-chip device (See Appendix C.2). Including the mutual interactions in the definition of dielectrophoresis is therefore very important. For these reasons, an accurate approach for calculating the DEP forces is necessary: it is based on the rigorous application of the Maxwell Stress Tensor (MST, here and after indicated by $\overline{\overline{T}}$), that is described below.

The momentum change of a volume V of a dielectric inside an e.m. field can be correctly expressed as a surface integral of $\bar{\bar{T}}$ [25]:

$$\frac{d}{dt}(\boldsymbol{P}_{mass} + \boldsymbol{P}_{field}) = \oint_{\Omega} \bar{\bar{T}} \cdot \hat{n} d\Omega, \tag{1.21}$$

where $\boldsymbol{P}_{mass}$ is the momentum of the mass contained in volume V, $\boldsymbol{P}_{field}$ is the total e.m. momentum of the field, Ω is the surface enclosing volume V and $\hat{n}$ is the unit vector normal to Ω. According the e.m. field theory, the MST is given by the following general expression [29]:

$$\bar{\bar{T}} = \frac{1}{2}[\mathbf{E} \otimes \mathbf{D} + \mathbf{D} \otimes \mathbf{E} + \mathbf{B} \otimes \mathbf{H} + \mathbf{H} \otimes \mathbf{B} - (\mathbf{E} \cdot \mathbf{D} + \mathbf{B} \cdot \mathbf{H})\mathbf{I}], \tag{1.22}$$

where **E** is the electric field, **D** is the electric displacement, **H** is the magnetic field, **B** is the magnetic induction, **I** is the unit tensor. Products with dot are scalar products, whereas the symbol $\otimes$ indicates a dyadic tensor product of vectors.

In this Thesis, the interest is focused on practical dielectrophoretic applications, where the applied external e.m. field generally has a frequency below 100 MHz and the correspondent field wave has a wavelength of the order of meters. This wavelength is much larger than dimensions of typical DEP arrangements. As a consequence, the contribution of the magnetic field can be neglected (near field approximation) and Eq. (1.22) becomes:

$$\bar{\bar{T}} = \frac{1}{2}[\mathbf{E} \otimes \mathbf{D} + \mathbf{D} \otimes \mathbf{E} - (\mathbf{E} \cdot \mathbf{D})\mathbf{I}]. \tag{1.23}$$

If non-ferroelectric materials compose the EMPs, a linear dependence between **D** and **E** is valid and Eq. (1.23) becomes [30]:

$$\bar{\bar{T}} = \mathrm{Re}\{\tilde{\varepsilon}_m\}[\mathbf{E} \otimes \mathbf{E} - \tfrac{1}{2}(\mathbf{E} \cdot \mathbf{E})\mathbf{I}] \,, \tag{1.24}$$

where $\tilde{\varepsilon}_m$ is the complex permittivity of the medium (see Eq. (1.10a)).
The harmonic non-uniform electric field can be written [25]:

$$\mathbf{E}(\mathbf{r},t) = \mathrm{Re}\{\mathbf{E}(\mathbf{r})e^{-i\omega t}\} \equiv \tfrac{1}{2}\left[\mathbf{E}(\mathbf{r})e^{-i\omega t} + \mathbf{E}^*(\mathbf{r})e^{i\omega t}\right]. \tag{1.25}$$

By replacing Eq. (1.25) in Eq. (1.24) and tacking the time average:

$$\langle\bar{\bar{T}}\rangle = \frac{1}{2\pi}\int_0^{2\pi} \bar{\bar{T}}\; d(\omega t) =$$
$$= \tfrac{1}{4}\mathrm{Re}\{\tilde{\varepsilon}_m\}[\mathbf{E}(\mathbf{r}) \otimes \mathbf{E}^*(\mathbf{r}) + \mathbf{E}^*(\mathbf{r}) \otimes \mathbf{E}(\mathbf{r}) - |\mathbf{E}(\mathbf{r})|^2\,\mathbf{I}]. \tag{1.26}$$

By expressing in explicit form the dyadic products and the square module, Eq. (1.26) becomes:

$$\langle\bar{\bar{T}}\rangle =$$
$$\tfrac{1}{4}\mathrm{Re}\{\tilde{\varepsilon}_m\}\begin{pmatrix} E_x^*E_x - E_yE_y^* - E_zE_z^* & E_xE_y^* + E_x^*E_y & E_xE_z^* + E_x^*E_z \\ E_yE_x^* + E_y^*E_x & E_y^*E_y - E_xE_x^* - E_zE_z^* & E_yE_z^* + E_y^*E_z \\ E_zE_x^* + E_z^*E_x & E_zE_y^* + E_z^*E_y & E_z^*E_z - E_xE_x^* - E_yE_y^* \end{pmatrix}. \tag{1.27}$$

From Eq. (1.21) it is noted that by integrating the MST over a surface external to the particle and infinitesimally close to it, we obtain the field-induced force acting on the particle itself (as the change of the moment

relative to the field is excluded). Therefore, if now we indicate with Ω this particular surface, the time-averaged electromechanical force exerted on a particle immersed in a medium with complex permittivity $\tilde{\varepsilon}_m$ and subject to sinusoidal electric field **E** is [31, 32, 33]:

$$\langle \boldsymbol{F}^{MST} \rangle = \oiint_{\Omega} \langle \bar{\bar{T}} \rangle \cdot \hat{n} d\Omega. \tag{1.28}$$

To identify the normal vector $\hat{n}$ present in Eq. (1.28), the cosine directors are calculated using the following formulas:

$$\cos(\widehat{rx}) = \frac{x - x_c}{\sqrt{(x-x_c)^2 + (y-y_c)^2 + (z-z_c)^2}},$$

$$\cos(\widehat{ry}) = \frac{y - y_c}{\sqrt{(x-x_c)^2 + (y-y_c)^2 + (z-z_c)^2}},$$

$$\cos(\widehat{rz}) = \frac{z - z_c}{\sqrt{(x-x_c)^2 + (y-y_c)^2 + (z-z_c)^2}}.$$

From Eq. (1.28), the time-averaged DEP force exerted on the particle can therefore be written:

$$\langle \boldsymbol{F}^{MST} \rangle = \begin{pmatrix} \langle F_x^{MST} \rangle \\ \langle F_y^{MST} \rangle \\ \langle F_z^{MST} \rangle \end{pmatrix} = \oiint_{\Omega} \langle \bar{\bar{T}} \rangle \cdot \hat{n} d\Omega =$$

$$= \frac{1}{4} \mathrm{Re}\{\tilde{\varepsilon}_m\} \oiint_{\Omega} \begin{pmatrix} E_x^* E_x - E_y E_y^* - E_z E_z^* & E_x E_y^* + E_x^* E_y & E_x E_z^* + E_x^* E_z \\ E_y E_x^* + E_y^* E_x & E_y^* E_y - E_x E_x^* - E_z E_z^* & E_y E_z^* + E_y^* E_z \\ E_z E_x^* + E_z^* E_x & E_z E_y^* + E_z^* E_y & E_z^* E_z - E_x E_x^* - E_y E_y^* \end{pmatrix} \cdot \begin{pmatrix} \cos(\widehat{rx}) \\ \cos(\widehat{ry}) \\ \cos(\widehat{rz}) \end{pmatrix} d\Omega \tag{1.29}$$

The use of $\langle \boldsymbol{F}^{MST} \rangle$, instead of $\langle \boldsymbol{F}^{STD} \rangle$, allows the correct description in the proximity of the electrodes when the particle-particle e.mec. interactions cannot be neglected due to the relatively large local density of EMPs. The usefulness of the calculation based on the MST consists also in its better applicability, compared with the dipole approximation method, to cases of objects with irregular shapes, such as nanowires, nanobelts etc.

The discussion presented for the calculation of $\langle \boldsymbol{F}^{MST} \rangle$ can be extended to the calculation of the time-averaged value of the torque, here indicated by $\langle \boldsymbol{T}^{MST} \rangle$. By indicating with $\boldsymbol{r}$ a vector connecting the reference axis to the particle surface, the expression of the torque is:

$$\langle \boldsymbol{T}^{MST} \rangle = \begin{pmatrix} \langle \boldsymbol{T}_x^{MST} \rangle \\ \langle \boldsymbol{T}_y^{MST} \rangle \\ \langle \boldsymbol{T}_z^{MST} \rangle \end{pmatrix} = \oiint_{\Omega} \boldsymbol{r} \times \langle \bar{\bar{T}} \rangle \cdot \hat{n} d\Omega =$$

$$\frac{1}{4}\mathrm{Re}\{\tilde{\varepsilon}_m\} \oiint_{\Omega} \boldsymbol{r} \times \begin{pmatrix} E_x^* E_x - E_y E_y^* - E_z E_z^* & E_x E_y^* + E_x^* E_y & E_x E_z^* + E_x^* E_z \\ E_y E_x^* + E_y^* E_x & E_y^* E_y - E_x E_x^* - E_z E_z^* & E_y E_z^* + E_y^* E_z \\ E_z E_x^* + E_z^* E_x & E_z E_y^* + E_z^* E_y & E_z^* E_z - E_x E_x^* - E_y E_y^* \end{pmatrix} \cdot \begin{pmatrix} \cos(\widehat{\vec{r}x}) \\ \cos(\widehat{\vec{r}y}) \\ \cos(\widehat{\vec{r}z}) \end{pmatrix} d\Omega. \quad (1.30)$$

As it can be seen from Eq. (1.29) and Eq. (1.30), the calculation of the e.mec. force and torque requires the solution of the electric field, which in the case of practical dielectrophoretic applications derives from an applied electrical potential to the electrodes. In order to evaluate the electric field, the complex Laplace equation must therefore be solved. Again, the potential applied is time-varying and harmonic:

$$\mathrm{V}(\mathbf{r},\mathrm{t}) = \mathrm{V}(\mathbf{r})e^{i\omega t} \tag{1.31}$$

and the complex Laplace equation to be resolved is [34]:

$$\nabla \cdot [\tilde{\varepsilon}\, \nabla\, \mathrm{V}(\mathbf{r})] = 0. \tag{1.32}$$

In Eq. (1.32), consider $\tilde{\varepsilon} = \tilde{\varepsilon}_m$ inside the liquid medium and $\tilde{\varepsilon} = \tilde{\varepsilon}_p$ inside the particles.

This equation is based on some assumptions: particle neutrality (negligible ion effect), harmonic oscillation (linear model) and negligible convection effects [35]. Moreover, as stated, the coupling of electric and magnetic fields can be neglected ($\nabla \times \mathbf{E} = -\frac{\partial \mathbf{B}}{\partial t} = 0$) and in this framework we can derive the electric field simply as a gradient of the electrical potential:

$$\mathbf{E}(\mathbf{r}) = -\nabla\, \mathrm{V}(\mathbf{r}). \tag{1.33}$$

1.5 Remarks

In this section we resume the formalism needed to evaluate (eventually using numerical methods) the force and torques in EMPs. We notice that for a spherical particle, the direct use of these expressions allows for a relatively simple derivation of the kinetics in diluted systems of EMPs. Anyhow, beyond the single particle approximation, such derivation could be strongly inaccurate. In the next chapter we present the state of the art (as it emerged at the beginning of the present Thesis work) of the theoretical/computational approaches for the study of many particle effects in a system of EMPs.

Chapter 2

Many-particle theories of electromechanical systems

In this chapter we will briefly discuss the current state-of-the-art of the theoretical approaches to the study of many-particle effects in dielectrophoretic systems in order to discuss some limitations which we intend to overcome with our methodology. Firstly, we present the approaches in the continuum limit where particles are approximated as density fields. In this case, the multiparticle effects are highlighted by means of a medium field approach, while the formation of particle chains is analyzed according to reaction-diffusion models. Such approaches are independent of the calculation of the dielectrophoretic force.

The second part is dedicated to the more accurate particle-like description of the EMPs where, in turn, the limitations are related to the pure static configuration studied both with approximate dipole-dipole interactions and with the use of the Maxwell Stress Tensor for the derivation of the forces.

2.1 Mean field approach to many e.mec. particle kinetics

In dielectrophoretic devices, many-particle effects can arise due to the high concentration of particles in the surroundings of electrodes. This constitutes a substantial source of indetermination on the theoretical estimate of the trapping/separation efficiency when single particle solutions are used (see Section 1.3). An approximated method to include many-particle effects in the calculation of DEP trapping has been suggested [36], which is based on the Effective Medium Approximation (EMA) for electric parameters of the suspension [37].

As discussed in Chpt. 1, the Clausius–Mossotti factor (called also DEP spectrum) for a particle immersed in a medium is:

$$f_{CM} = \frac{\tilde{\varepsilon}_p - \tilde{\varepsilon}_m}{\tilde{\varepsilon}_p + 2\tilde{\varepsilon}_m}. \qquad (2.1)$$

If the local particle density is high, the dipole-dipole particle interaction can significantly vary the DEP response [38] and consequently, the form of f_{CM}. The mean field method consists on the correction of f_{CM}, taking into account the many-particle effects as alteration of the medium complex dielectric. The correction is based on the EMA for the dielectric properties of heterogeneous two-component composite materials [15]. This approach allows calculating the electrical conductivity σ and the permittivity ε for various shapes of composite materials as a function of the hosted material (ε_2, σ_2) and the host material (ε_1, σ_1) properties. It is assumed that material 2 is included by a random formation of spherical clusters in a liquid

medium. The subscript p instead of 2 and m instead of 1 are used. The dielectric function is given by [15]:

$$\varepsilon(\varphi) = \frac{1}{4}\left[2\varepsilon_v - \varepsilon_v' + \sqrt{\left(2\varepsilon_p - \varepsilon_p'\right)^2 + 8\varepsilon_m\varepsilon_p}\right], \tag{2.2}$$

with

$$\varepsilon_v = (1-\varphi)\varepsilon_m + \varepsilon_p\varphi, \tag{2.3a}$$

$$\varepsilon_v' = \varepsilon_m\varphi + (1-\varphi)\varepsilon_p. \tag{2.3b}$$

where φ represents the volume fractions of cluster inclusions. The modification of f_{CM} (Eq. (2.1)) to include the EMA consists simply in these substitutions:

$$\varepsilon_m \rightarrow \varepsilon(\varphi), \tag{2.4}$$

$$\sigma_m \rightarrow \sigma(\varphi), \tag{2.5}$$

In this way, the electrical properties of the mixture, composed of particles and liquid medium, are determined as a function of the volume fraction.
The DEP mobility, defined in Eq. (1.20), becomes:

$$\mu_{DEP} = \frac{\varepsilon(\varphi)R^2\mathrm{Re}\{f_{CM}\}}{3\eta}. \tag{2.6}$$

Figure 2.1 shows an example of a DEP spectrum obtained from experimental data on latex microspheres given in Ref. [39]:

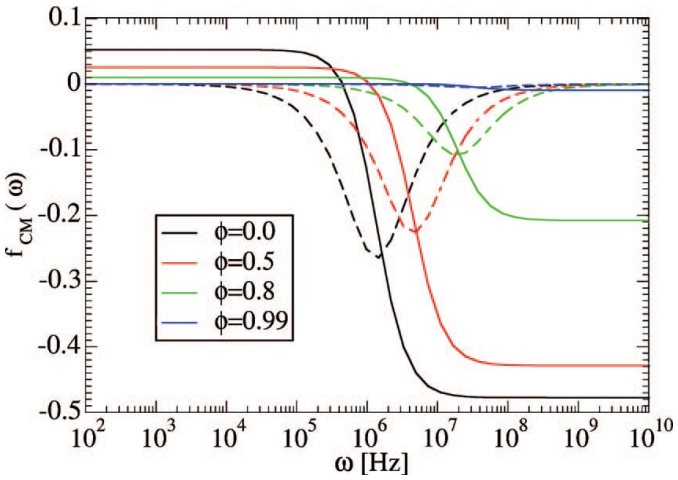

Fig. 2.1 DEP spectrum of latex microspheres obtained from data given in Ref. [4]. Straight and dashed lines refer to the real and imaginary parts of the Clausius–Mossotti factor, respectively. (Figure taken from: O. E. Nicotra, A. La Magna, and S. Coffa, Appl. Phys. Lett. 93, 193902 (2008)).

The effect of EMA in the DEP spectrum is clear: both real and imaginary parts of the f_{CM} flat to zero as the volume fraction approaches to one.

2.1.1 Detrapping effects

The mean field approach allows the use of the same computational strategy of the single particle case presented in Chpt. 1. As a consequence, the electric potential $\mathrm{V}(\mathbf{r})$ must be computed by solving the Laplace equation:

$$\nabla \cdot [\tilde{\varepsilon}\, \nabla\, \mathrm{V}(\mathbf{r})] = 0. \qquad (2.7)$$

In a standard DEP simulation, the vector composition of the liquid medium velocity field $\boldsymbol{u}_m$ with the particle's velocity field $\boldsymbol{v}_{DEP}$ gives all information on the particle motion inside the DEP device, allowing to predict particle trajectories. $\boldsymbol{u}_m$ is derived by the Navier–Stokes equation for a steady and uncompressible fluid [40]. The total velocity field is:

$$\boldsymbol{u}_{tot} = \boldsymbol{v}_{DEP} + \boldsymbol{u}_m. \tag{2.8}$$

$\boldsymbol{u}_{tot}$ acts as a drift toward the electrodes and particles may therefore be represented by a drift-diffusion current $\boldsymbol{J}$, as follows:

$$\boldsymbol{J} = -D\nabla\varphi + \boldsymbol{u}_{tot}\,\varphi. \tag{2.9}$$

In the diluted limit and for particles' dimensions in the micrometer scale, D has the meaning of a numerical diffusion, introduced to stabilize the calculation, while for the high density case, D can also effectively include the scattering event between particles or the limit threshold of φ for the packing. In order to prevent φ exceeding the threshold value for the packing fraction of 0.74, a diffusion coefficient $D(\varphi)$ was introduced:

$$D(\varphi) = \frac{D_0}{\sqrt{1-\frac{\varphi}{0.74}}}, \tag{2.10}$$

where D_0 is a constant value to be fixed in order to take into account the diffusion due to particles crowding, especially at a high particle concentration regime.

The equation governing the time evolution of φ has a flux-conservative form:

$$\frac{\partial \varphi}{\partial t} = -\nabla \cdot \boldsymbol{J}. \qquad (2.11)$$

The set of Eqs (2.1)-(2.7) and (2.11) represent the governing equations to be solved. In this way, the local value of the volume fraction of dispersed particles is adjusted by drift-diffusion dynamics.

In Ref. [28] simulations were performed on a model with a particular geometry. The device modeled consists of a two-dimensional trap with an array of parallel interdigitated electrodes present at the base of a rectangular channel where the liquid medium flows. A schematic of the device, already presented in Section 1.3.3, is shown in Fig. 2.2.

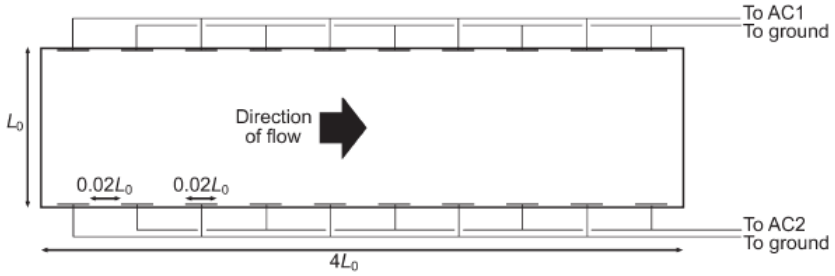

Fig. 2.2 Schematic of the model system. (Figure taken from: F. Aldaeus, Y. Lin, J. Roeraade, and G. Amberg, Electrophoresis **26**, 2005).

Spherical latex particles were considered, with radius R=5.87 μm and the following dielectric constant and conductivity:

$\varepsilon_p = 2.4\varepsilon_0$,

$\sigma_p = 7.0\ S/m^2$.

The liquid medium has the following specifications:

$\varepsilon_m = 78\varepsilon_0$,

$\sigma_m = 6.0\ S/m^2$,

$\eta = 10^{-3}\ Pa \cdot sec$.

The angular frequency is 10 KHz, $\varphi = 0.3$ and $D_0 = 9.6\ 10^{-9}\ m^2/s$.
Figure 2.3 shows some snapshots of the solution at different values of time. The color field represents φ while red lines represent a set of particle trajectories which depart from the left side of the device. Electrodes (in number of 10) are taken at a voltage of 0 or +5 V in an alternate sequence.

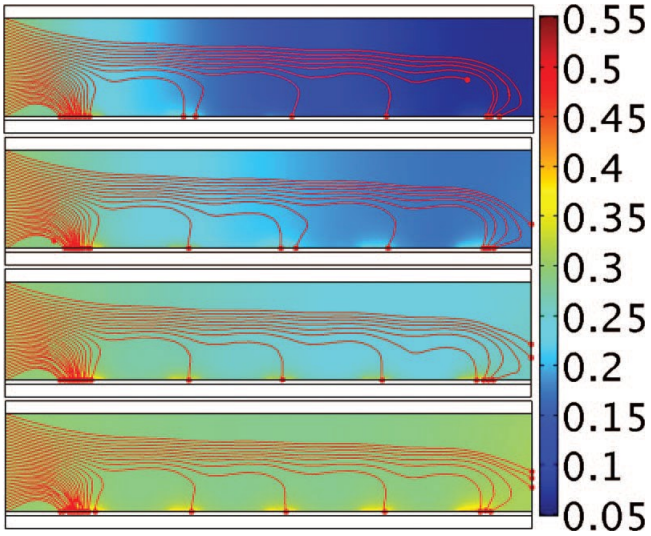

Fig. 2.3 Snapshots taken at times 1, 2, 3, and 4 s (from upper to lower) regarding the time evolution of particle volume fraction φ (color field) and particle trajectories (red lines). The vertical color bar provides the correspondence between colors and values of φ. Particles and fluid enter from the left, where at the boundary φ is fixed to 0.3, with initial fluid velocity of $15\,\mu m$. In the other boundaries the condition $\hat{n} \cdot \boldsymbol{J} = 0$ for Eq. (2.11) is assigned. (Figure taken from: O. E. Nicotra, A. La Magna, and S. Coffa, Appl. Phys. Lett. 93, 193902 (2008)).

As visible in the topmost part of Fig. 2.3, a complete trapping of the particles is predicted by the calculation when many-particle effects are neglected. Nevertheless, the self-consistency of the solution implies the change of the predicted trajectories of the particles. Indeed, as observed in the lowermost part of the same figure, the self-consistent solution indicates that some particle trajectories step away from the device. It is important to note that the many-particle effect is described by the real part of f_{CM}: in particular, it diminishes as φ increases. In this condition, the many-particle effect in trapping efficiency becomes non-negligible. Furthermore, as described in Fig. 2.4, showing a small region around one electrode, the

trapping capabilities of the device is significantly reduced when the particle fraction surrounding the electrodes increases.

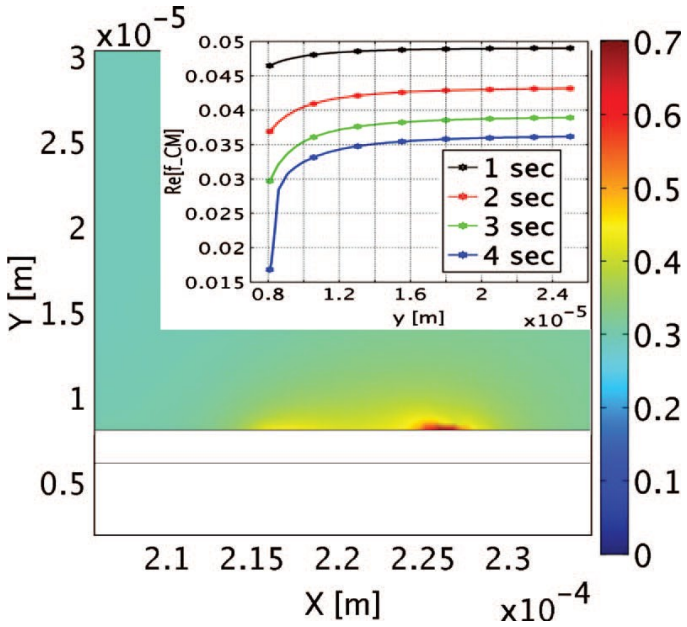

Fig. 2.4. An enlarged portion of snapshot at t=4 s of Fig. 2.3. The color field represents the particle volume fraction φ at the surroundings of an electrode where φ reaches its maximum value. Abscissa and ordinate are spatial coordinates. In the inner panel, the cross-section (taken just above the red region at $x = 2.26\ 10^{-4}\ m$) of the Clausius–Mossotti factor as a function of the ordinate is shown. Colors of the curves refer to the same times of the snapshots of Fig. 2.3. (Figure taken from: O. E. Nicotra, A. La Magna, and S. Coffa, Appl. Phys. Lett. 93, 193902 (2008)).

This aspect highlights the mutual influence between φ and the DEP spectrum as evidenced in the inset of the figure showing the dependence of f_{CM} on the y-coordinate near the electrode. As highlighted by these results, the influence of the many-particle effects on the features of DEP-based devices can be suitably investigated by combining EMA and drift-diffusion.

As discussed by the authors in Ref. [15], the many-particle correction is a fundamental tool to obtain reliable simulation outcomes in the prediction of trapping efficiency in the case of micro- and nanosized particles. This methodological approach is necessary when a high density of particles occurs near the electrode. This situation is rather common since high particle concentration can be achieved in device architectures where tight regions are designed to properly tailor the electric field [41].

2.1.2 Cluster formation

The diffusion formalism can be easily generalized to a reaction diffusion, as discussed in the following. In real systems with a large number of particles, the main effect of the induced electric dipole is the formation of particle clusters, particularly in the shape of chains of very different length, that align with the electric field (longitudinal chaining for identical particles) [42]. The clusters have different dielectrophoretic properties from those of their constituents: this is an aspect to be considered for the accurate description of the dielectrophoresis. In reference [43] it has been shown that particle-chain formation and evolution can be quantitatively described in a realistic device geometry. In this discussion, chains composed of no more than four particles are considered, however the approach followed can be easily generalized to a larger number of particles.
As seen in Chapter 1, the time-averaged force acting on a dipole in the presence of a non-uniform electric field

$$\mathbf{E}(\mathbf{r},t) = \mathbf{E}(\mathbf{r})e^{-i\omega t}$$

is:

$$\langle \boldsymbol{F}_{DEP}(t) \rangle = 2\pi\varepsilon_m \mathrm{Re}\{f_{CM}\} R^3 \nabla(|\mathbf{E}_{RMS}|^2) \qquad (2.12)$$

where $\mathbf{E}_{RMS} = \mathbf{E}(\mathbf{r})/\sqrt{2}$ is the root mean square of electric field.
For a conducting particle in a DC field, f_{CM} is a real quantity depending only on the electrical conductivities of the particle and the medium (see Eq. (1.17b)). For perfectly conducting particles in a liquid medium, namely in the limit:

$$\frac{\sigma_p}{\sigma_m} \to \infty, \qquad (2.13)$$

f_{CM} tends to 1 by Eq. (1.17b). Assuming that particles are subjected only to DEP and drag force and quickly reach a steady motion, the induced velocity field has the form of Eq. (1.19). For a spherical, perfect conductor particle of radius R_2 immersed in a liquid of dynamic viscosity η, by Eq. (1.20) the DEP mobility is:

$$\mu_{DEP} = \frac{\varepsilon_m R_2^2}{3\eta}.$$

Each type of chain is characterized by a well-defined DEP mobility μ_{DEP}^i, with *i*=1,2,3,4-particle chain. The total velocity field is:

$$\boldsymbol{u}_{tot}^i = \boldsymbol{v}_{DEP}^i + \boldsymbol{u}_m. \qquad (2.14)$$

For the DEP mobility, the following relation in the steady motion is valid:

$$\mu_{DEP}^{i} = \alpha_i \mu_{DEP}^{1}, \tag{2.15}$$

where α_i (with i = 2,3,4) are essentially geometrical factors ($\alpha_2 = 6.8, \alpha_3 = 13.8, \alpha_4 = 23$), also including the volume and shape enhancements of the effective dipole moment of the i-particles chain. The particles and the chains can be represented using their particle volume fraction φ^i and drift-diffusion current, defined as follows by generalizing Eq. (2.9):

$$\boldsymbol{J}^i = -D\nabla\varphi^i + \boldsymbol{u}_{tot}^{i}\,\varphi^i. \tag{2.16}$$

Reaction terms $Q_{(j)}^{(i)}$, depending on the nature of the reaction considered, can be introduced for the description of the particle stitching and chain formation. By labeling each particle or particle-chain species with P_i, the stitching reactions with the associated rates are the following form:

$$2P_1 \leftrightarrow P_2 \rightarrow Q_{(1)}^{(2)} = k_1[P_1]^2 - k_2[P_2], \tag{2.17a}$$
$$3P_1 \leftrightarrow P_3 \rightarrow Q_{(1)}^{(3)} = k_3[P_1]^2 - k_4[P_3], \tag{2.17b}$$
$$P_1 + P_2 \leftrightarrow P_3 \rightarrow Q_{(2)}^{(3)} = k_5[P_1][P_2] - k_6[P_3], \tag{2.17c}$$
$$4P_1 \leftrightarrow P_4 \rightarrow Q_{(1)}^{(4)} = k_7[P_1]^4 - k_8[P_4], \tag{2.17d}$$
$$2P_2 \leftrightarrow P_4 \rightarrow Q_{(2)}^{(4)} = k_9[P_2]^2 - k_{10}[P_4], \tag{2.17e}$$
$$P_1 + P_3 \leftrightarrow P_i \rightarrow Q_{(3)}^{(4)} = k_{11}[P_1][P_3] - k_{12}[P_4], \tag{2.17f}$$

where k_l $(l = 1, \dots, 12)$ are the reaction constants and $[P_i]$ are quantities proportional to the mass concentration. Providing $[P_i] \rightarrow \varphi^i$, all k_l are in unit of sec^{-1}. The set of equations governing the reaction-diffusion dynamics for φ^i is:

$$\frac{\partial}{\partial t}\varphi^1 + \nabla \cdot \boldsymbol{J}^1 = -2Q_{(1)}^{(2)} - 3Q_{(1)}^{(3)} - Q_{(2)}^{(3)} - 4Q_{(1)}^{(4)} - Q_{(3)}^{(4)}, \tag{2.18a}$$

$$\frac{\partial}{\partial t}\varphi^2 + \nabla \cdot \boldsymbol{J}^2 = Q_{(1)}^{(2)} - Q_{(2)}^{(3)} - 2Q_{(2)}^{(4)}, \tag{2.18b}$$

$$\frac{\partial}{\partial t}\varphi^3 + \nabla \cdot \boldsymbol{J}^3 = Q_{(1)}^{(3)} + Q_{(2)}^{(3)} - Q_{(3)}^{(4)}, \tag{2.18c}$$

$$\frac{\partial}{\partial t}\varphi^4 + \nabla \cdot \boldsymbol{J}^4 = Q_{(1)}^{(4)} + Q_{(2)}^{(4)} + Q_{(3)}^{(4)}. \tag{2.18d}$$

To consider larger chains, the corresponding equations must be added to the set of Eq. 2.18. Moreover, if μ_{DEP}^i and the stitching coefficients for larger chains depend weakly on the number of particles in the chain, a compact set with a reduced number of differential equations can be used [44].

The overall set of governing equation to numerically simulate particle-chain formation is composed of Eq. (2.18), Eq. (7), $\boldsymbol{E} = -\nabla V$ and the Navier-Stokes equation [16].

Many-particle corrections can be introduced, providing that:

$\varepsilon_1 \rightarrow \varepsilon(\varphi_{tot})$,

where $\varphi_{tot} = \sum_{i=1}^{4} \varphi^i$ is the total volume fraction. The dependence of ε on φ_{tot} is based on the EMA used for transport simulation in DEP.

Simulations on unstructured and perfectly conducting particles dispersed in a saline solution are carried out in Ref. [16]. The dielectric parameters used are:

$\varepsilon_m = 78\varepsilon_0$,

$\sigma_m = 6 \cdot 10^{-4}\mathrm{S/m}$.

For particles and chain: R=3.5 μm, $\varepsilon = \varepsilon_0$, $D_0 = 0.82\ 10^{-7}\ m^2/s$. The device geometry is the same as that previously considered in Fig. 2.1. In the initial configuration, all the four particles volume fraction φ^i are equal to zero and the reaction constants are set equal to: $k_1 = 2.1$, $k_2 = k_7 = 1.5$, $k_3 = k_8 = k_{10} = 1.5$, $k_4 = 1$, $k_5 = 3.1$, $k_6 = 1.8$, $k_9 = 2.0$, $k_{11} = 2.4$, $k_{12} = 1.3$.

k_l are free parameters to be adjusted in order to reproduce the real particle-particle interaction. The choice of this simulation represents only an example of study in order to emphasize some typical aspects of the dynamics. In this sense this method needs a parameter calibration study with the aid of a more accurate particle-like approach.

Figure 2.5 shows the evolution for some time steps. Four DEP mobilities are considered because there are four kinds of objects.

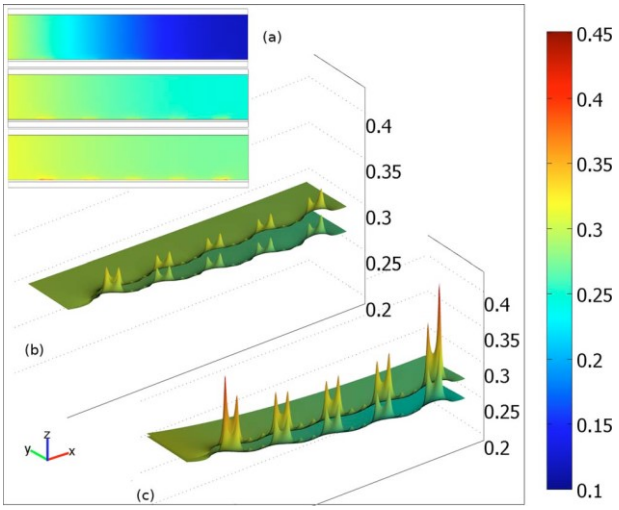

Fig. 2.5. Panel (a): snapshots taken at times 0.2, 0.6, and 1.0 s (from upper to lower) showing the time evolution of the total particle volume fraction φ_{tot} (see color bar on the right). Particles and fluid enter from the left boundary with a fluid speed of 0.5 $\mu m/sec$, where φ^1 is fixed to 0.3 and $\varphi^2 = \varphi^3 = \varphi^4 = 0$. In the other boundaries the condition $\varphi^i \cdot \boldsymbol{J}^i = 0$ is assigned. Electrodes (in number of ten) are separated from the fluid by a silicon layer 3 μm thick and they are taken at a voltage of 0 or + 2.5 V in an alternate sequence. Panel (b): three-dimensional plot where both the colored surfaces and the height (z-axis) represent φ_{tot} computed at times 0.6 and 1.0 s (from lower to upper) without particle stitching ($\varphi_{tot} = \varphi^1$). Panel (c): same as in panel (b) but with particle stitching included. (Figure taken from: O. E. Nicotra, A. La Magna, and S. Coffa, Appl. Phys. Lett. 95, 073702 (2009)).

The simulation time is reduced with respect to the one of the previous simulation where only spherical particles are considered. In fact, the DEP mobilities grow with increasing chain size and consequently a stronger DEP drift toward the electrodes is developed. This aspect can be seen in panels (b) and (c) of Fig. 2.5, where a calculation of φ_{tot} without chain formation ($k_l = 0$) is also displayed for comparison.

In Fig. 2.6, showing the particle-chain formation, φ^1 and φ^2 are reported, as well as in Fig. 2.7 for φ^3 and φ^4.

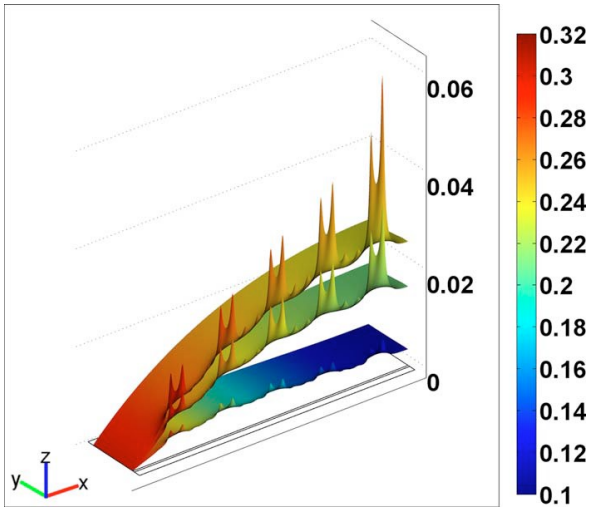

Fig. 2.6 Three-dimensional plot where the colored surfaces and the height (z-axis) represent respectively φ^1 and φ^2 taken at times 0.2, 0.5 and 1.0 s (from lower to upper). (Figure taken from: O. E. Nicotra, A. La Magna, and S. Coffa, Appl. Phys. Lett. 95, 073702 (2009)).

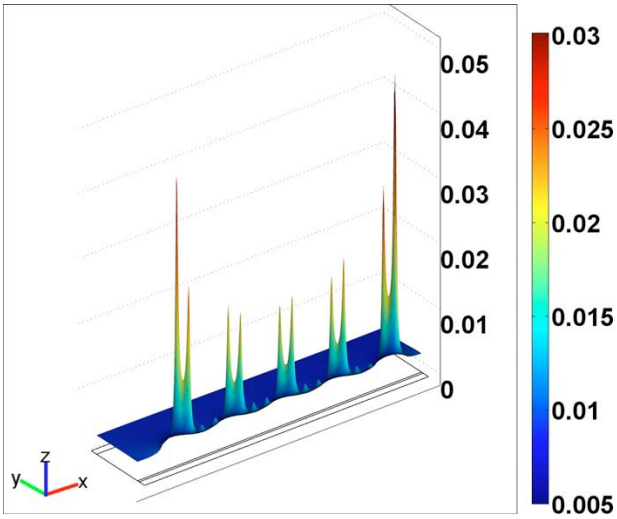

Fig. 2.7 Same as in Fig. 2.6 but for φ^3 and φ^4. Results shown refer only to time 1.0 s. (Figure taken from: O. E. Nicotra, A. La Magna, and S. Coffa, Appl. Phys. Lett. 95, 073702 (2009)).

In both Fig. 2.6 and Fig. 2.7, the volume fractions are represented by color field and height (z axis of the plot). Peaks are present in the colored surfaces at the edges of each electrode, where also the color field presents its maxima: this indicates that most part of the chain formation occurs in these regions. In fact, the rate terms in Eq. (2.17) are proportional to the volume fractions and particle stitching is more likely to occur in regions where particles accumulate. This mechanism, among others, is responsible for the slower kinetics of φ^3 and φ^4 with respect to φ^1 and φ^2.

The results of this simulation show the possibility of quantitatively describing particle-chain formation. This description is based on the extension of drift-diffusion dynamics with reaction terms properly included. The computation of the volume fractions φ^i allows to predict where and when particle chain formation occurs in a dielectrophoretic device.

Regarding the DEP mobility, in general EMA tends to reduce it. DEP mobility instead increases due to particle-chain formation. There is a competition between these two many-particle effects, but the present simulation shows that the latter is favored on the basis of the shortening of the evolution time. The particle stitching in DEP seems thus to completely dominate the entire transport dynamics. The two simulations show the importance of the many-particle corrections. The design of a dielectrophoretic device should not neglect such a phenomenon.

2.2 Analysis of stable configurations of e.mec. systems

A different approach from that set out in the previous sections requires the evaluation of the external electric field. Section 2.2.1 describes a simulation based on the calculation, by the electric field, of the electric potential energy and on the use of the MC technique, whereas Section 2.2.2 describes a simulation based on the use of MST.

2.2.1 Monte Carlo study of the static configurations

The method presented in Ref. [45], described below, allows the simulation of sufficiently large systems in terms of size and number of particles (i.e. within the experimental scopes).
$\langle \boldsymbol{F}^{STD} \rangle$ is a non-conservative force which can however be calculated as the negative gradient of the following effective average potential energy [46]:

$$\overline{U}_{eff}(\boldsymbol{r}) = -\frac{1}{2}\alpha_{eff} E^2_{RMS}(\boldsymbol{r}), \tag{2.19}$$

where α_{eff} is the average polarizability, which has the form:

$$\alpha_{eff} = 4\pi R^3 \mathrm{Re}\{\tilde{\varepsilon}_m\}\mathrm{Re}\{f_{CM}\}.$$

The DEP force is approximated as those generated by the total distorted electric field, which is equal to the sum of the external field and the contributions of the dipoles induced in all the particles [47]:

$$\mathbf{E}^{tot}(\boldsymbol{r}_i) \approx \mathbf{E}(\boldsymbol{r}_i) + \sum_j^{all\ the\ particles} \mathbf{E}_j(r_i). \quad (2.20)$$

By considering identical particles and neglecting multipole terms and mutual polarization, the effective potential energy can be derived from the expression that generalizes Eq. (2.19) for the case of particle-particle instantaneous interactions in the dipole approximation:

$$U_{ij} \approx -\frac{1}{2}\mathrm{Re}\{\mathbf{p}_i(\boldsymbol{r}_i)\cdot\mathbf{E}_j(\boldsymbol{r}_i)^*\} = -\frac{1}{2}\mathrm{Re}\{\mathbf{p}_j(\boldsymbol{r}_j)\cdot\mathbf{E}_i(\boldsymbol{r}_j)^*\}, \quad (2.21)$$

where $\mathbf{E}_j(\boldsymbol{r}_i)$ is the electrical field generated by the dipole in the particle *j* at the position $\boldsymbol{r}_i$, and $\mathbf{p}_i(\boldsymbol{r}_i)$ is the dipole moment induced on the *i*-th particle by the external field $\mathbf{E}(\boldsymbol{r}_i)$. Similar definitions apply to $\mathbf{E}_i(\boldsymbol{r}_j)$ and $\mathbf{p}_j(\boldsymbol{r}_j)$. The dipole electric fields in Eq. (2.21) are:

$$\mathbf{E}_j(\boldsymbol{r}_i) = \frac{1}{4\pi\mathrm{Re}\{\tilde{\varepsilon}_m\}}\frac{3\,\mathbf{n}\,(\mathbf{n}\cdot\mathbf{p}_j)-\mathbf{p}_j}{R_{ij}^3}, \quad (2.22)$$

$$\mathbf{E}_i(\boldsymbol{r}_j) = \frac{1}{4\pi\mathrm{Re}\{\tilde{\varepsilon}_m\}}\frac{3\,\mathbf{n}\,(\mathbf{n}\cdot\mathbf{p}_i)-\mathbf{p}_i}{R_{ij}^3}, \quad (2.23)$$

where $\mathbf{n} = \frac{\mathbf{R_{ij}}}{\mathrm{R_{ij}}}$.

Based on the above expressions, the average effective potential energy is:

$$\overline{U}_{i,j} \cong \frac{1}{4\pi\mathrm{Re}\{\tilde{\varepsilon}_m\}}|\alpha|^2\frac{1-3\cos\left(\theta_{i_j}^i\right)\cos\left(\theta_{i_j}^j\right)}{R_{ij}^3}\left[\boldsymbol{E}_{RMS}(\boldsymbol{r}_i)\cdot\boldsymbol{E}_{RMS}(\boldsymbol{r}_j)\right], \quad (2.24)$$

where $\theta_{i_j}^{i}$ and $\theta_{i_j}^{j}$ are the angles between the vectors $E(\boldsymbol{r}_i)$, $E(\boldsymbol{r}_j)$ and **n.**

The formalism presented above is useful to carry out, by the MC approach [48], simulations of the equilibration of a particle system suspended in a static liquid medium under the action of an oscillating non-uniform electric field. The particles are considered as hard spheres with radius r_i. The energy of the system is:

$$E(\{\mathbf{r}_1, \dots, \mathbf{r}_n\}) = \sum_i \overline{U}_{eff}(r_i) + \sum_{i,j} \overline{U}_{i,j}(r_i, r_j), \qquad (2.25)$$

where $\overline{U}_{eff}$ and $\overline{U}_{i,j}$ are calculated by Eq. (2.19) and (2.24).

In general, in the MC simulation, the external field is simulated by a numerical solver of the Poisson equation for different device structures. The numerical values of the vector electric field are interpolated in the grid of the MC simulation box. Periodic, reflecting, or mixed boundary conditions can be imposed depending on the problem under consideration.

The MC method is based on a stochastic sequence of single-particle displacement events. The application of an algorithm generates a new configuration by the old one. The Metropolis algorithm is used, which consists of the following steps:

- one particle i_s is randomly selected;
- the random displacement attempt is picked;

- the difference between the energies of the new and old configurations is calculated:

$$\Delta E = E\left(\{\boldsymbol{r}_i, \dots, \boldsymbol{r}_{i_s} + \Delta\boldsymbol{r}_{i_s}, \dots, \boldsymbol{r}_n\}\right) - E\left(\{\boldsymbol{r}_i, \dots, \boldsymbol{r}_{i_s}, \dots, \boldsymbol{r}_n\}\right)$$

- the proposed displacement is accepted, and the configuration is updated, if $\Delta E < 0$ or if $rand(0,1) \leq \exp(-\frac{\Delta E}{k_B T})$, where T is the system temperature.

Hard sphere behavior is reproduced considering $\Delta E \to \infty$ if the center-center distance between two particles is smaller than the sum of their radii.
The system considered in the simulation of Ref. [14] is a colloidal solution of Neurospora Crassa dispersed in a weakly conducting saline water solution. The effective complex dielectric constant can be approximated by the following expression (see Chapter 5 and Appendix C):

$$\tilde{\varepsilon}_{eff} = \tilde{\varepsilon}_{mem} \frac{\left(\frac{R}{R-d}\right)^3 + 2\frac{\tilde{\varepsilon}_{cyt} - \tilde{\varepsilon}_{mem}}{\tilde{\varepsilon}_{cyt} + 2\tilde{\varepsilon}_{mem}}}{\left(\frac{R}{R-d}\right)^3 - \frac{\tilde{\varepsilon}_{cyt} - \tilde{\varepsilon}_{mem}}{\tilde{\varepsilon}_{cyt} + 2\tilde{\varepsilon}_{mem}}}.$$

Figure 2.8 shows the real part of the Clausius-Mossotti factor of the Neurospora Crassa.

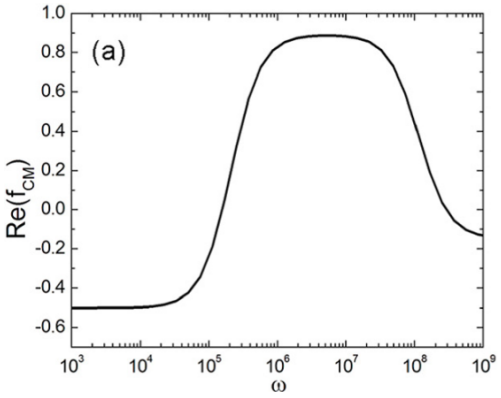

Fig. 2.8. Real part of the Clausius-Mosotti factor calculated with the dielectric model of the Neurospora Crassa cell. (Figure taken from: A. La Magna, M. Camarda, I. Deretzis, G. Fisicaro, and S. Coffa, Appl. Phys. Lett. 100, 134104 (2012)).

The cubic simulation box has dimensions $(1000 \cdot 1000 \cdot 1000)\mu m^3$. All the borders of the simulation box are grounded. The initial configuration consists in a random distribution of N=2000 cells (corresponding approximately to a 0.01 volume fraction) subjected to a uniform oscillating electric field ($E_{RMS} = 10^4 \frac{V}{cm}, \omega = 10^6\ Hz$). Figure 2.9 shows the results of a simulation after $2 \cdot 10^6$ MC iterations. In this case, the gradient of the electric field is null and the dielectrophoretic force is therefore absent. The behaviour of the system is due only to the particle-particle interactions. The system assumes an orderly configuration: the cell chains are aligned along the electric field direction.

In another type of simulation of the behaviour of N=2000 cells of Neurospora Crassa, one electrode (a single plate with width of $200\ \mu m$) is present at the center of the computational box. Figure 2.10(a) shows the spatial distribution of the electrical vector field and of the dielectrophoretic force field, as yellow and red arrows.

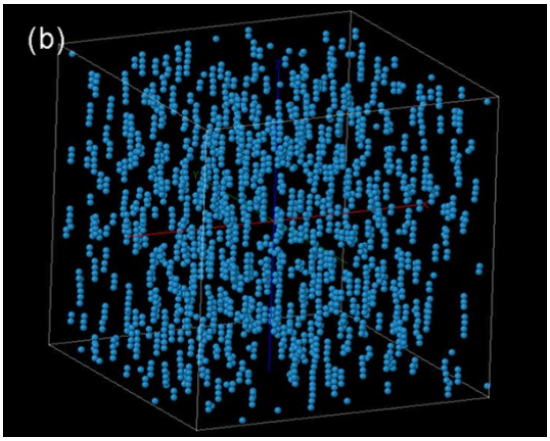

Fig. 2.9. Spatial distribution of N=2000 Neurospora Crassa cells suspended in a saline water solution subjected to a uniform oscillating electric field, obtained, starting from a random one, after $2 \cdot 10^6$ MC iterations. (Figure taken from: A. La Magna, M. Camarda, I. Deretzis, G. Fisicaro, and S. Coffa, Appl. Phys. Lett. 100, 134104 (2012)).

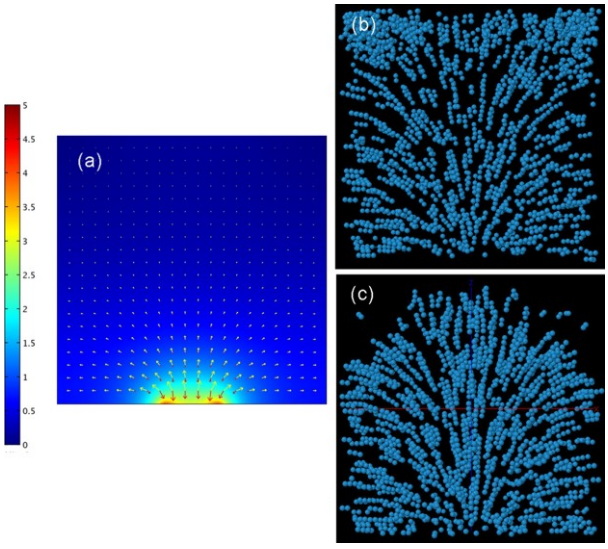

Fig. 2.10. (a): Spatial distribution of the electrical vector field and of the dielectrophoretic force field, as yellow and red arrows. (b): Spatial distribution of N=2000 Neurospora Crassa cells suspended in a saline water solution subjected to oscillating electric fields with angular frequency $\omega = 10^5\ Hz$ (n-DEP). (c): Spatial distribution with angular frequency $\omega = 10^6\ Hz$ (p-DEP). (Figure taken from: A. La Magna, M. Camarda, I. Deretzis, G. Fisicaro, and S. Coffa, Appl. Phys. Lett. 100, 134104 (2012)).

Figure 2.10(b) shows the system configuration obtained after $1 \cdot 10^7$ MC iterations in the case of an oscillating electric field with an angular frequency $\omega = 10^5\, Hz$ (n-DEP). Fig. 10(c) shows the case relative to $\omega = 10^6\, Hz$ (p-DEP). Both cases are characterized by the presence of particle chains that are displaced along the force lines of the electric field. The chains are larger in the regions of more intense field. The configurations obtained are rather stable. The device shows a moderate trapping efficiency in the case of p-DEP (Fig. 10(c)), while in the presence of n-DEP (Fig. 10(b)) cell densifications far away from the electrode occur. However, the equilibration mechanism seems massively ruled by the aligned chain formations.

The results clearly indicate that the particle-particle interactions compete with the DEP force field. Indeed, in pure p-DEP conditions, the particles would be massively trapped in the regions where the gradient of the electric field is higher. Therefore, the particle-particle interactions crucially affect the kinetic evolution of colloidal systems in DEP devices. The method presented by the authors strengthened the role of particle-particle interactions on the trapping capability of the device, on the arrangement of cells in ordered chains, and on the cell space distribution.

2.2.2 MST calculations of forces in few-particle systems

In Reference [49], an approximate theory of the DEP interaction in the proximity of a wall is derived for a dielectric sphere of radius R, to analyze the role of particle-wall interactions in the functioning of the

dielectrophoretic devices. Considering an infinite flat wall located at $z = 0$ of a Cartesian reference system, the result for the time averaged force on a particle in the presence of an electric field is:

$$\langle \mathbf{F}_{DEP}^{wall} \rangle = 2\pi\varepsilon_m R^3 \mathrm{Re}\left\{ f_{CM} \left(F_x E_{0_x} \hat{x} + F_y E_{0_y} \hat{y} + F_z E_{0_z} \hat{z} \right) \nabla \left(F_x^* E_{0_x}^* \hat{x} + F_y^* E_{0_y}^* \hat{y} + F_z^* E_{0_z}^* \hat{z} \right) \right\}, \quad (2.26)$$

where

$$F_x = F_y = \frac{1}{1 - f_{CM}\Delta},$$

$$F_z = \frac{1}{1 - 2f_{CM}\Delta},$$

with $\Delta = \left(\frac{R}{2z}\right)^3$.

Eq. (2.26) represents the extension of the standard DEP force for an isolated particle in an infinite medium given by Eq. (1.14).

In Ref. [17], in addition to $\langle \mathbf{F}_{DEP}^{wall} \rangle$, $\langle \boldsymbol{F}^{STD} \rangle$ and $\langle \boldsymbol{F}^{MST} \rangle$ are also calculated. For the calculation of $\langle \boldsymbol{F}^{MST} \rangle$, the commercial tool Comsol Multiphysics [50] is used. The studied system consists of a planar array of parallel electrodes. The electrodes have width $W_{el} = 50\,\mu m$ and are separated by a gap of $G_{el} = 50\,\mu m$. Voltage signals with opposing phase are applied to adjacent electrodes. The system is shown in Fig. 2.11.

$\langle \boldsymbol{F}^{MST} \rangle$, $\langle \boldsymbol{F}^{STD} \rangle$ and $\langle \mathbf{F}_{DEP}^{wall} \rangle$ as a function of the particle–wall distance along a vertical line located at the center of the electrode ($x = 75\,\mu m$) have been calculated. Fig. 2.12 shows the comparison between results of these different models.

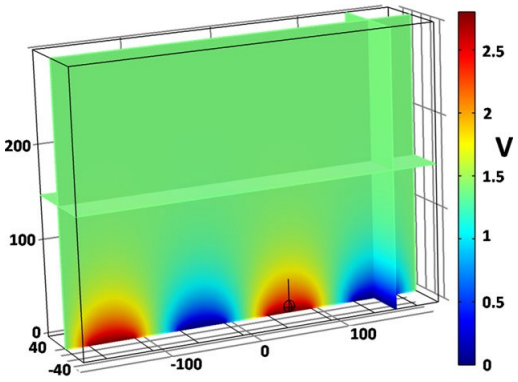

Fig. 2.11 Snapshot of the simulation box for the interdigitate electrodes system. The space dimensions are all in microns. The electric potential V is plotted as intensity map. A particle is located above the electrode centered in $x = 75\,\mu m$. Periodic boundary conditions are used on all side walls. The top and bottom boundaries are insulating, except above the electrodes. The black line indicates the plot region of Fig. 2.12. (Figure taken from: Camarda M, Scalese S, La Magna A, Electrophoresis, 36, (2015)).

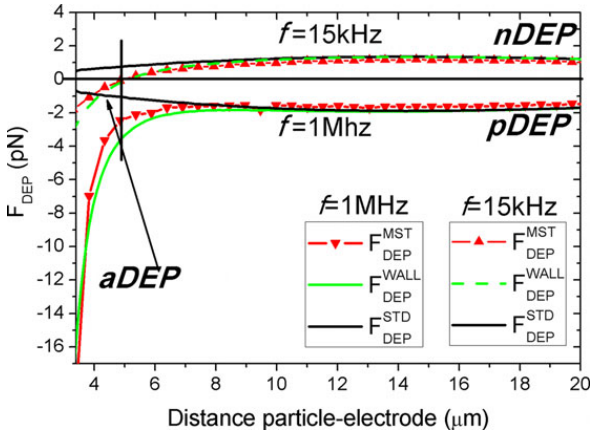

Fig. 2.12 Comparison between different model results for an interdigitate electrode system along a vertical line located over the center of the electrode (see Fig. 2.11). (Figure taken from: Camarda M, Scalese S, La Magna A, Electrophoresis, 36, (2015)).

The analysis of Fig. 2.12 shows that $\langle \mathbf{F}_{DEP}^{wall} \rangle$ correctly reproduced the force profile of the $\langle \boldsymbol{F}^{MST} \rangle$.

2.3 Conclusions

In this section we presented the state of the art (at the beginning of our Thesis work) of the theoretical/computational approaches for the study of many-particle effects in a system of EMPs. The method based on the MST of Section 2.2.2, implemented with a commercial tool for the case of a static fluid (Ref. [17]), is of particular importance for the objectives of this Thesis. In chapter 5, some results of Ref. [17] for a single EMP will indeed be used as validation data for our original simulation method based on a Coupled MD-FEM algorithm.

We wish to notice that the previous methods deal with some particular aspects of the complex behaviour of a system of interacting EMPs, whilst the kinetics of real systems is driven by many concurrent effects. In particular, mean field theories could in principle allow for fast solution considering the effects caused by the particle densification. Anyhow, since these theories are based on many undetermined parameters, the prediction which can be obtained with these methods is only qualitative: the parameter assessment needs more accurate particle-like approaches (like the one we will present in the next chapters) for the calibration in realistic conditions. It is probable that successful calibration can be obtained by fitting the results derived on fixed system geometry. Anyhow the calibration in principle can be also system dependent. As a consequence, the concurrent

use of mean field and accurate methods could be necessary for the general study of EMP systems.

Accurate derivation of the forces and the correspondent particle configurations can be obtained in the static limit. In this case the obvious limit is the missing kinetic solution; moreover, the many particle configurations have been studied neglecting the field modifications induced by the particle presence, whereas the correct force derivation using the MST based method is presented for the case of a single spherical particle. Apart from these considerations, as we will discuss in the following, the correct dynamics of the EMPs can be simulated only including other effective interactions in addition to the e.mec. ones due to the medium presence and the steric effect (i.e. the finite volume of the particles).

An important technical characteristic of this Thesis work is the application of an open source framework instead of a widely applied commercial package as COMSOL. This aspect has a double advantage: it permits the free distribution of the tool and it makes easier the integration with the MD method. In the next chapter we present the variational method, the FEM approximation and the open source platform for solving PDEs and data post-processing.

Chapter 3

The variational approach for the numerical solution of Partial Differential Equations

In the method we have developed to solve field mediated interactions, that will be described in Chapter 4, it is indispensable to solve numerically the field equations which are formulated in terms of partial differential equations (PDEs). In particular, as discussed at the end of Chapter 1, the Laplace problem must be resolved. For this purpose, the finite element method (FEM) represents a powerful approach and it is the one applied in our tool. There are commercial tools that solve PDEs through FEM; however, they are difficult to integrate in a more general code. In this Thesis, the open source software FEniCS was used, which allows for a more feasible integration and use of the PDEs solutions in a more general framework. We note that FEniCS requires the numerical implementation of the differential equations in the so-called *weak form* within the variational method.

This Chapter, after a brief reference to the basic concepts of the PDEs and problems with boundary values [51, 52], introduces the variational method for solving PDEs [53], the FEM [54, 55], the *FEniCS Project* software and other software useful for the meshing and results' analysis.

3.1 Partial Differential Equations

PDEs are differential equations containing derivatives of the unknown function u with respect to more than one variable. Consider a function:

$$F\colon \Omega \subset \mathbb{R}^N \to \mathbb{R},$$

with N a sufficiently large natural number. Whether the function explicitly depends on at least one of the partial order n derivatives of the function u, an equation of the type:

$$F\left(x_1, \dots, x_m, u, \frac{\partial u}{\partial x_1}, \dots, \frac{\partial u}{\partial x_m}, \dots, \frac{\partial^n u}{\partial x_1^n}, \dots, \frac{\partial^n u}{\partial x_m^n}\right) = 0 \qquad (3.1)$$

is called *partial differential equation* of order n. $x_1, \dots, x_m$ are the independent variables.

The objective of the solution of differential equations in a given domain is to determine the unknown function $u(x_1, \dots, x_m)$ that satisfies Eq. (3.1) within certain boundary conditions. This function is called *integral* or *solution* of the equation itself. The totality of the integrals constitutes the so-called *general integral* of the equation (excluding at most some of a particular character, called *singular*).

It is essential to highlight the differences between ordinary differential equations and partial differential equations. For an ordinary differential equation of order n, the set of its solutions (general integral) can be represented, unless possible singular integrals, by a function of the

independent variable, which depends on n integration constants $c_1, \dots, c_n$. Vice versa, for each family of functions with n parameters, an ordinary differential equation of order n exists and the function satisfies it.
For PDEs the situation is more complex: a general solution can be sought, but the arbitrary elements to be set in order to obtain a particular solution are no longer, in general, arbitrary constants, but are arbitrary functions.
The equation is said to be in *normal form* if it is resolved with respect to one of the derivatives of the maximum order with respect to a single independent variable, i.e. if it appears in the following form:

$$\frac{\partial^n u}{\partial x_1^n} = g\left(x_1, \dots, x_m, u, \frac{\partial u}{\partial x_1}, \dots, \frac{\partial u}{\partial x_m}, \dots, \frac{\partial^n u}{\partial x_1^{n-1}\partial x_2}, \dots, \frac{\partial^n u}{\partial x_m^n}\right).$$

3.2 Boundary value problems

An important problem class is formed by *boundary value problems*. In the case of equations of evolution (like the equation of heat or that of waves), they are also said "initial and boundary value problems", because in this case it is necessary to prescribe also the data to the initial time. In this type of problem, the domain on which the solution must be defined is assigned a priori. In boundary value problems, it is sufficient to prescribe only one boundary data. Three cases are distinguished:

- *Dirichlet problem*: the boundary data is prescribed as the value of the unknown function u;

- *Neumann problem*: the boundary data is prescribed as the value of the normal derivative of u at the Ω frontier;

- *Robin problem*: the boundary data is prescribed as the value of a linear combination of the the function and of its derivative, at the Ω frontier.

In any case, a second information on the solution is assigned, as a restriction on its definition domain. Finally, it is possible to prescribe the value of the unknown function on a part of the domain boundary and the value of its normal derivative on the remaining part: these cases are called *problems with mixed conditions*.

3.2.1 Boundary problem for the Poisson equation

Consider a three-dimensional spatial domain $\Omega \subset \mathbb{R}^3$, limited and connected with regular boundary $\partial\Omega$. The 3D Poisson's problem is:

$$\nabla^2 u(\boldsymbol{r}) = f(\boldsymbol{r}), \quad \boldsymbol{r} \in \Omega, \tag{3.2}$$

where $u(\boldsymbol{r})$ is the unknown function defined on Ω, ∇^2 is the Laplace operator, $f(\boldsymbol{r})$ is a prescribed function. This expression is the so-called *strong formulation* of the Poisson's problem. To have a single solution, appropriate boundary conditions should be added, as follows.
The Dirichlet problem for the Poisson's equation in an open limited $\Omega \subset \mathbb{R}^3$ with regular boundary is:

assigned the function $u_D: \partial\Omega \rightarrow \mathbb{R}$, to determine $u \in C^2$ such that:

$$\begin{cases} -\nabla^2 u(\boldsymbol{r}) = f(\boldsymbol{r}), & \boldsymbol{r} \in \Omega \\ u(\boldsymbol{r}) = u_D(\boldsymbol{r}), & \boldsymbol{r} \in \partial\Omega \end{cases} \tag{3.3}$$

If $u_D(\boldsymbol{r}) = 0$, the problem is said to be homogeneous.

The Neumann problem for the Poisson equation in an open limited $\Omega \subset \mathbb{R}^3$ with regular boundary is:
assigned the function $h(r): \partial\Omega \rightarrow \mathbb{R}$, to determine $u \in C^2$ such that:

$$\begin{cases} -\nabla^2 u(\boldsymbol{r}) = f(\boldsymbol{r}), & \boldsymbol{r} \in \Omega \\ \nabla u \cdot \mathbf{n} = \frac{\partial u}{\partial n} = h(\boldsymbol{r}), & \boldsymbol{r} \in \partial\Omega \end{cases} \tag{3.4}$$

where **n** is the external normal to Ω. If $h = 0$, the problem is said to be homogeneous.
It is evident that if u solves Neumann's problem, u + *constant* solves it as well. Therefore, there can be no uniqueness of solutions, at least in the full sense of the term.

It is useful to underline what is the modelling meaning of the boundary conditions. The conditions of the type of Dirichlet are of immediate interpretation, consequent from the meaning of the unknown u.

For example, in problems of heat diffusion, where u generally represents a temperature, the condition of Dirichlet is assigned when the domain border is maintained at a known temperature by contact with a thermostat. The conditions of the Neumann type can have the meaning of flow conditions: always in the case of the heat equation, it is known that the heat flow along x-axis in the body is (proportional to) $-ux$ (at least according to Fourier's law).

It is possible to define the mixed problem for the Poisson equation, in which different conditions are assigned to different portions of the boundary. Let be $\partial\Omega$ the boundary of the domain Ω, Γ_D the portion of Ω with Dirichlet boundary conditions and Γ_N the portion of Ω with Neumann boundary conditions. If $\partial\Omega = \Gamma_D \cup \Gamma_N$ with $\Gamma_D \cap \Gamma_N$ equal to empty set, the following conditions can be imposed:

$$\begin{cases} u = u_{\mathrm{D}}(\boldsymbol{r}) \,, \ \boldsymbol{r} \in \Gamma_D \\ \dfrac{\partial u}{\partial n} = h(\boldsymbol{r}) \,, \qquad \boldsymbol{r} \in \Gamma_N \end{cases} \tag{3.5}$$

In the case of problems posed for the evolution equations in a temporal range (0,T), the value of the solution and of their derivatives at final time T is obviously determined by the data at previous values of time, t < T. To prescribe data on the part of the domain boundary that lies on t = T therefore not needs, from the point of view of the modelling intuition (this intuitive consideration is in fact confirmed by the mathematical analysis of the problems in question).

3.3 Variational method

In order to expose the so-called *variational method* for the solution of a PDE, let's consider the specific case of the Poisson equation. Consider, as an example, a domain $\Omega \subset \mathbb{R}^3$ and the Dirichlet problem for the Poisson three-dimensional equation:

$$\begin{cases} -\nabla^2 u(\boldsymbol{r}) = f(\boldsymbol{r}), & \boldsymbol{r} \in \Omega \\ u(\boldsymbol{r}) = u_{\mathrm{D}}(\boldsymbol{r}), & \boldsymbol{r} \in \partial\Omega \end{cases} \tag{3.6}$$

The unknown function u to be approximated is referred to as a *trial function*. Within the variational method, a function v (called *test function*) is introduced. Suitable function spaces are defined for the test and trial functions, to specify their properties: the function space of trial function, indicated by F, is called *trial space*. The function space of test function, indicated by $\hat{F}$, is called *test space*.
In applying the method, first, the Poisson equation is multiplied by the test function v and integrated over Ω:

$$-\int_{\Omega} (\nabla^2 u)\, v \mathrm{d}x = \int_{\Omega} f\, v \mathrm{d}x. \tag{3.7}$$

dx denotes the differential element for integration over the domain Ω.

Eq. (3.7) contains a second-order spatial derivative of u, which can be transformed to a first-derivative of u and v by applying the technique of integration by parts.
The formula reads:

$$-\int_{\Omega}(\nabla^2 u)\, v \mathrm{d}x = \int_{\Omega} \nabla u \cdot \nabla v \,\mathrm{d}x - \int_{\partial\Omega} \frac{\partial u}{\partial n} v \,\mathrm{d}s\,, \qquad (3.8)$$

where $\frac{\partial u}{\partial n} = \nabla u \cdot \boldsymbol{n}$ is the derivative of u in the outward normal direction $\boldsymbol{n}$ on the boundary of Ω and ds denotes the differential element for integration over such a boundary.
An important feature of variational formulations is that the test function v must vanish on the parts of the boundary where the solution u is known. In the present case this means that $v = 0$ on the whole boundary $\partial\Omega$. It is thus required that the function is not too badly behaved so that the involved integrals do indeed exist. More specifically, both v and ∇v must be square integrable on Ω. The trial and test spaces F and $\hat{F}$ in the present problem are therefore defined as:

$$F = \{v \in H^1(\Omega) : v = u_{\mathrm{D}} \; on \; \partial\Omega\},$$

$$\hat{F} = \{v \in H^1(\Omega) : v = 0 \; on \; \partial\Omega\},$$

where $H^1(\Omega)$ is the Sobolev space containing functions v such that v^2 and $|\nabla v|^2$ have finite integrals over Ω (these conditions essentially mean that the

functions are continuous [51]). $\hat{F}$ contains infinitely many functions, and any of them can be used as test function v. $\hat{F}$ has thus infinite dimension.
The second term on the right-hand side of Eq. (3.8) therefore vanishes and it becomes:

$$-\int_{\Omega} (\nabla^2 u)\, v \mathrm{d}x) = \int_{\Omega} \nabla u \cdot \nabla v \, \mathrm{d}x. \tag{3.9}$$

From Eq. (3.7) and Eq. (3.9) it follows that:

$$\int_{\Omega} \nabla u \cdot \nabla v \, \mathrm{d}x = \int_{\Omega} f \, v \mathrm{d}x. \tag{3.10}$$

Eq. (3.10) represents the *weak form* or variational form of the original boundary-value problem of Eq. (3.6). The weak formulation allows thus to move from a differential problem of the second order to one of the first order. Eq. (3.10) must hold for all test functions in some test space and it is therefore possible to determine the solution u which lies in some (possibly different) trial space.
The statement of variational problem now becomes as follows:

find $u \in F$ such that:

$$\int_{\Omega} \nabla u \cdot \nabla v \, \mathrm{d}x = \int_{\Omega} f \, v \mathrm{d}x \quad \forall \, v \in \hat{F}. \tag{3.11}$$

In mathematics literature the following canonical notation for variational problems is introduced:

$$a(u,v) = \int_{\Omega} \nabla u \cdot \nabla v \, dx, \tag{3.12}$$

$$L(v) = \int_{\Omega} f \, v dx. \tag{3.13}$$

$a(u,v)$ is called bilinear form and $L(v)$ is called linear form. By introducing the linear and bilinear form in Eq. (3.11), the variational form is defined as it follows:

find $u \in F$ such that:

$$a(u,v) = L(v) \;\; \forall \, v \in \hat{F}. \tag{3.14}$$

To solve a linear problem, we have therefore to identify the terms which contain unknown u and collect them in $a(u,v)$, and similarly collect all terms with only known functions in $L(v)$. As a consequence, in terms of the computational approach, the variational methods consist in integral weighted averages of the starting equation which act on the weak form of the problem.

It is important to underline that the variational problem of Eq. (3.11) is a *continuous problem*.

3.3.1 Solution of Laplace's problem by the variational method

As mentioned at the end of Par. 1.4, since we deal with the MST evaluation of the e.mec. interactions, in the numerical tool at the basis of this Thesis it is necessary to solve the Laplace equation:

$$\nabla \cdot [\tilde{\varepsilon}\, \nabla\, \mathrm{V}(\mathbf{r})] = 0.$$

where V (the dependence on **r** is omitted for simplicity of notation) is the complex electrical potential:

$$\mathrm{V} = \mathrm{Re}\{\mathrm{V}\} + i\ \mathrm{Im}\{\mathrm{V}\} = \mathrm{V}_R + i\mathrm{V}_I \qquad (3.15)$$

and $\tilde{\varepsilon}$ is the general expression for the complex permittivity (see Par. 1.5).

$$\tilde{\varepsilon} = \mathrm{Re}\{\tilde{\varepsilon}\} + i\ \mathrm{Im}\{\tilde{\varepsilon}\} = \varepsilon_R + i\ \varepsilon_I. \qquad (3.16)$$

The subscripts R and I indicate clearly the real part and the imaginary part (thereafter, this notation will be adopted for all complex quantities).
As already seen, the complex permittivity has the following values inside the particles and in the medium:

$$\tilde{\varepsilon} \equiv \begin{cases} \tilde{\varepsilon}_p = \varepsilon_p - i\frac{\sigma_p}{\omega} \\ \tilde{\varepsilon}_m = \varepsilon_m - i\frac{\sigma_m}{\omega} \end{cases}$$

The linear and bilinear forms, Eqs (3.12) and (3.13), are complex themselves and can be written:

$$\tilde{a}(\tilde{u}, \tilde{v}) = \int_\Omega \tilde{\varepsilon}\, \nabla\tilde{u} \cdot \nabla\tilde{v}\, \mathrm{d}x = a_R + ia_I, \tag{3.17}$$

$$\tilde{L}(\tilde{v}) = \int_\Omega \tilde{f}\, \tilde{v}\mathrm{d}x = L_R + iL_I, \tag{3.18}$$

where

$$\tilde{v} = v_R + iv_I \tag{3.19}$$

is the complex test function and

$$\tilde{f} = f_R + if_I \tag{3.20}$$

is the complex prescribed function (which is null in the case of Laplace equation).

Consistently with the variational method, the solutions of the Laplace's problem for the real and imaginary part V_I and V_R of the electrical complex potential function V can be obtained and, starting from these, the real and

the imaginary part of the electric field can be calculated. The complex electric field is indeed:

$$\mathbf{E} = -\nabla \mathrm{V}, \tag{3.21}$$

and consequently:

$$\mathbf{E}_R + i\mathbf{E}_I = -\nabla \mathrm{V}_R - i\nabla \mathrm{V}_I. \tag{3.22}$$

By the previous expression:

$$\mathbf{E}_R = -\left(\hat{\imath}\frac{\partial \mathrm{V}_R}{\partial x} + \hat{\jmath}\frac{\partial \mathrm{V}_R}{\partial z} + \hat{k}\,\frac{\partial \mathrm{V}_R}{\partial z}\right) \equiv \left(E_{x,R}, E_{y,R}, E_{z,R}\right), \tag{3.23}$$

$$\mathbf{E}_I = -\left(\hat{\imath}\frac{\partial \mathrm{V}_I}{\partial x} + \hat{\jmath}\frac{\partial \mathrm{V}_I}{\partial z} + \hat{k}\,\frac{\partial \mathrm{V}_I}{\partial z}\right) \equiv \left(E_{x,I}, E_{y,I}, E_{z,I}\right), \tag{3.24}$$

and finally:

$$E_x = E_{x,R} + iE_{x,I}, \tag{3.24}$$

$$E_y = E_{y,R} + iE_{y,I}, \tag{3.25}$$

$$E_z = E_{z,R} + iE_{z,I}. \tag{3.26}$$

These values of the electric field components and their conjugate complex will be inserted into Eq. (1.29) to numerically calculate the force $\langle \boldsymbol{F}^{MST} \rangle$ and in Eq. (1.30) to evaluate the torque $\langle \boldsymbol{T}^{MST} \rangle$.

3.4 FEM approximation

It may be difficult or even impossible to solve analytically a PDE. The FEM is a general and efficient method for the numerical solution of PDEs. FEM involves the discretization of a large domain into small parts of coded form, called *finite elements* (typically triangles and quadrilaterals for 2D domains, tetrahedrons and hexahedrons for 3D domains), that are defined by points called *nodes*. The grid thus formed is called *mesh*. A field quantity is approximated using polynomial interpolation over each of the elements and, by this formulation, a set of simultaneous algebraic equation results: the equations concerning the finite elements form in fact a large system of equations that models the total problem. In order to solve this system and approximate the solution, FEM use then variational methods. The important points are: what kind of elements should be used, how many elements are needed, where the mesh can be coarse and where must be fine, the eventual assumptions and the choice of a suitable software.
Summarizing, the use of FEM follows usually these steps:

- node and element generation: subdivide the domain into small finite elements, each of which is defined by a finite number of node points;

- application of boundary conditions;

- within each element, a solution to governing equations is formulated and solved;

- general solution for all elements results in algebraic set of simultaneous equations.

3.4.1 Galerkin Method of FEM approximation

The solution of the PDEs must belong to a functional space where the derivatives are continuous, neverthless the Sobolev space H^1 allows functions with discontinuous derivatives. This weaker continuity requirement of u in the variational form of Eq. (11) has practical consequences in the construction of the functional finite element spaces: among them, the most important is that the use of piecewise polynomial function spaces is permitted, i.e. function spaces built by combining polynomial functions on simple domains such as intervals, triangles or tetrahedrons.

Application of FEM starts by rewriting the PDE as a variational equation. It has been seen that the variational problem (Eq. (3.11)) is a continuous problem: it identifies the solution u in the infinite-dimensional function space V. Thanks to the FEM, it is possible to approximate u by a continuous piecewise linear function u_h. For this purpose, it needs to suitably define the *discrete* (finite-dimensional) trial and test spaces $F_h \subset F$

and $\hat{F}_h \subset \hat{F}$ and replace the infinite-dimensional function trial space F and function test spaces $\hat{F}$ by them. The boundary conditions are encoded as part of the trial and test spaces.
The discrete variational problem consequently is:

find $u_h \in F_h \subset F$ such that

$$\int_\Omega \nabla u_h \cdot \nabla v \, \mathrm{d}x = \int_\Omega f v \, \mathrm{d}x \quad \forall \, v \in \hat{F}_h \subset \hat{F}. \tag{3.27}$$

The variational problem of the previous expression uniquely defines the approximate numerical solution of Poisson's problem. This type of FEM, based on similar trial and test spaces, is called Galerkin Method, in honour of the Russian physicist and mathematician who conceived it.

3. 5 FEniCS Project, Gmsh, Salome

Here we outline the characteristics of the open source tool we have applied to implement our code.

3.5.1 FEniCS Project

FEniCS Project [56] is an open source software package that implements a finite element method to solve partial differential equations of importance in engineering and Physics. The programming language used in

the works present in this Thesis for the code implementations by FEniCS is *Python*.

Let us consider the discrete variational problem of Eq. (3.27). The PDE can be solved with the FEniCS code thanks to its abstractions relative to the linear and bilinear form. In fact, the formulas for a (Eq. (3.12)) and L (Eq. (3.13)) can be expressed directly in a FEniCS program. Moreover, the terms trial and test functions, used in mathematics, are also used in FEniCS.

It should be noted that the finite element variational problem of Eq. (3.27) looks in FEniCS the same as the continuous variational problem of Eq. (3.11): in fact, while in the mathematics literature on variational problems u_h indicates the solution of the discrete problem and u indicates the solution of the continuous problem, in the corresponding FEniCS program u indicates the solution of the discrete problem. Similarly, in the mathematics literature V_h indicates the discrete finite element function space, while in the FEniCS programs it is denoted by F. There consequently is a one-to-one relationship between the mathematical formulation of a continuous problem and the corresponding FEniCS program.

To solve a boundary-value problem by FEniCS, it needs to follow these steps:

- identify the PDE, its computational domain Ω and its boundary conditions;

- redefine the PDE as a finite element variational problem;

- define the finite element spaces F and $\hat{F}$ by specifying the domain, the mesh, the type and degree of function space;

- write a Python code which includes the quantities of the first points by using the corresponding FEniCS abstractions;

- use the appropriate FEniCS command to solve the boundary-value problem.

For the details see the associated web page: https://fenicsproject.org/.

3.5.2 Gmsh

FEniCS offers the possibility of generating spatial sampling to obtain the calculation grid (mesh). In 3D this potentiality is limited. In the works presented in this Thesis, Gmsh is consequently used. Gmsh [57] is an open-source computer-aided engineering platform which operates on the basis of parametric inputs. It offers, among others, solutions for meshing and provides a number of mechanisms to control the accuracy of elements in mesh generation. The Gmsh software libraries can be used alone or together with external applications. An important point is that it interacts with external solvers, including FEniCS.

As an example of application, several images created by Gmsh are reported in Fig. 3.1: panel (a) shows the edges of a box of dimensions $(100 \cdot 50 \cdot 50)\ \mu m^3$, panel (b) the surface mesh (namely relative to the

faces of the parallelepiped), panel (c) the volumetric mesh, panel (d) a sphere with a surface mesh.

3.5.3 Salome

Salome is a free software which consists of a generic platform for pre- and post-processing of numerical simulations, meshing, visualization and analysis of FEM results. It is released under the GNU Lesser General Public License and may be downloaded from its official website [58]. It is based on an open architecture made of several components. Its software libraries can be used alone or in combination with other software applications for the study of a CAD model.

Salome was used to visualise the output files of the solution of the Laplace problem created by FEniCS. The files show the electrical potential or electric field, displayed according to a colour scale. The default setting allows to display the values of the external part of the box, with or without the presence of the surface mesh. In order to show the solution in spatial regions of interest inside the box, the “slice” function was used, which allows to display a section of a three-dimensional object. As an example, Fig. 3.2 shows the solution of the Laplace problem in the box of Fig. 3.1 when an electric potential V=0 is applied to the top and V=5 Volt is applied to the bottom: panel (a) shows the surface mesh drawn with a colour scale relative to the values of the solution, panel (b) shows the slice passing through the centre of the box and parallel to the front face.

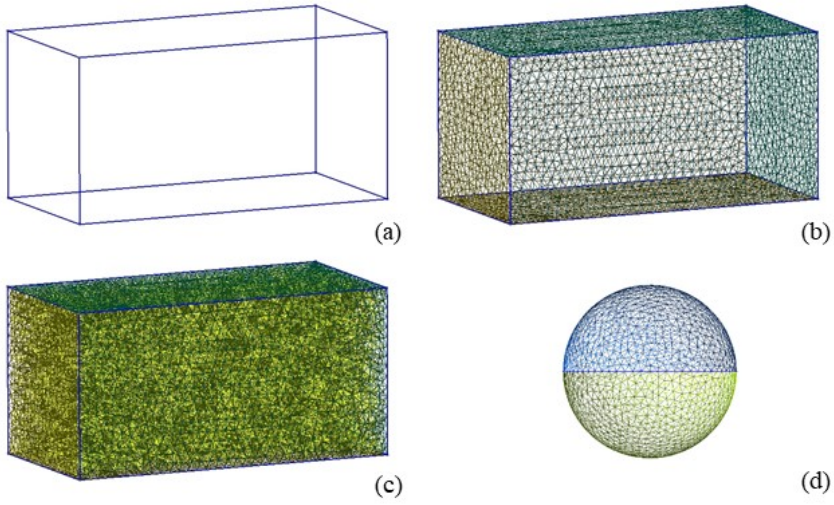

Fig. 3.1 Images created by Gmsh. (a): edges of a box of dimensions $(100 \cdot 50 \cdot 50)\ \mu m^3$. (b): surface mesh. (c): volumetric mesh. (d): sphere with a surface mesh.

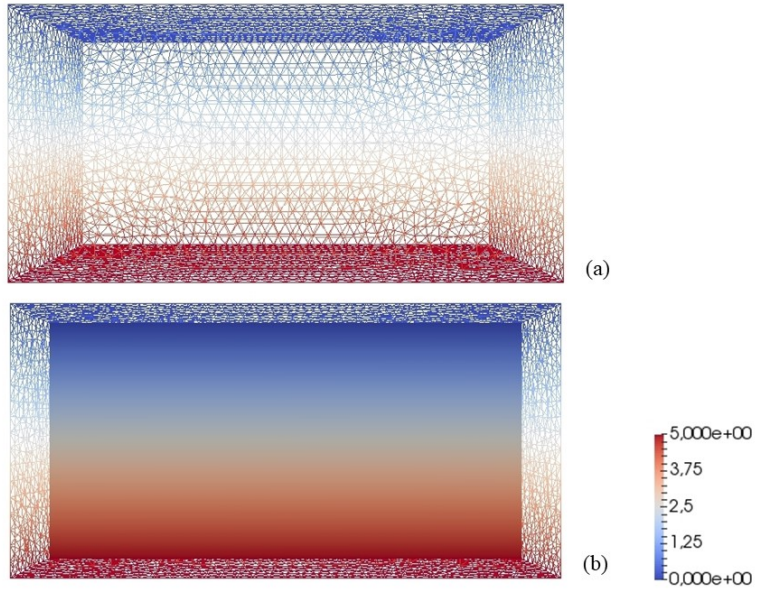

Fig. 3.2 Images created by Salome. (a): surface mesh in color scale related to the solution. (b): slice passing through the centre of the box and parallel to the front face.

3.6 Remarks

In this section we presented a short reference to the basic concepts of the PDEs, to the variational method for solving them, to the FEM and the usefulness of *FEniCS Project* to apply this method for a generic solution of PDEs in the weak form. In the next chapter we will deal with the second aspect of our coupled method: we will report a brief presentation of the Molecular Dynamics and relative integration method (Verlet Integration) and present the formalization of the MD-FEM code used for the simulations.

Chapter 4

Coupled Molecular Dynamics-Finite Element Method algorithm

The general objective of this Thesis work is the extension of the so-called “simulation” approach and related techniques in different application fields. In theoretical Physics, a model of a system is considered, generally subjected to approximations and based on equations to be solved analytically or numerically. Numerical simulations, based on the models of physical systems, can play an important role in the theoretical study of the evolution of a system because it is possible to increase the level of complexity of the description with respect to the analytical models. They provide very accurate results (depending on the level of precision in the modelling of the fundamental interaction ruling the system’s behaviour) for problems that cannot be solved analytically. In this regard, computer simulation can be considered both as a test of theories and as verification and analysis of experimental information. Numerical simulations allow also performing ideal experiments (*gedanken* experiments) under extreme conditions (i.e. of temperature and pressure, of purity of materials rarely achievable in a real experiment etc.). Simulations can both provide microscopic details of a system and describe macroscopic properties of experimental interest (state equations, transport coefficients, structural parameters, etc.). Numerical results are finally analyzed and interpreted, with techniques similar to those used to characterize experimental data.

Compared to experimental methods, simulations are usually costless and less time consuming.

Molecular Dynamics (MD) is a widely used simulation technique for the computational study of the movement of atoms and molecules, but our aim is to extend its applicability to EMPs. This Chapter provides a description of the MD technique [59, 60, 61] and the algorithm for coupling the MD with the FEM method for the simulation of EMP systems. The formalism here described has been originally implemented using the *Python API* in our open source tool. For the MD part we will use the Verlet integration technique [62, 63, 64], an algorithm diffusely used in the MD context.

4.1 Molecular Dynamics

MD is a set of computational techniques of simulation that in general allows to study the evolution of physical and chemical systems (i.e. sets of N interacting particles) at atomic and molecular level. MD is based on the step-by-step integration of the classical equations of particle motion, which are described as interacting point masses.

The MD method was introduced by Alder and Wainwright [65] in the 1950s for the study of systems composed of rigid spheres. It offered excellent results in the study of simple liquids. The first MD simulation of a realistic system (water in the liquid phase) dates back to 1971 (Rahman and Stillinger [66]). In the following years, rigid molecules (Barojas, Levesque and Quentrec, 1973 [67]) and flexible hydrocarbons (Ryckaert and

Bellemans, 1975 [68]) were studied. Computer MD simulations were also performed on phase transitions and interface behaviour of different materials (1974-1980). An advancement of simulation techniques occurred with the development of "dynamic stochastic" methods (Friedman, 1977 [69]) and with the introduction of methods for measuring transport coefficients (McDonald, 1979 [70]). Recently, developments have turned to the search for metastable states and multiscale problems [71, 72], in which MD is integrated with other calculation techniques, in particular the Monte Carlo method [73], allowing to overcome the main limit of MD that consists in the short duration of the simulations (a few ns) and in the small size of the studied systems (fractions of μm3). In general, the fields of applications of MD are liquids, defects in solids, surfaces and interfaces of solids, fractures, molecular clusters, biomolecules (e.g. DNA), diffusion through membranes (e.g. H2O through graphene), heat transport [74, 75], complex dynamic processes that take place in solid state physics, materials science, biological systems, chemistry [76].

4.1.1 MD implementation

MD is a deterministic technique: given an initial state of positions and velocities, the time evolution of the system is completely determined (unlike e.g. Monte Carlo methods). Deviation of this principle is mainly due to numerical errors and physical conservation rules are commonly used to control the integration accuracy. Particles in general interact through a potential which can be a semi-empirical (classical) potential or can be

derived by a quantum mechanical approach, whilst the particle kinetics is essentially classic (i.e. quantum theory is applied within the Born-Oppenheimer B.O. approximation [77]).

Consider a system composed of N massive points, described by the set of canonical coordinates $\{\boldsymbol{r}_i, \boldsymbol{p}_i\}$ and initialized with initial positions $\boldsymbol{r}_i(t_0)$ and initial velocities $\boldsymbol{v}_i(t_0)$. Initial mass positions generally are "randomly" displaced (depending on the system under consideration, they are displaced from the ideal equilibrium positions). In general, the initial positions can be obtained starting from experimental structures solved with the X-ray diffraction methods on mono-crystals, by nuclear magnetic resonance imaging (NMR) or from configurations derived from crystallography.

The distributions of initial velocities are generally referred to a Maxwell's random distribution corresponding to a specific temperature, if the system is considered as a canonical ensemble:

$$p(\boldsymbol{v}_i) = \sqrt{\frac{m_i}{2\pi k_B T}}\ exp\frac{m_i v_i^2}{2k_B T},$$

where $p(\boldsymbol{v}_i)$ is the probability that an atom has velocity $\boldsymbol{v}_i$ at temperature T. The initial random distribution of the speeds is chosen in such a way that the total momentum is zero, that is:

$$\mathbf{P}(\boldsymbol{v}_i) = \sum_{i=0}^{N} m_i\, \boldsymbol{v}_i = 0.$$

The MD method is based on the iterative application of Newton's second law. The knowledge of the resulting force on each particle of the system allows determining its respective accelerations. For a system of N atoms, the motion of each atom in the system is therefore determined by the equation:

$$\boldsymbol{F}_i = m_i\, \boldsymbol{a}_i = m_i\, \frac{d^2}{dt^2}\boldsymbol{r}_i \qquad i = 1,\ldots, \mathrm{N}, \qquad (4.1)$$

where $\boldsymbol{F}_i$ is the resultant of the force acting on the particle of mass m_i and $\boldsymbol{a}_i$ is its acceleration. The fundamental assumption in classical dynamics, in which the forces are of empiric nature, is that they can be expressed as the gradient of a potential energy function $V(\boldsymbol{r}_1, \ldots \boldsymbol{r}_N)$ independent of time:

$$\boldsymbol{F}_i = -\nabla_i V(\boldsymbol{r}_1, \ldots \boldsymbol{r}_N). \qquad (4.2)$$

From Eq. (4.1) and (4.2):

$$-\nabla_i V(\boldsymbol{r}_1, \ldots \boldsymbol{r}_N) = m_i\, \boldsymbol{a}_i = m_i\, \frac{d^2}{dt^2}\boldsymbol{r}_i. \qquad (4.3)$$

The trajectories of the massive points are derived by integrating the Newtonian equations of motion.

It should be noted that the integration of equations of motion is in general a complex procedure because the displacement of the particles modifies the values of the potential energy of interaction and therefore of the forces acting on them.

By using the MD techniques, problems related to calculation times and computational resources are encountered, as it is necessary to be able to follow, at every step in time, all the degrees of freedom of the particles in the system. However, the increased performance of computers and the refinement of methods and algorithms have made possible calculations that were prohibitive until recently. Nevertheless, MD presents in general some limitations: it is suitable for classical and not fully quantum evolving particles (i.e. when B.O. is not appropriate as for lightweight systems like H, He, Ne, or low temperatures), time limitations (from pico to nanoseconds), size limitations (from thousands to few millions of atoms).

There are several ways to solve the Eq. (4.3) in MD contexts. One of the algorithms used in MD for constant energy simulations is the Verlet method, which will be described below.

4.2 Verlet Integration

In MD, methods to calculate trajectories of particles integrating Newton's equations of motion are required. The task is to construct a sequence of points that closely follow the masses on the trajectory of the exact solution. Verlet integration is a numerical method frequently applicated in MD. It was used by Carl Størmer to compute the trajectories of particles moving in a magnetic field and was popularized in MD by the physicist Loup Verlet in 1967. The Verlet integration offers greater stability than the much simpler Euler method [78] and other properties that are important in physical systems, such as time-reversibility.

4.2.1 Basic Verlet Integration

Let us consider conservative physical systems. Newton's equation of motion is:

$$\mathbf{M}\ddot{\boldsymbol{r}}(\mathrm{t}) = \mathbf{F}\big(\boldsymbol{r}(t)\big) = -\nabla V\big(\boldsymbol{r}(t)\big), \tag{4.4}$$

where t is the time, $\boldsymbol{r}(t) = \big(\boldsymbol{r_1}(t), \dots, \boldsymbol{r}_N(t)\big)$ is the ensemble of the position vector of N objects, V is the scalar potential function, $\mathbf{F}$ is the ensemble of forces on the particles, $\mathbf{M}$ is the diagonal block matrix with mass for every particle.

The initial positions $\boldsymbol{r}(0) = \boldsymbol{r_0}$ and initial velocities $\boldsymbol{v}(0) = \dot{\boldsymbol{r}}(0) = \boldsymbol{v_0}$ of the particles are typically given. In order to discretize and numerically solve this initial value problem, a suitable time step $\Delta t > 0$ is chosen and the sampling point sequence $t_n = n\Delta t$ is considered.

Verlet Integration is based on the central difference approximation to the second derivative:

$$\frac{\Delta^2 \boldsymbol{r}(t)}{\Delta t^2} = \frac{\frac{\boldsymbol{r}(t+\Delta t)-\boldsymbol{r}(t)}{\Delta t} - \frac{\boldsymbol{r}(t)-\boldsymbol{r}(t-\Delta t)}{\Delta t}}{\Delta t} = \frac{\boldsymbol{r}(t+\Delta t)-2\boldsymbol{r}(t)+\boldsymbol{r}(t-\Delta t)}{\Delta t^2} = \boldsymbol{a}(t). \tag{4.5}$$

The Verlet algorithm uses the following equation (deriving from the third and fourth members of the previous expression):

$$\boldsymbol{r}(t+\Delta t) = 2\boldsymbol{r}(t) - \boldsymbol{r}(t-\Delta t) + \boldsymbol{a}(t)\Delta t^2. \tag{4.6}$$

The next position vector (with respect to the time t) is thus obtained from the previous two. It is important to note that the velocity is not used. An important characteristic is about the order of accuracy of the errors. The time symmetry of this method reduces the level of errors introduced into the integration by calculating the position at the next time step. The Taylor expansions at time $t = t_n$ of the position vector in different time directions are:

$$\boldsymbol{r}(t + \Delta t) = \boldsymbol{r}(t) + \boldsymbol{v}(t)\Delta t + \frac{1}{2}\boldsymbol{a}(t)\Delta t^2 + \frac{1}{6}\boldsymbol{b}(t)\Delta t^3 + O(\Delta t^4). \quad (4.7)$$

$$\boldsymbol{r}(t - \Delta t) = \boldsymbol{r}(t) - \boldsymbol{v}(t)\Delta t + \frac{1}{2}\boldsymbol{a}(t)\Delta t^2 - \frac{1}{6}\boldsymbol{b}(t)\Delta t^3 + O(\Delta t^4). \quad (4.8)$$

where and $\boldsymbol{b}$ is the jerk (third derivative of the position with respect to the time). Adding these two expansions gives:

$$\boldsymbol{r}(t + \Delta t) = 2\boldsymbol{r}(t) - \boldsymbol{r}(t - \Delta t) + \boldsymbol{a}(t)\Delta t^2 + O(\Delta t^4). \quad (4.9)$$

The first and third-order terms from the Taylor expansion cancel out and the Verlet integrator is therefore an order more accurate than integration by simple Taylor expansion alone.

In the Basic Verlet equation, as seen above, only the positions are explicitly given, but not the velocities. However, velocities are often necessary, e.g. for the calculation of certain physical quantities like the kinetic energy. The velocity can be estimated using the position terms and the mean value theorem, as follows:

$$\boldsymbol{v}(t) = \frac{\boldsymbol{r}(t+\Delta t)-\boldsymbol{r}(t-\Delta t)}{2\Delta t} + O(\Delta t^2). \quad (4.10)$$

The calculation of velocities at time t can create technical problems in MD simulations, because they cannot be calculated until the positions are known at time $t + \Delta t$. The velocity term calculated in this way is a step behind the position term, since this is at time t and not $t + \Delta t$. Anyhow, the velocity is not used to update the position. Another way to remedy this deficiency is to use the Velocity Verlet algorithm, which is presented below.

4.2.2 Velocity Verlet algorithm

A commonly used algorithm is the Velocity Verlet, which is obtained from the original Verlet algorithm. This method explicitly incorporates velocity. First of all, it is useful to derive the following expression by Eq. (4.10):

$$\boldsymbol{r}(t + \Delta t) - \boldsymbol{r}(t - \Delta t) = 2\boldsymbol{v}(t)\Delta t. \quad (4.11)$$

In order to obtain an equation for the position, the term $\boldsymbol{r}(t + \Delta t)$ is added to both members of the Eq. (4.6), obtaining:

$$2\boldsymbol{r}(t + \Delta t) = \boldsymbol{r}(t + \Delta t) - \boldsymbol{r}(t - \Delta t) + 2\boldsymbol{r}(t) + \boldsymbol{a}(t)\Delta t^2. \quad (4.12)$$

By Eq. (4.11) and Eq. (4.12), the following expression for the position is obtained:

$$\boldsymbol{r}(t+\Delta t) = \boldsymbol{r}(t) + \boldsymbol{v}(t)\Delta t + \frac{1}{2}\boldsymbol{a}(t)\Delta t^2. \quad (4.13)$$

In order to obtain an equation for the velocity, we consider the original Verlet (Eq. (4.6)) for $\boldsymbol{r}(t)$ instead of $\boldsymbol{r}(t+\Delta t)$:

$$\boldsymbol{r}(t) = 2\boldsymbol{r}(t-\Delta t) - \boldsymbol{r}(t-2\Delta t) + \boldsymbol{a}(t-\Delta t)\Delta t^2. \quad (4.14)$$

By adding this last equation to Eq. (4.6):

$$\boldsymbol{r}(t+\Delta t) - \boldsymbol{r}(t-\Delta t) =$$
$$= \boldsymbol{r}(t) - \boldsymbol{r}(t-2\Delta t) + [\boldsymbol{a}(t-\Delta t) + \boldsymbol{a}(t)]\Delta t^2. \quad (4.15)$$

From Eq. (4.1) and Eq. (4.15):

$$\boldsymbol{2v}(t)\Delta t = \boldsymbol{r}(t) - \boldsymbol{r}(t-2\Delta t) + [\boldsymbol{a}(t-\Delta t) + \boldsymbol{a}(t)]\Delta t^2. \quad (4.16)$$

The Eq. (4.11) at the time $t-\Delta t$ is:

$$\boldsymbol{r}(t) - \boldsymbol{r}(t-2\Delta t) = 2\boldsymbol{v}(t-\Delta t)\Delta t. \quad (4.17)$$

From Eq. (4.16) and Eq. (4.17):

$$\boldsymbol{v}(t) = \boldsymbol{v}(t-\Delta t) + \frac{\boldsymbol{a}(t-\Delta t)+\boldsymbol{a}(t)}{2}\Delta t, \quad (4.18)$$

and, shifting the time step by one:

$$\boldsymbol{v}(t+\Delta t) = \boldsymbol{v}(t) + \frac{\boldsymbol{a}(t)+\boldsymbol{a}(t+\Delta t)}{2}\Delta t. \qquad (4.19)$$

In the end, the standard implementation scheme of the Velocity Verlet algorithm consists in the following steps:

- calculate $\boldsymbol{r}(t+\Delta t) = \boldsymbol{r}(t) + \boldsymbol{v}(t)\Delta t + \frac{1}{2}\boldsymbol{a}(t)\Delta t^2$; (4.20)
- derive $\boldsymbol{a}(t+\Delta t)$ using $\boldsymbol{r}(t+\Delta t)$;
- calculate $\boldsymbol{v}(t+\Delta t) = \boldsymbol{v}(t) + \frac{\boldsymbol{a}(t)+\boldsymbol{a}(t+\Delta t)}{2}\Delta t.$ (4.21)

One peculiarity of this method must be noted: the values $\boldsymbol{r}(t+\Delta t)$ is calculated as a function of $\boldsymbol{r}(t)$, $\boldsymbol{v}(t)$ and $\boldsymbol{a}(t)$ (quantities relative the previous time step), while $\boldsymbol{v}(t+\Delta t)$ is calculated as a function of $\boldsymbol{v}(t)$, $\boldsymbol{a}(t)$ and $\boldsymbol{a}(t+\Delta t)$. The velocity at the time $t+\Delta t$ thus depends also on the acceleration value calculated at the same time step and not only at the previous.

This formulation of the Verlet algorithm is completely equivalent to that of Eq. (4.3) as far as the propagation of the position is concerned. It should be noted, however, that this algorithm assumes that acceleration only depends on position and does not depend on velocity. In the case of analytic formulations of the dependence of $\boldsymbol{a}(t+\Delta t)$ on the velocity, we can consider Eq. (4.21) an implicit equation for the evaluation of $\boldsymbol{v}(t+\Delta t)$

provided that a single value solution can be found. This is the case of the drag forces we introduce in Chap. 5 to simulate correctly the EMPs kinetics in a fluid medium.
It can be shown that the error on the Velocity Verlet is of the same order as the Basic Verlet [62]. Stability of the technique depends heavily upon a uniform update rate and the ability to accurately identify positions at a small time Δt into the past.

4.3 MD-FEM algorithm

Our code aims at evaluating the evolution of a system of e.mec. particles by using MD techniques for the integration of the equations of motion. In this section we outline the implemented algorithm while some details and some extracts of the code are reported in the Appendix E. In the formulation here presented, the rotation of particles is neglected; this is a reliable approximation for the majority of real EMP systems. A generalization of the method which considers rotation is presented in Chap. 6. The simulation of particles' kinetics then consists of a sequence of loops with the following steps: system configuration preparation from the known positions and velocities of the particles; calculation of forces acting on the particles and then of the corresponding accelerations; integration of the equations of motion for a suitable time increment; new configuration setting. The calculation of the e.mec. force acting on the particles needs the solution of the Laplace's problem (see Sec. 1.4) with a complex potential variable in a 3D geometry, i.e. the corresponding PDE needs to be solved in

a numerical domain reproducing the system configuration (sources, medium and particles). Other eventual single particle forces are instead calculated by means of analytic expression (see Chap. 5).

The complex Laplace equation is solved using a Finite Element Method. In particular, in the code the corresponding *Python* methods, implementing calls to the *FEniCS* routines, are integrated. As already discussed in the section 3.5.1, FEniCS is an open source software package that offers a complete platform for solving PDE with the use of FEM. For the 3D computational mesh generation relative to the system configuration our code instead integrates Gmsh, which is an again open-source computer-aided engineering platform which operates on the basis of parametric inputs. We have coded in *Python* an interface which transforms the system configuration in a Gmsh input file (i.e. .geo format, see the Gmsh manual at the web page [79]) driving the mesh building. This interface allows the interaction between the FEM part and the MD part of the code. Finally, the particle-like Molecular Dynamics technique extracts the forces from the FEM continuum solution in the so-called *Coupled MD-FEM technique*. The steps of the simulations are analyzed in the following.

Computational domain.

Figure 2 shows the procedure to simulate the system evolution. A number of particles with their initial position and velocities, at the instant t_0, are considered. The first step of the simulations is to create, through the functionality of Gmsh, the mesh relative to the spheres (which represent the particles) embedded in the box (which represents the micro-fluidic channel)

including also the electrode geometries. All these portions of the numerical domain are merged in a single mesh, but it is necessary to identify and label them in a univocal way. Note that the dimensions of the particles and simulation box entities as well as the local resolution of the mesh in the different geometric elements can be defined independently.

FEM solutions and forces' estimates.

The second step is the solution of Laplace's problem, which is a prerogative of FEniCS. Dirichlet boundary conditions for the applied potentials on the electrodes and on the micro-channel top surface are used (see also Chap. 5), whereas Neumann boundary conditions are used for most other exterior boundaries to model their electrical insulation. Eventual periodic boundary conditions can be also activated if necessary. Using the *FEM* solution (i.e. the distribution of the complex potential in the space), by applying some FEniCS functionalities the following quantities are calculated:

- the values of the electric field;
- the MST by Eq. (1.27);
- $\langle \boldsymbol{F}^{MST} \rangle$ by Eq. (1.29).

After this computationally intensive part, the single particle interactions are calculated from the analytic expressions which depend on the velocity field of the fluid (see also Chap. 5).

Integration of the Equations of the motion and steric interactions.

The accelerations of the particles from the resulting forces are calculated and the numerical integration of the equations of motion is performed by means of the Velocity Verlet method technique (Eqs (4.20) and (4.21)).

The MD step includes control instructions on steric particle-particle and particle-wall interactions, which can be also considered as particular particle-particle interactions. Indeed, particles must never exceed the walls of the simulation box in their dynamics. Moreover, particles must not penetrate each other. For each MD step, checks are carried out: if one or both of these events occur, one check modifies the velocities and positions of the particles as explained below. The interaction between the particles and the walls is conceived in terms of an elastic impact: if a particle is found to have crossed the wall of the box in an MD step, its center is associated with a new value of speed (the opposite vector with respect to the one it had) and with the position occupied before crossing the wall. In the case of overlapping between particles, they are separated from each other, along the center-center direction, by a minimum distance so that they do not penetrate each other. Unlike in the case of particle-wall interaction, the check in this case does not change the particle speeds but only their positions. In other words, the problem is not treated in terms of elastic impact. This procedure is motivated by the presence of the drag force which depends on the speed.

It is assumed that the drag force strongly influences the particle-particle interaction modifying immediately the effects of the elastic impact. Such procedures avoid non-physical situations, which, among other, lead to conflicts in the generation of the mesh of the box and sub-domains at the FEM computational phase. See Appendix E for more details.

It is evident that MD-FEM coupling implies considerable computational resources, since the result obtained in a calculation cycle constitutes the initial condition of a further cycle relative to the following time step and both re-meshing and FEM procedures have to be performed at each iteration cycle. In order to optimize simulation times, the calculation of the e.m. force is decoupled from the analytical calculation of other forces (which is significantly faster). The e.m. forces usually show appreciable variations on time scales larger with respect to the optimal values of the MD increment Δt, which in turn is ruled by the other forces and steric interactions. Consequently, two time steps are introduced: Δt, already seen in the equations of the Velocity Verlet algorithm, which optimizes the calculation of the drag and lift forces and of steric interactions, and Δt_{DEP}, i.e. the time interval between one re-meshing and FEM calculation and the subsequent one. The first type of cycle is performed for $t = n\Delta t$ while the second type is performed for $t = n_{DEP}\Delta t_{DEP}$, where n and n_{DEP} are integers greater than zero, such that $n/n_{DEP} = \Delta t_{DEP}/\Delta t$.

This decoupled method is clearly more efficient. Figure 4.1 shows a block diagram of this MD-FEM algorithm.

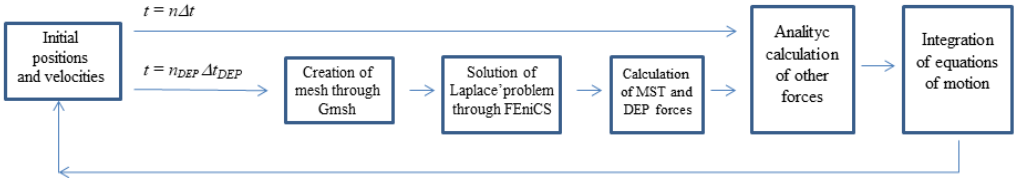

Fig. 4.1 Block diagram of MD-FEM algorithm. n and n_{DEP} are integers greater than zero such that $n/n_{DEP} = \Delta t_{DEP}/\Delta t$.

4.4 Conclusions

In this section we have described the MD-FEM algorithm implemented in our code for the simulation of EMPs dynamics. The formalism here described is appropriate for the prediction of the translational motion of the particles. In the next chapter, we apply the method to realistic systems of EMPs which can be experimentally realized also for practical application in the field of cell sorting. We note that additional (minor) formalism extension (Sec. 5.1), dealing with the external interactions, is needed for the particular application described in the following; whilst the method here presented could be easily generalized for other EMPs' systems. We notice that external interactions are somewhat typical of the given realization of the EMP system as a consequence they need in any case an "ad hoc" formulation.

Chapter 5

Simulated evolution of EMPs systems

This Chapter focuses on the theoretical study of the dynamics of spherical EMPs suspended in a colloidal solution in the presence of a non-uniform variable electric field. The numerical simulations of the model system aim at providing predictions of both stable configurations of the particles and their dynamics in fully three-dimensional configurations, minimizing the approximations usually considered in models of mutual interactions.

As cases of study that will be deeply analyzed, systems of practical interest have been chosen consisting of biological cells dispersed in a colloidal solution (of which the typical characteristics of interest are reported in the literature) that flow into a microfluidic channel in the presence of electromagnetic fields. In Chap. 1 it was seen that the dielectrophoretic force has the potential to manipulate micrometric particles according to their morphological and dielectric characteristics. This potential could be in principle exploited in the clinical field to separate/select/capture the so-called Circulating Tumor Cells (CTCs) in a hematological sample with high resolution and sensitivity. According the discussion reported in section 1.3.1 for generic particles, in sorting operation mode two types of cells (one of them tumoral) are suspended in a colloidal solution within a microfluidic device and subjected to a non-uniform variable electric field, and its frequency can be chosen for the capturing and

separations in a way that the tumoral type experiences p-DEP and the second type experiences n-DEP. For further details, Appendix C contains: a more accurate definition of CTCs, a discussion on their clinical effects and on the role that their study can play in the diagnostic and prognostic fields, a qualitative discussion on microfluidic devices based on dielectrophoresis. The examples of the method's application will focus on DEP induced translation of spherical particles (in particular a dielectric model of: MDA-MB-231 tumor cells, B-Lymphocites and mixtures of them).

A detailed study is carried out, with a non-approximate calculation of the forces, which are estimated by integrating the MST over the surfaces of the particles. As presented in the previous chapters, the evolution is simulated by techniques borrowed from MD, whilst the FEM is applied to obtain self-consistent numerical solutions of the partial differential equations regarding the e.m. field. The Coupled MD-FEM algorithm and its implementation in the FEniCS environment is used.

This chapter consists of the following sections:

5.1 *Single particle external interactions*: the forces (in addition to the electromagnetic forces) to which the particles are subjected in the microfluidic channel are defined and described;

5.2 *Particle model*: a model taking into account the structural complexity of cells is introduced;

5.3 *Model validation for simple configurations*: simulations carried out on simple configurations are presented in order to validate the implemented model;

5.4 *MD-FEM simulations results in many particle systems*: simulation results are presented and discussed.

5.5 *Geometry' effects:* results of simulations carried out with geometries different from those of section 5.4 are presented.

5.1 Single particle external interactions

For realistic simulations, other forces must also be taken into account in addition to the e.mec. forces. EMPs, in usual conditions induced in manipulation experiments, are not only subjected to e.m. fields, but also to hydrodynamic pressure fields and to gravity. These external interactions act on single particles and for spherical ones can be expressed as analytical expressions of their kinetic variables. We note that in general the colloidal solution containing the EMPs is not static, although some case studies will be discussed in the limit of static solutions. In the following the formulation of single particle forces included in the simulation method is given.

Drag force

The viscous drag force stemming from the viscosity of the medium is given for a spherical object by [26, 80]:

$$\boldsymbol{F}_{drag} = 6\pi\mu R(\boldsymbol{u} - \boldsymbol{v}) \quad (5.1)$$

where μ is the dynamic viscosity, $\boldsymbol{u}$ is the local velocity of the fluid and $\boldsymbol{v}$ is the instantaneous velocity of the particle. The Eq. (5.1) is referred as the Stokes's law [81].

Lift force

The lift force, due to the non-negligible velocity gradient of the fluid across the particle surface, is also present [82, 83] and it is particularly important close to the sidewalls of the channel containing the solution. In the application of MD-FEM method in this Thesis, a micro-fluidic channel with parallel sidewalls and small dimensions will be considered, where the fluid flow can be assumed to be laminar since the Reynolds-number is of the order of 10^{-1}. In these conditions, the shape of the flow profile in the vertical direction of the channel depends by the chamber height h. The analytical solution of the fluid velocity field is the parabolic flow profile [28]:

$$u(z) = 4\, u_{max}\, \frac{z}{h}\, \frac{h-z}{h}, \quad (5.2)$$

where z is the distance of the particle center from the bottom of the channel and

$$u_{max} = u\left(\frac{h}{2}\right)$$

is the velocity of the fluid at the center of the channel, as shown in Fig. 5.1. It is important to note that:

$$u(0) = u(h) = 0.$$

The expression of Eq. (5.2) can be written also in terms of the average velocity $\bar{u}$ [84]:

$$u(z) = 6\,\bar{u}\,\frac{z}{h}\,\frac{h-z}{h}. \tag{5.3}$$

In fact, by Eq. (5.3):

$$\frac{1}{h}\int_0^h u(z)\,dz = \frac{1}{h}\int_0^h 6\bar{u}\,\frac{z}{h}\,\frac{h-z}{h}\,dz = \bar{u}. \tag{5.4}$$

The lift force arises because of the fluid viscous flow on particles close to a solid plane, causing their levitation [85] and, in this particular channel geometry, it is perpendicular to the bottom and directed towards the center of the channel. Its intensity is directly proportional to the gradient of the curve describing the fluid velocity (Eq. (5.2)) and it takes the following form [86]:

$$F_{lift} = \frac{C\mu R^3}{(z-R)} \frac{d}{dz} u(z)\Big|_{z=0} = \frac{4C\mu R^3 u_{max}}{h(z-R)}, \quad (5.5)$$

where C=0.153 [87].

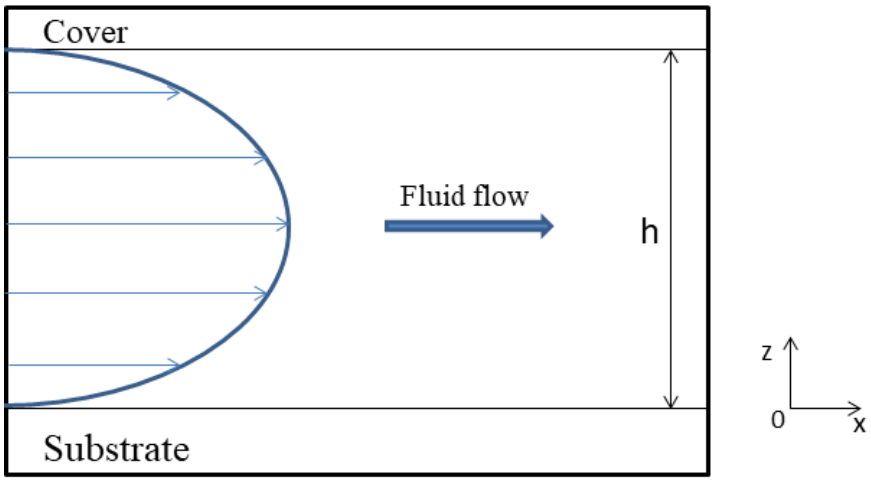

Fig. 5.1 Parabolic velocity profile for a fluid flowing through a microfluidic channel of height h; $u(0) = u(h) = 0$; $u_{max} = u\left(\frac{h}{2}\right)$.

Gravitational force

The summation of gravitational force acting on spherical cells and the buoyancy force (due to the density of the surrounding fluid and the amount of fluid displaced by the particles) is:

$$\boldsymbol{F_{g,B}} = \frac{4}{3}\pi R^3(\rho_p - \rho_m)\mathbf{g}, \quad (5.6)$$

where ρ_p and ρ_m are the particle and suspension medium density respectively and **g** is the acceleration due to gravity.

Summarizing from the considerations of this section, the forces acting on the particles are:

along *x*-axis: $\langle F_x^{MST} \rangle$ and viscous drag force;
along *y*-axis: $\langle F_y^{MST} \rangle$ and viscous drag force;
along *z*-axis: $\langle F_z^{MST} \rangle$, viscous drag force, lift force, gravity and buoyancy force.

5.2 Particle Model

It is clear from Eq. (1.32) that it is necessary to know the complex dielectric constant of the particles at the operational angular frequency ω for calculating the dielectrophoretic force. In the application examples of the MD-FEM method we consider biological cells, therefore a derivation of the dielectric parameter for such particular system is necessary. The expression first introduced by Pohl is based on modeling the cell as a solid spherical dielectric particle suspended in a fluid medium. CTCs are often modeled as rigid spheres [88]. However, biological particles are complex and heterogeneous structures with multiple layers having distinct electrical properties [89]. The cells have in general a so-called *cell wall*, this is a structure that provides rigidity and shape retention and also represents a physical and chemical barrier. *Protoplasts* are particles prepared by treating

walled cells with special enzymes to digest the wall. Their form is typically balloon-like. They are very fragile due to the absence of cell wall. Such protoplasts can be outlined as particles with a conductive fluid interior (cytoplasm) enclosed by a very thin capacitive layer (membrane). Typical mammalian cells are structurally similar to protoplasts [90, 91], although smaller and less fragile: most of them lack indeed the cell wall, consist of a conducting cytoplasm surrounded by an insulating membrane and exhibit a very similar polarization response. The cell membrane is a semipermeable phospholipidic bi-layer with the presence of some internal specific proteins. It is very thin (about 10 nm). Biochemistry and biomedicine investigate the vital function of the cells which is severely dependent on the activity of the membrane cell. Indeed, the membrane promotes the two-way exchange for (i) life-sustaining nutrients and regulatory substances required by the cell's metabolism and (ii) waste materials excreted from the cell. It is important to investigate the membrane's average dielectric properties, with the aim of studying the behaviour of the cells when they undergo to an e.m. field. The drop in DC electrical potential that membranes can typically withstand without being damaged is typically about one volt, corresponding to an effective dielectric strength of $\sim 10^8$ V/m, a value that is sustainable in few, if any, dielectric insulating synthetic materials [23].

Since its phospholipidic nature, the membrane behaves like a very low loss capacitor, blocking low frequency electric fields and electric current from the cytoplasm, which is a quite complex aqueous ionic fluid containing the nucleus and other several functional organules.

On the basis of the above, in biological dielectrophoresis it is essential to adopt trusted dielectric models for protoplasts. A more realistic

model for cells has consequently been adopted in this work: the cell is represented by a spherical dielectric core and a spherical dielectric shell to account specifically for the dielectric properties (conductivity and permittivity) of the cytoplasm and of the membrane respectively. Despite the complexity of the cytoplasm, simplified models are usually adopted to overall describe the interior of cell system, taking into account the average dielectric properties of the cytoplasm itself. A homogeneous model with dielectric permittivity ε_{cyt} and ohmic conductivity σ_{cyt} is adopted. As well, the cell membranes are typically characterized by dielectric permittivity ε_{mem} and ohmic conductivity σ_{mem}. This shelled model is shown in Fig. 5.2(a). The liquid medium is similarly described by ε_m and σ_m. The complex permittivities of the cytoplasm, membrane and liquid medium are:

$$\tilde{\varepsilon}_{cyt} = \varepsilon_{cyt} - i\sigma_{cyt}/\omega,$$

$$\tilde{\varepsilon}_{mem} = \varepsilon_{mem} - i\sigma_{mem}/\omega,$$

$$\tilde{\varepsilon}_{m} = \varepsilon_{mem} - i\sigma_{m}/\omega.$$

The cell radius is R, *d* is the membrane thickness, the difference *R-d* is the cytoplasm radius.

The "effective electrical permittivity" $\tilde{\varepsilon}_{eff}$ method is applied taking into account the properties of these two different parts of the cell [92]: it can be shown that the induced electrostatic potential outside the particle, that is for

$|r| > R$, is indistinguishable from that of the equivalent, homogeneous dielectric sphere of radius R with permittivity $\tilde{\varepsilon}_{eff}$, as shown in Fig. 5.2(b).

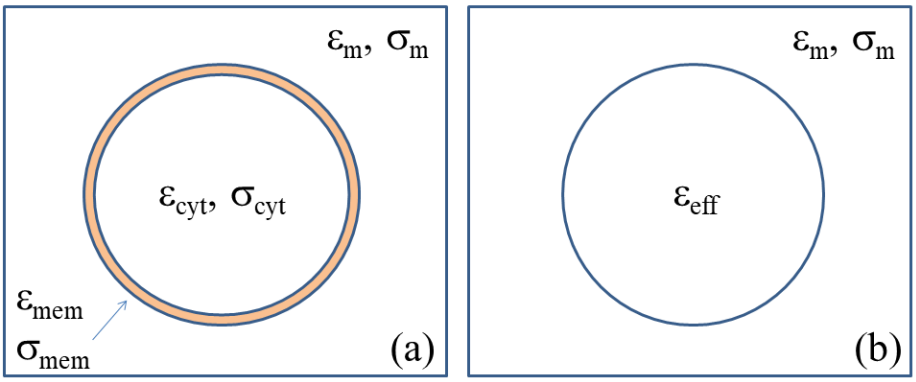

Fig. 5.2 (a): Spherical dielectric cell composed of the cytoplasm (inner volume) and the membrane (light brown shell). (b) Effective equivalent homogeneous sphere model ruled by the dielectric function $\tilde{\varepsilon}_{eff}$.

The particle is thus replaced by an equivalent and homogeneous sphere with a radius equal to that of the outermost shell but with different dielectric characteristics represented by $\tilde{\varepsilon}_{eff}$. The complex dielectric constant $\tilde{\varepsilon}_{eff}$ has the following form (see Appendix C):

$$\tilde{\varepsilon}_{eff} = \tilde{\varepsilon}_{mem} \frac{\left(\frac{R}{R-d}\right)^3 + 2\frac{\tilde{\varepsilon}_{cyt}-\tilde{\varepsilon}_{mem}}{\tilde{\varepsilon}_{cyt}+2\tilde{\varepsilon}_{mem}}}{\left(\frac{R}{R-d}\right)^3 - \frac{\tilde{\varepsilon}_{cyt}-\tilde{\varepsilon}_{mem}}{\tilde{\varepsilon}_{cyt}+2\tilde{\varepsilon}_{mem}}}. \qquad (5.7)$$

In the final analysis, the quantity $\tilde{\varepsilon}_p$ present in the equations in the preceding chapters must be replaced by the $\tilde{\varepsilon}_{eff}$ (for example in the definition of the CM factor of Eq. (1.15)).

5.3 Model validation for simple configurations

The simulations presented in this section concern a simple device configuration to validate our numerical approach based on the MD-FEM technique: the parallel plate capacitor. The electric field is generated by the two parallel electrodes separated by a distance h. The only component of electric field different from zero is that along the direction perpendicular to the plates and its value in module is:

$E=V/h$,

where V is the electric potential drop across the plates. The first system considered is a single particle immersed in a fluid present inside the capacitor. For this particle, the electrical parameters representative of the B-Lymphocites cell (which has been well characterized [93, 94]) are used. These and similar values for the liquid medium, typical for isotonic water solutions, are given in the Table 1.

	Permittivity (in unit of vacuum permittivity $\varepsilon_0 = 8.854$ F/m)	Conductivity (S/m)
B- Lymphocyte membrane	$\varepsilon_{mem} = 14.26$	$\sigma_{mem} = 1 \cdot 10^{-6}$
B- Lymphocyte cytoplasm	$\varepsilon_{cyt} = 59$	$\sigma_{cyt} = 0.31$
Liquid medium	$\varepsilon_m = 79$	$\sigma_m = 0.03$

Tab. 1 Electrical parameters of the cytoplasm and the membrane of B- Lymphocytes and of the liquid medium.

The properties of B-Lymphocites are [95]:

- radius: R = 3.3 μm;
- membrane thickness: d = 10 nm;
- mass density: ρ = 1065 Kg/m^3.

In the calculation, the drop of potential between the plates of the capacitor is V=10 Volt, while the frequency of the electric field is $\nu = 1\,MHz$ (the angular frequency is $\omega = 2\pi\nu$) and $h = 500\ \mu m$.

The DEP force values calculated by the approximate formula of Eq. (1.14) are equal to zero as the electric field is constant inside the capacitor. The force calculated by MST has instead values different from zero due to the alteration induced to the total electric field by the particle in the electrode proximity (see Ref. [17] for a complete discussion).

The results are compared with those of Ref. [17] to validate the MD-FEM approach. In this reference the calculations are made by Comsol Multiphisycs [50], which is a commercial solver and simulation software based on finite element analysis. It is important to note that in Comsol it is possible to use the function “dielectrophoretic force” present in its functions library. Figure 5.4 shows the comparison between the values of F^{MST} for several particle-electrode distance values present in Ref. [17] and the analogous values calculated by MD-FEM approach. The value of F^{MST} is stronger close to the plate and becomes less intense as it moves away.

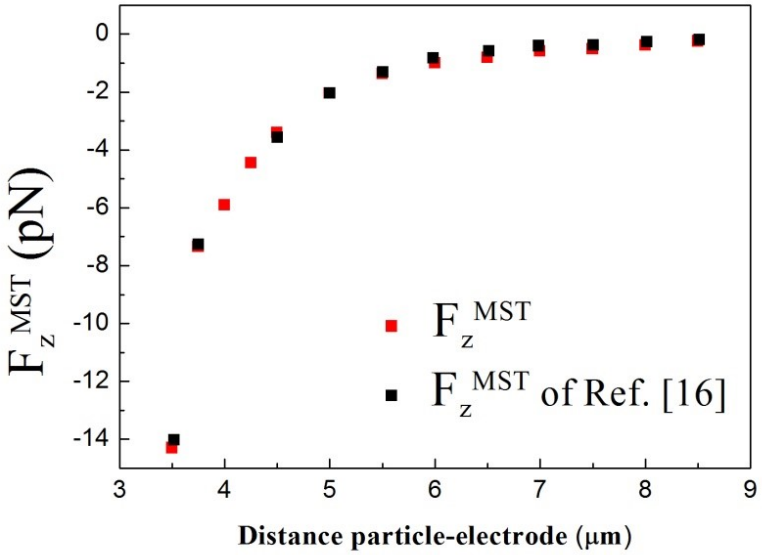

Fig. 5.3 Comparison between the values of F^{MST} present in reference [17], obtained by Comsol, and the values calculated in the Gmsh-FEniCS implementation of the e.mec. force calculation.

The results are very similar to the ones obtained by Comsol in Ref. [17], whereas small differences are due to the different meshes and numerical integration schemes employed.

The second check of our code is done considering two particles (B-Lymphocites) in a capacitor like configuration of the device similar to that of the previous case. In the presence of an electric field, the formation of chains of particles is predicted [96]. It consists in the end-to-end attachment of particles, which assume a formation similar to that of a chain of pearls. The formation of particle chains is a phenomenon mainly due to the electrostatic interactions among the particles under the effects of the electric field. It occurs because the particles acquire induced dipole moments under the field action: if two particles are close to each other, the positive charge of the dipole of the first particle interacts with the negative charge of the dipole of the second; hence, they experience an attractive force which links them together. Pearl chains are formed only when the particles come close to each other and this phenomenon can be neglected in the dilute solution limit, when the particles are separated by large distances. As for elongated single particles (including biological cells), a frequency dependent orientation effect is expected for chains of homogeneous conducting dielectric spheres suspended in fluids and subjected to an electric field [97]: chains are predicted to align with the vector joining the centers parallel to the field direction. The formation of chains is a common occurrence in DEP experiments on biological cells. In this analysis, we consider the kinetics of chain formation for Lymphocytes.

The drop of potential between the plates of the capacitor is V=10 Volt, the frequency of the electric field is $\nu = 1\ MHz$, $h = 100\ \mu m$. Figure

5.4(a) shows the particles in the initial configuration, at time t=0 sec. Figures 5.4(b), 5.4(c) and 5.4(d) show the particles in successive instants, after application of a uniform electric field directed along the z-axis: a chain forms, due to the polarization of the particles, and also aligns itself with the electric field as time passes.

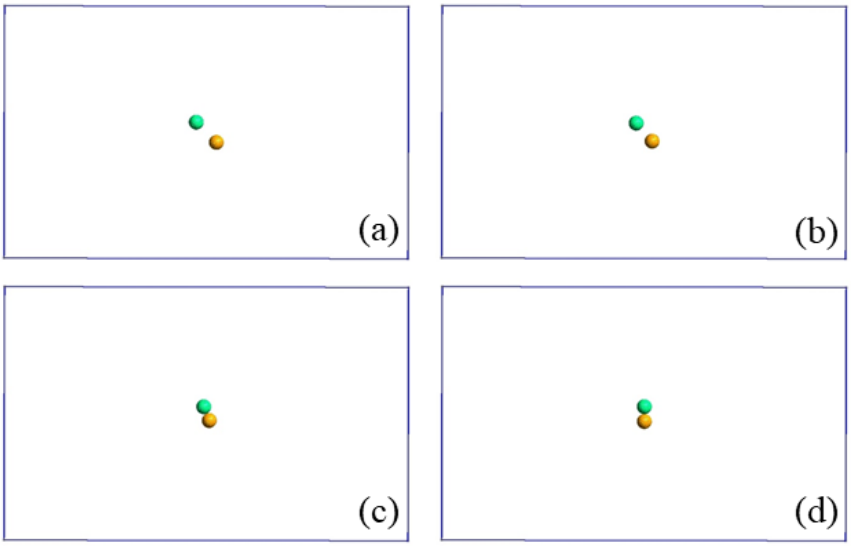

Fig. 5.4 Snapshots of a simulation of two particles in a parallel plate capacitor for t =0, 0.1, 0.15, 0.21 sec ((a), (b), (c), (d) respectively). The particles attract and form a chain that aligns with the electric field and remains in this stable configuration for the rest of the simulated evolution.

5.4 MD-FEM simulation results in many particle systems

In this section some results of the application of our MD-FEM method to many-particle systems are discussed. They reproduce the condition of real manipulation experiments where DEP forces are induced on cells.

The non-uniform electric field used in DEP applications is typically produced by electrodes with feature size in the scale of microns in order to reduce suitably the value of the applied voltage [98]. Several electrode geometries have been developed according to the particular application scopes. Lithography techniques are typically used to pattern planar electrodes on the bottom of the micro-channel and examples of planar electrode designs include inter-digitated [99], castellated, spiral [100], curved [101], oblique [102], quadrupole [103], matrix [104] and polynomial [105] electrodes.

In particular, the prototype devices for cell capture/separation have planar electrodes. The devices are composed of the following parts:

- a micro-fluidic channel (where the colloidal solution flows);

- electrodes made with a geometry such as to generate a non-uniform electric field when they are subjected to an alternating electric signal.

In order to apply the method to a particular application example, the geometry used in this work is the inter-digitated circuit (shown in Fig. 5.5) which is assumed to be incorporated in one boundary of the micro-fluidic channel.

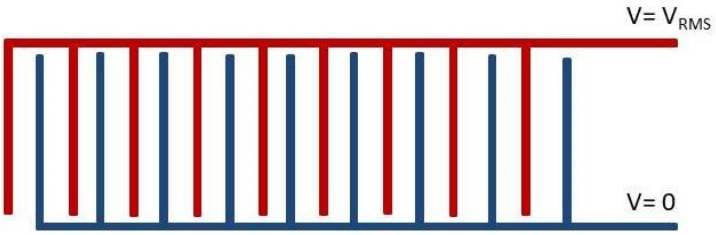

Fig. 5.5 Schematic of an inter-digitated circuit. An alternating signal is applied to the electrodes in red while V=0 is imposed to electrodes in blue.

An alternating signal is applied to the odd-position electrodes (shown in red in Fig. 5.5), while the even-position electrodes (blue in Fig. 5.5) are potential-free (V=0). The simulated system consists of cells in colloidal solution in a liquid medium that flows through the microfluidic channel. The channel is represented in the simulations by a box (parallelepiped): in its base the surface mesh region is identified, in which the electrical signal is applied.

It is necessary to make some assumptions to perform the simulations:

- each individual “finger” comprising the inter-digitated electrode array is sufficiently long such that the fringe effect at the end of the fingers is negligible;

- ohmic heating due to the applied voltage is not large enough to cause flows or changes in the physical constants [106, 107] (an approximate calculation shows that the temperature rise for this type of application will be less than 0.15 ◦C; consequently, this is a valid assumption [108]).

The micro-fluidic chamber is simulated according to these assumptions. The channel is composed by N electrodes. Electrode thickness was ignored. Figure 5.6 shows a schematic representation of the geometry of the simulations, which includes the substrate, channel cover and two fingers of inter-digitated electrodes. W_e is the width of the electrodes, W_g is the width of the gap between a pair of electrodes and h is the height of the micro-channel. Appendix C (Section C.2) provides some details on the materials typically used in the construction of such microchannels and on the typical prototype dimensions.

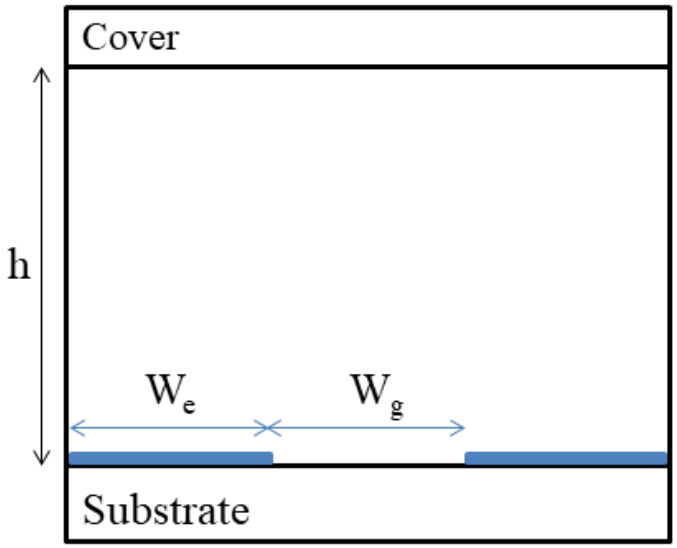

Fig. 5.6 Schematic of the computational domain (limited for simplicity to only two electrodes whilst in the simulation N electrodes are considered). The electrodes (in blue) have a width W_e and are separated by a gap of width W_g.

The results of simulations of the dynamics of the system composed by a colloidal solution of cells in the microfluidic system with interdigitated electrodes are presented below. Two types of simulations are performed:

- (a) twenty MDA-MB-231 cells under p-DEP conditions;
- (b) ten MDA-MB-231 cells and ten B-Lymphocites, in p-DEP and n-DEP respectively.

5.4.1 Case (a): MDA-MD-231 cells

In the case of simulation (a), the electrical parameters representative of MDA-MB-231 cells [109] are used. Table 2 shows these values and the medium analogues.

	Permittivity (in unit of vacuum permittivity $\varepsilon_0 = 8.854$ F/m)	Conductivity (S/m)
MDA-MB-231 membrane	$\varepsilon_{mem} = 24$	$\sigma_{mem} = 1 \cdot 10^{-7}$
MDA-MB-231 cytoplasm	$\varepsilon_{cyt} = 50$	$\sigma_{cyt} = 0.2$
Liquid medium	$\varepsilon_m = 79$	$\sigma_m = 0.03$

Tab 2. Electrical parameters of the cytoplasm and the membrane of MDA-MD-231 cells and of the liquid medium.

The properties of MDA-MB-231 cells are [94, 109]:

- radius: R = 6.2 μm;
- membrane thickness: d = 10 nm;
- mass density: ρ = 1060 Kg/m^3.

The medium liquid is characterized by:

- dynamic viscosity: μ = 0.001 Pa sec;
- maximum velocity: u_{max} = 100 μm/sec;
- mass density: ρ = 1000 Kg/m^3.

The following parameters are also used for the box simulation:

- width of the electrodes: $\mathrm{We} = 40\ \mu m$;
- gap between them: $\mathrm{Wg} = 40\ \mu m$;
- dimensions of the microchannel: (960x60x100) μm^3 (for the length, depht and height, respectively);
- number of electrodes: 12.

The time steps, calibrated in order to ensure stability and time accuracy to the explicit MD integration method (no significant improvement can be achieved reducing further these values), were:

- $\Delta t = 3 \cdot 10^{-5}\ sec$;
- $\Delta t_{DEP} = 6 \cdot 10^{-4}\ sec$.

The e.m. force varies as a function of the magnitude and frequency of the input voltage and a high voltage should be applied to generate intense DEP forces, but excessive loading can cause cell damage (harm cell viability) [110] or electro-thermal flows. For these reasons, a tradeoff between DEP

intensity and safe conditions for the biological system was considered in the experimental conditions, and usually voltages less than 10 $V_{p\text{-}p}$ were applied. The following values have been used in the simulation:

- potential applied to the set of odd electrodes: V=5 Volt;
- potential applied to the set of odd electrodes: V = 0;
- frequency: $\nu = 1\ MHz$.

The boundary conditions, in addition to the predefined voltages on the electrode surfaces, consist of insulation (Neumann-type boundary condition) on the channel walls, because of the large difference between the permittivities and the conductivities of the liquid medium and the channel material, which is either glass or polymer-based in the majority of the cases. Neumann type boundary conditions were also applied in the surface regions of the micro-channel base that were not covered by electrodes.

As initial condition, the particles were arranged in a configuration characterized by random positions, concentrated in the left side of the channel, corresponding to about a third of the total volume (i.e. a local injection of particles was reproduced).

During the simulation, the self-consistent FEM solutions of Eq. (1.32) were calculated considering the instantaneous configuration of the system. As an example in the Fig. 5.7 the solution of the time harmonic Laplace's problem at t = 0.6 sec, relatively to four sections of the microfluidic channel, is shown: the first crosses the channel in x = 60 μm plane, the second in x = 220 μm, the third in x = 540 μm and the fourth in x = 880 μm. In this instant, some particles are located at the edges of the

electrode centered in x = 40 μm and of the second centered in x = 220 μm. The perturbations to the potential generated by the external field due to the particle presence (and corresponding polarization) can be seen in the sections.

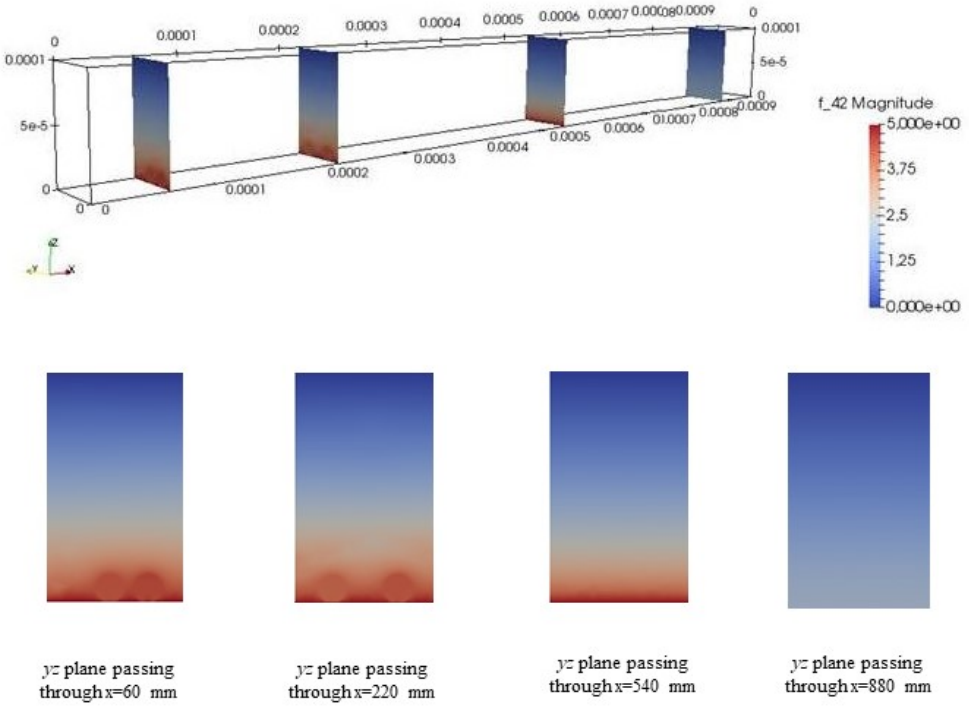

Fig. 5.7 Solution of Laplace's problem at t = 0.6 sec. Top panel, the schematic of the microfluidic channel in which the solution of the Laplace equation relative to the sections passing through x = 60, 220, 540, 880 μm is visible. Bottom panel, the front views of the slices themselves; in the first two, variations in potential due to the presence of particles can be observed.

As can be deduced from Fig. 5.7, the gradient of the electric field is more intense in the areas close to the base of the microfluidic channel, and in particular in the regions close to the edges of the electrodes. As a result,

forces are more intense in these areas. In the snapshots of planes passing through x = 60 μm and x = 220 μm, it is possible to clearly identify the effects on the electrical potential due to the presence of particles occupying the regions close to the edges of two electrodes.

An anticipation of the behavior of the cells can be given by the real part of the Clausius-Mossotti factor, f_{CM}. It refers to the calculation of the standard DEP force in the approximation of isolated particles on an infinite medium (diluted solution limit), but can nevertheless provide a guideline in the most realistic cases analyzed with this simulation. Figure 5.8 shows the real part of f_{CM} of MDA-MB-231.

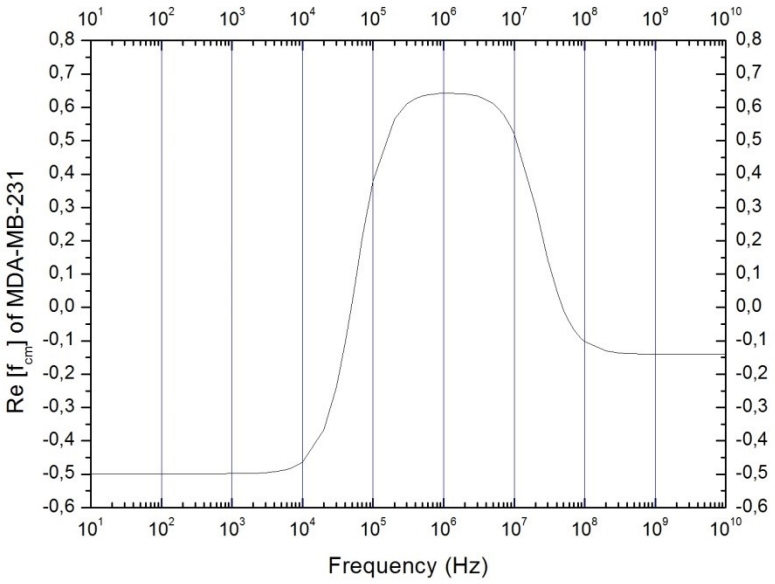

Fig. 5.8 Re$\{f_{CM}\}$ calculated with the dielectric model of the MDA-MB-231 cell at a medium conductivity σ_m = 0.03.

For the frequency used in this simulation ($\nu = 10^6$ Hz), Re$\{f_{CM}\}$ = 0.643. This indicates that MDA-MB-231 cells will be subject to p-DEP and will undergo attractive forces from the zones in which the electric field is greater.

Figure 5.9 shows snapshots of the simulation results at several instances of time, from t=0 sec to t=5.1 sec (different colours are used to identify the cells but, of course, they are identical in terms of dielectric properties).

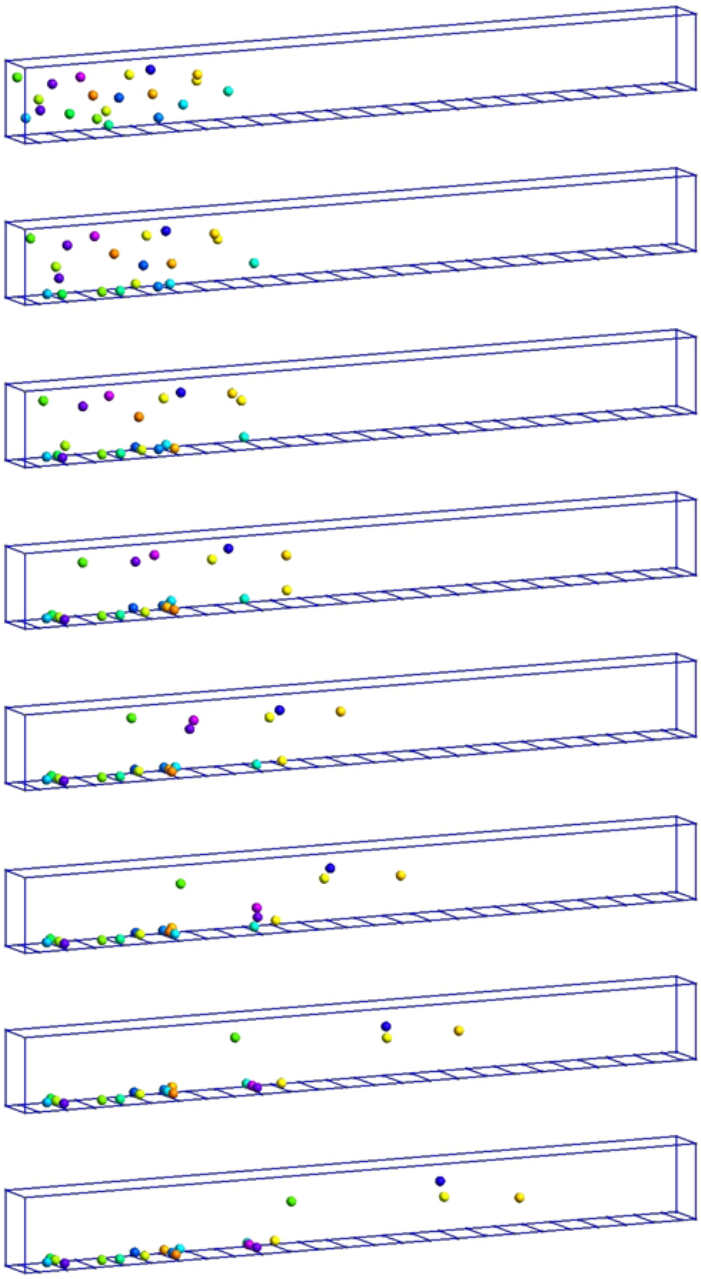

Fig. 5.9. Snapshots of the simulated system (N=20 MDA-MD-231 cells in a flowing colloidal solution) for t =0, 0.3, 0.6, 1.5, 2.4, 3.3, 4.2, 5.1 sec (from upper panel to lower panel). The dimensions of the microchannel are $(960\text{x}60\text{x}100)\ \mu m^3$ and the number of electrodes is 12. The cells are subjected to a p-DEP, i.e. they will tend to move towards high electric field regions.

The simulations carried out on this system show, as expected, that the particles experience p-DEP and, in particular, they are attracted by the edge of the electrode. The particles which have lower distance from the electrode are attracted more strongly since the gradient is greater in these regions. In the topmost part of the channel, the field is more uniform, so that particles in this region of the device will be subjected to less intense attractive forces and they continue to advance with minor height reduction. When their altitude with respect to the channel base is sufficiently small and they reach zones where the non-uniformity of the field is greater, the attraction becomes stronger and the trapping effect becomes evident. Figure 5.10 shows a detailed analysis of the behavior of a particle that, reached a sufficiently low height, reverses the direction of motion along the horizontal axis, being attracted by the edge of an electrode. The particle is circled in the first snapshot of the Fig. 5.10.

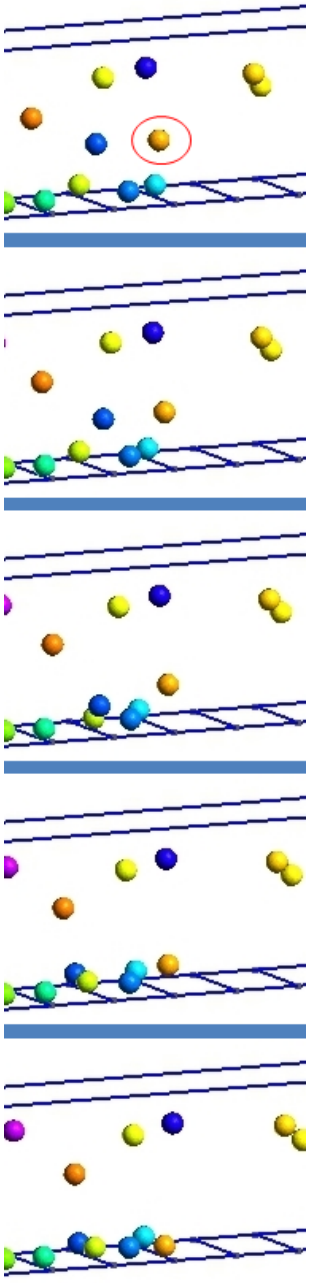

Fig. 5.10 Snapshots for t = 0.3, 0.36, 0.42, 0.48, 0.54 sec (from upper to lower). The particle that reverses the direction of motion along the horizontal axis is circled in the upper snapshot.

Particles that reach the base of the device and thicken close to the edges of the electrodes have small variations of their position as a result of the various forces acting on them; anyway it is correct to say that they remain trapped in these regions.

An additional behavior that can be observed, in the case of spatial proximity between particles, is the chain formation in dynamical conditions caused by mutual polarization. Figure 5.11 shows a more detailed analysis of the behavior of a pair of particles that attract each other form a pair (chain), which moves as a single object and is attracted by the edge of an electrode. The pair is circled in the first snapshot of Fig. 5.11. It is possible to note that after the pair formation in the time evolution the two particles present a cohesive motion until they reach the bottom, whose influence could, of course, overcome particle-particle interactions.

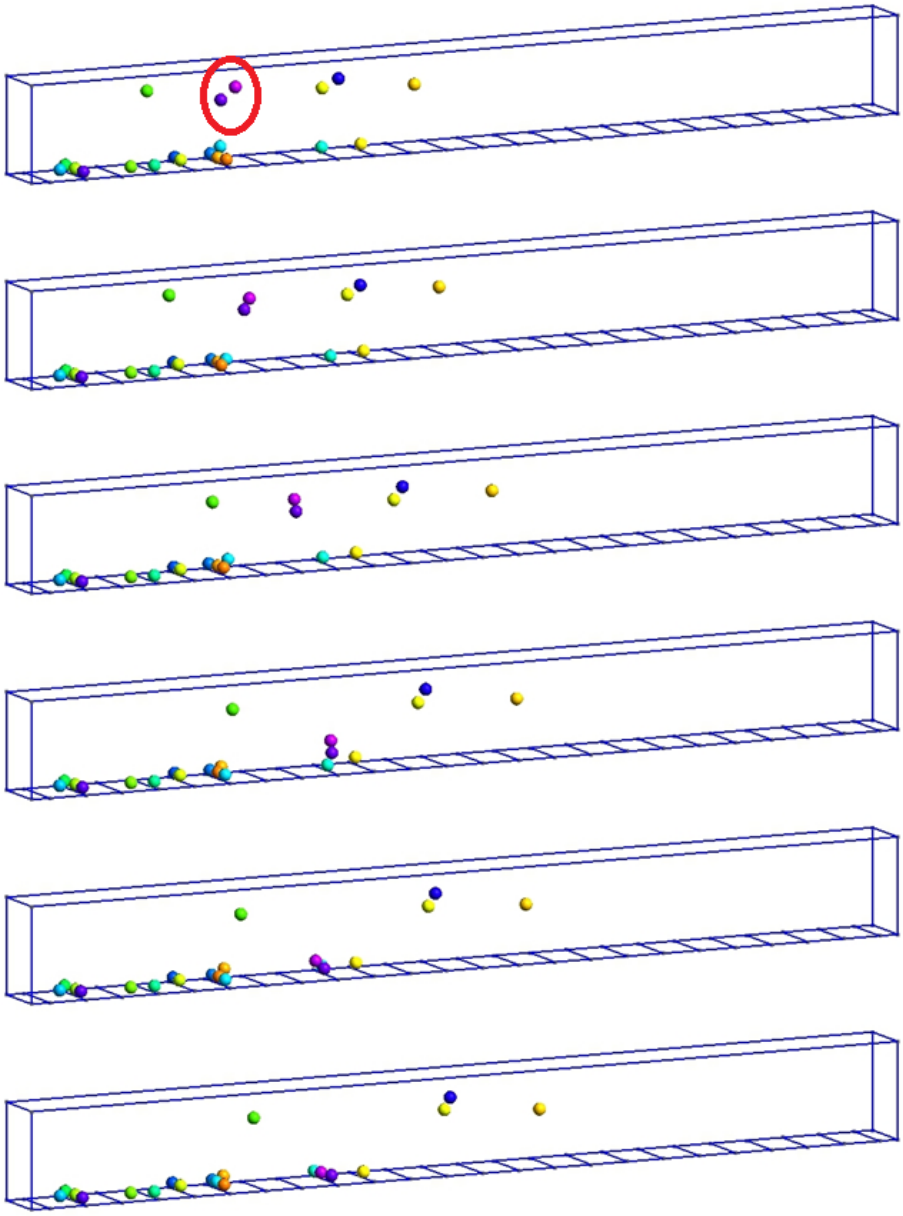

Fig. 5.11. Snapshots for t = 2.1, 2.4, 2.7, 3, 3.3, 3.6 sec (from upper to lower). The pair of particles that form the chain is circled in the upper snapshot.

5.4.2 Case (b): two-cell system MDA-MB-231 and B-Lymphocites

With respect to simulation (b), the morphological and electrical characteristics of both cell types have already been listed (see section 5.3 for B-Lymphocites and section 5.4.1 for MDA-MD-231). The specifications of the liquid medium, the width of the electrodes, the distance between them, the time steps (Δt and Δt_{DEP}) and the applied electric potential values are unchanged. The number of electrodes this time is N=10 and thus the dimensions of the microchannel are $(800\text{x}60\text{x}100)\ \mu m^3$ (for the length, depth and height, respectively).

A relevant parameter that has been modified with respect to the previous study of twenty identical particles is the oscillation frequency of the electric field: in this second simulation, it has been set to $\nu = 10^5$ Hz. Figure 5.12 shows $\text{Re}\{f_{CM}\}$ of both cell types (see Appendix F for details).

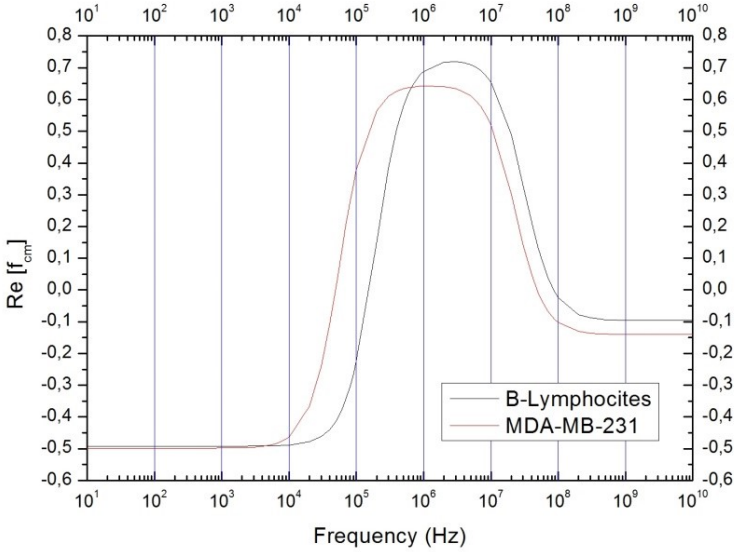

Fig. 5.12 Re$\{f_{CM}\}$ of the MDA-MB-231 and B-Lymphocites at a medium conductivity $\sigma_m = 0.03$.

For the frequency used in this simulation, $\nu = 10^5$ Hz, Re$\{f_{CM}\}$ has the following values for the two cell types:

MDA-MB-231: $\text{Re}\{f_{CM}\} = 0.378$;

B-Lymphocytes: $\text{Re}\{f_{CM}\} = -0.225$.

They indicate that MDA-MB-231 cells will be subject to p-DEP and attracted to areas where the electrical field intensity is higher (that is from the region near the electrodes and especially from their edges), while B-Lymphocytes will be subject to n-DEP and rejected from this regions.

Figure 5.13 shows the simulation results at several instances of time, from t=0 sec to t=5.1 sec.

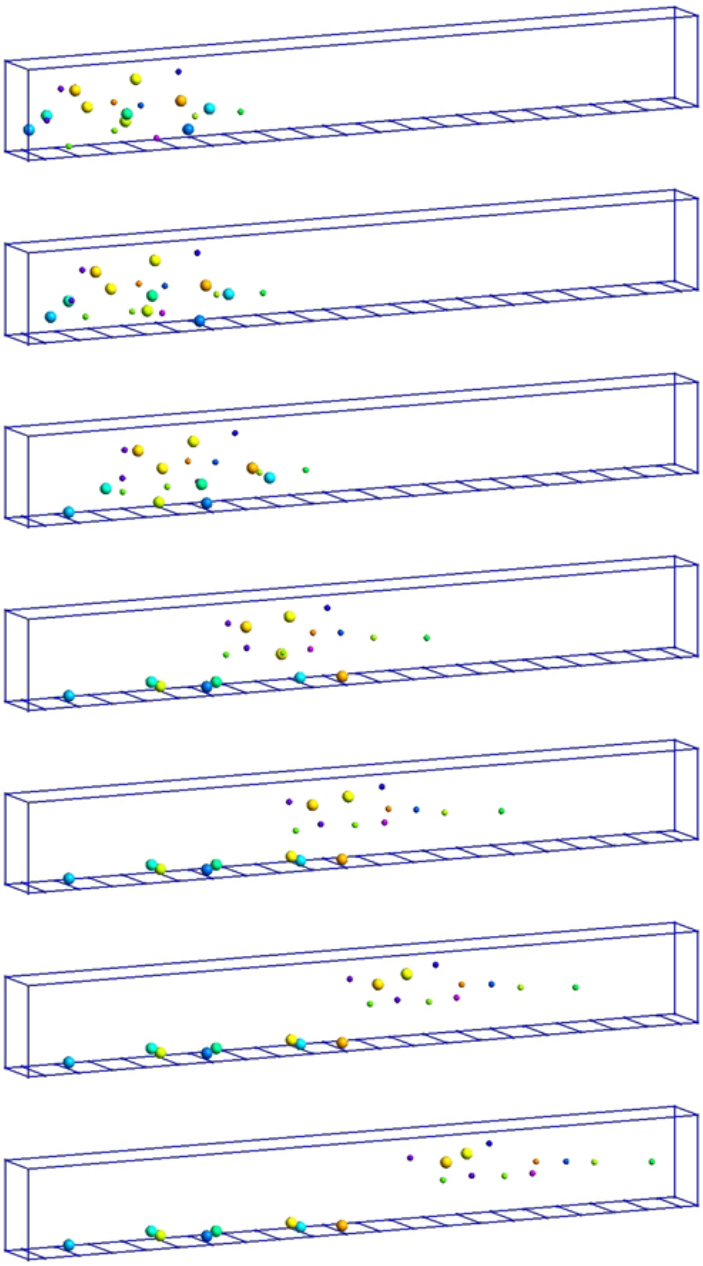

Fig. 5.13 Snapshots of the simulated system (ten MDA-MD-231 cells and ten B-Lymphocites in a flowing colloidal solution) for t =0, 0.6, 1.2, 2.4, 3.3, 4.2, 5.1 sec (from upper to lower). Dimensions of the microchannel: (800x60x100) μm^3; number of electrodes: 10.

The simulation follows qualitatively the behaviour predicted for the two values of Re$\{f_{CM}\}$. The MDA-MB-231 cells are attracted to the electrodes as in the case of simulation (a), while B-Lymphocites are rejected and do not reach the base of the device. This behavior confirms the separation/capture potential of this type of electrophoretic device.

It is interesting to note that, due to the difference in frequency value, the Re$\{f_{CM}\}$ value relative to MDA-MB-231 cells in this second simulation (equal to 0.378) is lower than in the first simulation (equal to 0.643), so the standard DEP forces are on the average less intense this time.

In simulation (a), in which only MDA-MB-231 cells are present, all cells reduce monotonically their altitude over time, due to gravity and e.m. forces (p-DEP). It is important to note that in this second simulation two MDA-MB-231 cells, precisely the ones that have higher positions, do not reduce their elevation monotonically. Analysing the numerical values of the z-coordinate for each time cycle, we notice that in some time periods (for example around t=3.5 sec) the height of these two particles increases slightly. This behaviour is due to particle-particle interactions involving these two MDA-MB-231 cells and some B-Lymphocytes that are in their spatial proximity. The B-Lymphocytes are rejected by the bottom of the device (n-DEP) and they in turn push away from the electrodes the MDA-MB-231 cells. In order to quantify this effect, we analyse in detail the motion of the particle with the highest altitude during the entire simulation. Figure 5.14 shows the z-coordinate of this particle as a function of the time in one of the time intervals in which a non-monotonic variation of its height is provoked by the interaction with the n-DEP type cells. The graph shows values taken at regular intervals of 0.06 seconds.

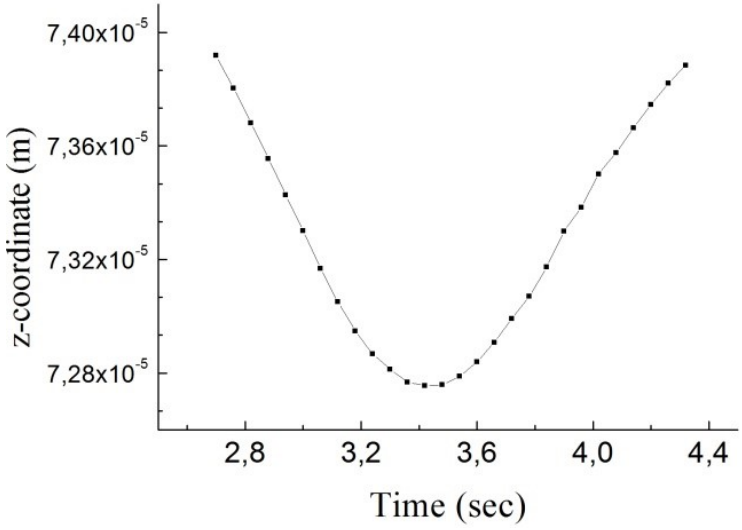

Fig. 5.14 z-coordinates of the particle with the highest altitude during the entire simulation, in a time interval where it presents a non-monotonic change in altitude.

To highlight this phenomenon, we carried out an additional simulation similar to that of the Fig. 5.4 (relative to a pair of B-Lymphocytes), in which there are one MDA-MB-231cell and one B-Lymphocyte. The frequency is 10^5 Hz (MDA-MB-231 in p-DEP, B-Limphocyte in n-DEP), as the previous simulation. The results are shown in Fig. 5.15, for time values equal to those of Fig. 5.4. We note that the particles repel each other, contrary to the case of Fig. 5.4, where two identical particles in p-DEP conditions attract forming a chain.

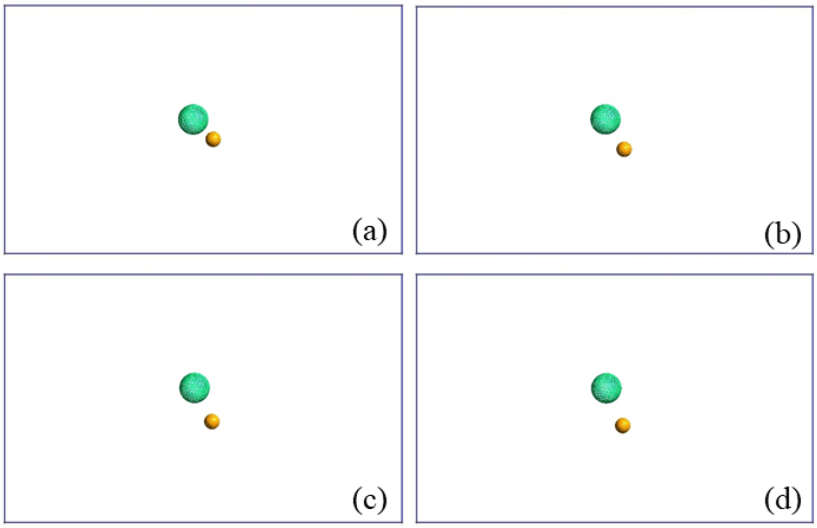

Fig. 5.15 Snapshots of the simulation of one MDA-MD-231 cell and one B-Lymphocyte in a parallel flat face capacitor for t =0, 0.1, 0.15, 0.21 sec ((a), (b), (c), (d) respectively). Contrary to the case of the Fig. 5.4, the particles repel each other.

The behaviour of the two cells can be qualitatively explained by considerations regarding the charge densities due to polarization. For the used values of permittivity and conductivity of the cells and the medium and for the considered frequency value, the qualitative arrangements of the charge at the particle-medium interfaces are shown in Fig. 5.16.

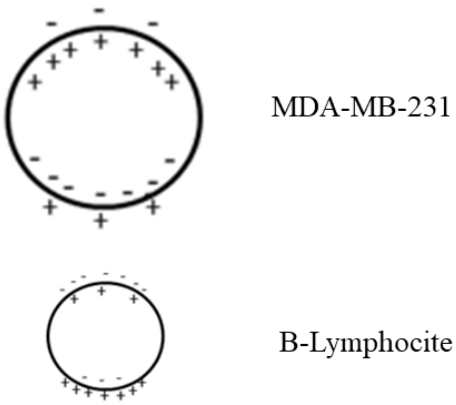

Fig. 5.16 Qualitative electric charge arrangements at the particle-medium interface for the MDA-MD-231 cell and B-Lymphocite. The negative charge densities at the top of the B-Lymphocite and at the bottom of MDA-MD-231 cause the repulsive force between them.

It is important to note that also in this case particle-particle interactions are appreciable thanks to the use of the MST. A calculation of the dielectrophoretic force carried out using the Standard DEP force (Eq. (1.14)) would not have detected this effect and therefore the two MDA-MB-231 higher positioned would have the same "qualitative" behaviour as the others. Standard DEP force utilization could therefore overestimate the capture/separation efficiency of real devices.

5.5 Geometry's effects

Numerical simulations can be used to optimize the microfluidic device geometry and other physical properties, to improve their performance. For example, it can be useful to compare different arrangements of electrode arrays. Two simulations, indicated by (c) and (d), were carried out relating to simulations (a) and (b) respectively, halving the values of the width of electrodes and of the gap between them.

5.5.1 Case (c): MDA-MD-231 cells

The simulation box of the case (c) differs from the (a) one since the following values relative to inter-digitated electrodes are used:

- width of the electrodes: $\mathrm{We} = 20\ \mu m$;
- gap between them: $\mathrm{Wg} = 20\ \mu m$;
- number of electrodes: 24.

Figure 5.17 shows snapshots of the simulation (c) results at the same times as in the Figure 5.9, from t=0 sec to t=5.1 sec. The initial configuration is equal to that of simulation (a).

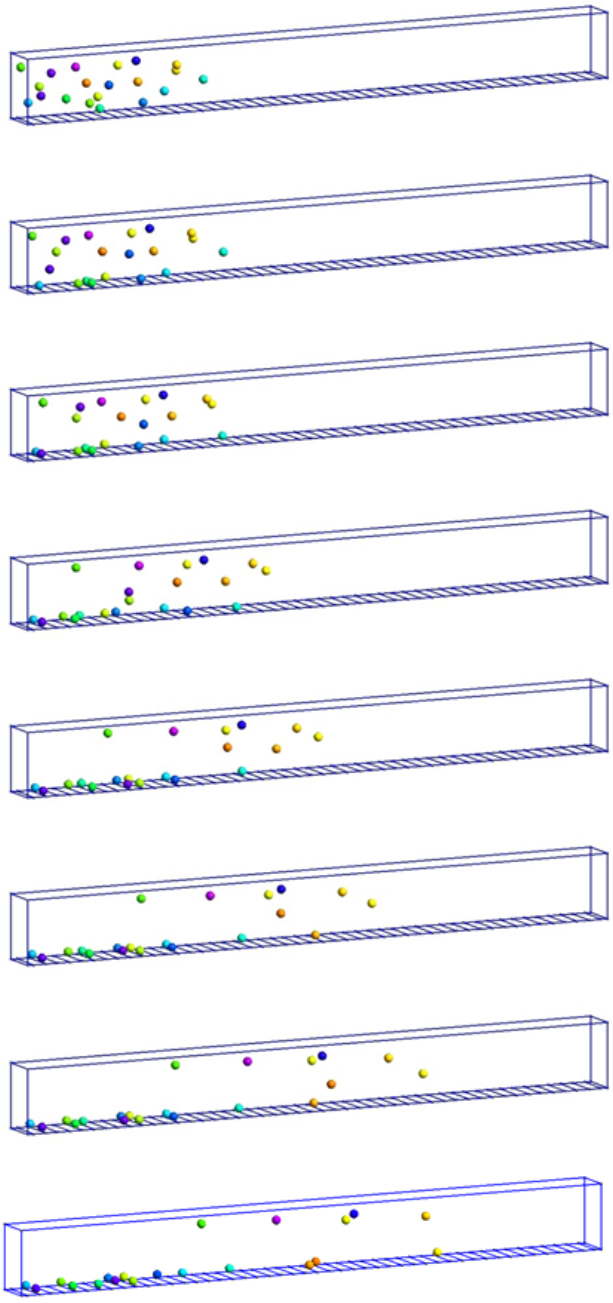

Fig. 5.17 Snapshots for t =0, 0.3, 0.6, 1.5, 2.4, 3.3, 4.2, 5.1 sec (from upper panel to lower panel) of simulation (c). Number of electrodes: 24. The cells are subjected to a p-DEP.

In simulation (c), at the instant 5.1 seconds, 14 of 20 particles are captured, whereas in simulation (a) 16 of 20 particles were captured with the same initial configuration (see Fig. 5.9). This result shows the implications of the choice of electrode-related parameters on capture efficiency. The arrangement of the electrodes in case (c) generates a field with less unevenness and therefore the dielectrophoretic forces are less intense.

5.5.2 Case (d): two-cell systems: MDA-MD-231 and B-Lymphocites

The simulation box of case (d) differs from the (b) one since the following values relative to inter-digitated electrodes are used:

- width of the electrodes: $\mathrm{We} = 20\ \mu m$;
- gap between them: $\mathrm{Wg} = 20\ \mu m$;
- number of electrodes: 20.

Figure 5.18 shows snapshots of the simulation (d) results (from t=0 sec to t=5.1 sec).

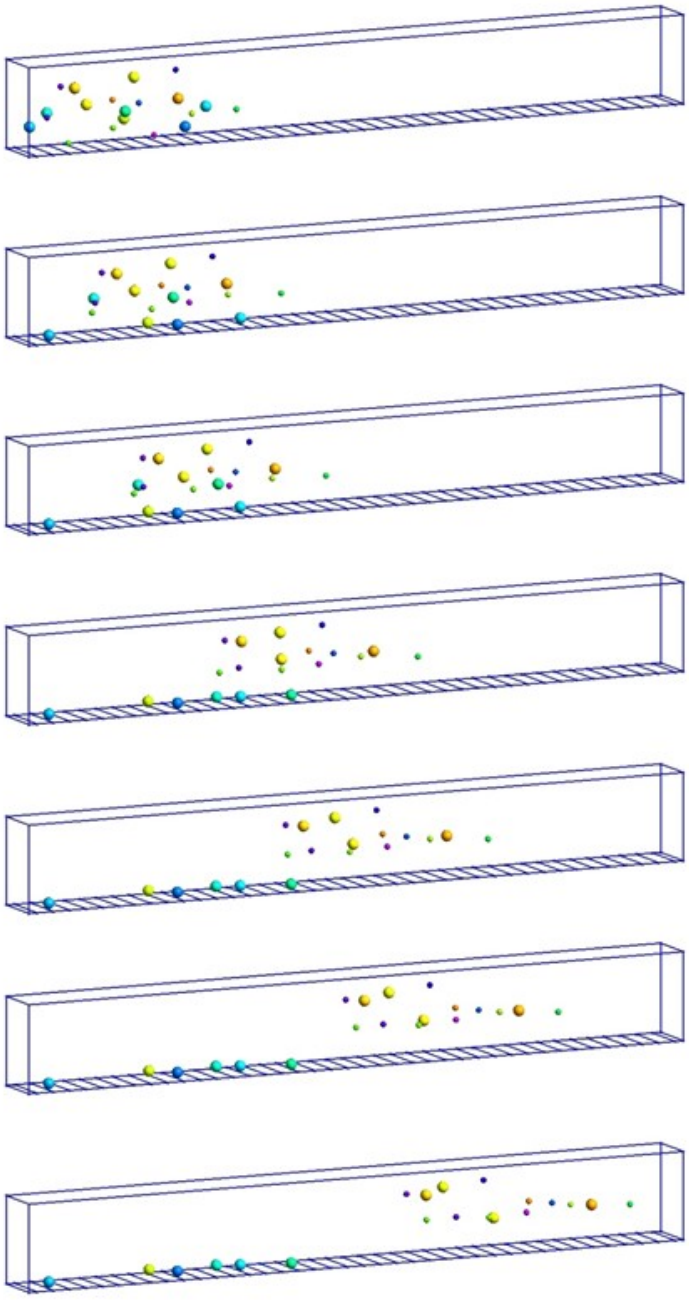

Fig. 5.18 Snapshots for t = 0, 0.6, 1.2, 2.4, 3.3, 4.2, 5.1 sec (from upper to lower) of the simulation (d). The number of electrodes is 20.

From the analysis of the numerical values of the particle altitudes, it can be seen that, for each instant, the MDA-MB-231 cells (which are in p-DEP condition) are higher than the analogous particles of simulation (b) at the same time, while the lymphocytes have lower altitudes compared to their counterparts of case (b). This behaviour is mostly due to the lower intensity, compared to case (b), of the dielectrophoretic forces: the MDA-MD-231 are attracted, and the lymphocytes are rejected, towards the region with higher intensity of electric field, but forces manipulating the cell and driving their movement are less intense. We note that in this case, no inversion of the vertical movement for MDA-MD-231 cells, discussed in the previous section, has been observed.

5.6 Conclusions

In this section we have presented the results of MD-FEM simulations of the kinetics of realistic systems of EMPs which can be experimentally realized. The field-mediated interactions are DEP forces generated by electrodes loaded with AC currents and calculated using the Maxwell Stress Tensor formalism. In particular, two types of colloidal solutions that flow through micro-fluidic channels with different geometries of the electrode set are considered: a solution of MDA-MD-231 tumour cells in p-DEP condition and a mixture of MDA-MB-231 cells and B-Lymphocites in p-DEP and n-DEP conditions, respectively (due to the particular value of the AC frequency chosen). These systems are used for practical applications in the field of cell sorting. In the case of p-DEP only (i.e. a colloidal solution

of the MFA-MB-231 cells only), the results show that the cells experience an attractive force that traps them close to the electrodes' edges. However, the particle-particle interactions strongly affect the trapping efficiency and, in general, the overall system evolution, leading also to the dynamical formation of complexes of cells (chains) moving as a single object after the cells merge due to attractive dipole-dipole interactions. The results of the simulation of the colloidal solution composed of MDA-MB-231 and B-Lymphocites shows that the first cell type experienced p-DEP while the second n-DEP, allowing to study the cell capture/separation capability of the simulated device. Some effects, which can be reproduced only by using non-approximate methods for the calculation of e.mec. forces, are also evidenced.

We focused our study on spherical particles (good approximation of the real cells' systems). For non spherical particles or for particular conditions where couples of forces act on particles with spherical symmetry the method should be extended considering generic rotations, as well as translations, due to the presence of torques. The next chapter presents a prospective discussion of the formalism generalization, based on the use of quaternions, useful for describing the rotational motion of rigid-bodies.

Chapter 6

Generalization of the MD-FEM formalism for particles of generic shape

The method presented in chapters 4 and 5 focuses only on systems consisting of spherical particles and on the pure translational motion of the particles. In this chapter, we discuss the steps needed to generalize the coupled MD-FEM method to the case of particles modelled as rigid body of generic shape. The purpose of the chapter is to demonstrate that this generalization is feasible using a similar numerical context, which considers also the integration of the roto-translational dynamics of the particles.

6.1 Rigid-body dynamics

In the dynamics of the rigid-body, the rotational motion around the center of mass must be considered in addition to the translational motion of the center of mass. The quantities similar to position, velocity, moment, force and mass are, in rotational motion, the orientation $\boldsymbol{\vartheta}$, the angular velocity $\boldsymbol{\omega}$, the angular momentum **L**, the torque **T** and the inertia tensor **I**, respectively.

For the *i-th* (*i*=1…N) rigid-body of a system of *N* bodies, the angular momentum is:

$$\mathbf{L}_i(t) = \mathbf{I}_i(t)\boldsymbol{\omega}_i(t). \tag{6.1}$$

and the equations of rotational motion are:

$$\dot{\mathbf{L}}_i(t) = \mathbf{T}_i(t); \tag{6.2}$$

$$\dot{\boldsymbol{\vartheta}}_i(t) = f[\,\mathbf{I}_i^{-1}(t)\mathbf{L}_i(t)] = f[\boldsymbol{\omega}_i(t)]. \tag{6.3}$$

Let's consider a rigid-body and its fixed reference coordinate system consistent with the body (not inertial) where its geometry is referred. Hereafter, such a system is indicated by the letter *B*. The orientational dynamic variable represents the rotation of the reference system *B* into the world (or laboratory) frame coordinate system *W*. The orientation, which is in general a functional of the angular velocity (Eq. 6.3), can be represented by a set of Euler angles [111, 112] or a rotational matrix [113], but the use of the mathematical entity called "*rotational quaternion*" can be more appropriate and efficient for the MD implementation [114]. The simulations can be carried out by using the integration method called "Rotational Velocity Verlet", which derives from rotational leap-frog method and acts on quaternions [115].

The definition and the main characteristics of the quaternions, the advantages of their use for the study of the rotational motion and their utilization in the Rotational Velocity Verlet will be described in the next sections.

6.2 Quaternions

The rotational quaternion is a formal mathematical entity which consists of a tuple of four real numbers, which can be considered as the sum (in the acceptation of the group theory) of an ordered pair formed by a scalar a and a three-dimensional vector $\mathbf{v}$ [116]:

$$\mathbf{q} = (a, \mathbf{v}) = a + \mathbf{v}. \tag{6.4}$$

The set of quaternions is indicated by $\mathbf{H}$. A quaternion $\mathbf{q} \in \mathbf{H}$ can be written as it follows:

$$\mathbf{q} = a + \boldsymbol{i}x + \boldsymbol{j}y + \boldsymbol{k}z = a + \mathbf{v}, \tag{6.5}$$

where (x, y, z) are the real components of the verctor $\mathbf{v}$.
$\boldsymbol{i}$, $\boldsymbol{j}$ and $\boldsymbol{k}$ have the mathematical characteristics of the imaginary unit of complex numbers. They satisfy the following properties:

- $\boldsymbol{i}^2 = \boldsymbol{j}^2 = \boldsymbol{k}^2 = -1$;
- $\boldsymbol{ij} = -\boldsymbol{ji} = \boldsymbol{k}$;
- $\boldsymbol{jk} = -\boldsymbol{kj} = \boldsymbol{i}$;
- $\boldsymbol{ki} = -\boldsymbol{ik} = \boldsymbol{j}$;
- $\boldsymbol{ijk} = -1$.

The rules of multiplication between $\boldsymbol{i}$, $\boldsymbol{j}$ and $\boldsymbol{k}$ have the same properties as the vectorial product between the unit vectors of a right-handed Cartesian coordinate system.
In analogy with complex numbers, of which an element can be represented by a pair of real numbers, the generic quaternion $\mathbf{q}$ is also representable by means of a four-tuple of real numbers:

$$\mathbf{q} = (a, x, y, z).$$

Ultimately, a quaternion q can be denoted in three different ways: as the sum of a scalar part and a vector part, as a hypercomplex number defined on a basis composed of one real part and three imaginary parts, like a quadruple of reals.
A scalar can be considered as a quaternion with zero vector:

$$a \rightarrow \mathbf{q}(a) = (a, 0,0,0) = (a + \mathbf{0}), \tag{6.6}$$

and a vector can be seen as a quaternion with zero scalar:

$$\mathbf{v} \rightarrow \mathbf{q}(\mathbf{v}) = (0 + \mathbf{v}). \tag{6.7}$$

6.2.1 Algebra of the quaternions

The summation of two quaternions is defined as:

$$\mathbf{q}_1 + \mathbf{q}_2 = (a_1 + \mathbf{v}_1) + (a_2 + \mathbf{v}_2) = (a_1 + a_2) + (\mathbf{v}_1 + \mathbf{v}_2). \quad (6.8)$$

The quaternion (0, 0, 0, 0) = (0, $\mathbf{0}$) is the neutral element of the summation.
The algebraic structure ($\mathbf{H}, +$) is an abelian group.
The dot product of two quaternions is defined as it follows:

$$\mathbf{q}_1 \cdot \mathbf{q}_2 = a_1 a_2 + \mathbf{v}_1 \cdot \mathbf{v}_2. \quad (6.9)$$

The quaternion product is:

$$\mathbf{q}_1\mathbf{q}_2 = (a_1 + \mathbf{v}_1)(a_2 + \mathbf{v}_2) = (a_1 a_2 - \mathbf{v}_1 \cdot \mathbf{v}_2) + (a_1\mathbf{v}_2 + a_2\mathbf{v}_1 + \mathbf{v}_1 \times \mathbf{v}_2); \quad (6.10)$$

The product satisfies the following properties:

- it is associative: $\mathbf{q}_1(\mathbf{q}_2\mathbf{q}_3) = (\mathbf{q}_1\mathbf{q}_2)\mathbf{q}_3$;
- it is not commutative: $\mathbf{q}_1\mathbf{q}_2 \neq \mathbf{q}_2\mathbf{q}_1$;
- it is distributive.

The quaternion (1, 0, 0, 0) = (1, $\mathbf{0}$) is the neutral element of the multiplication.
The product between a scalar $s \in \mathbb{R}$ and a quaternion $\mathbf{q} = a + \mathbf{v}$ is also defined:

$s\mathbf{q} = sa + s\mathbf{v}$.

The conjugation, the inversion and the norm of a quaternion are:

$$\mathbf{q}^* = (a - \mathbf{v}); \tag{6.11}$$

$$\mathbf{q}^{-1} = \frac{\mathbf{q}}{\mathbf{q}\cdot\mathbf{q}^*}; \tag{6.12}$$

$$q = |\mathbf{q}| = \sqrt{\mathbf{q}\cdot\mathbf{q}^*} = \sqrt{a^2 + v^2} = \sqrt{a^2 + x^2 + y^2 + z^2}. \tag{6.13}$$

The algebra of quaternions, with summation and product operations between quaternions, is a skew-field: division is defined in it and the quaternion inverse to a quaternion $\mathbf{q}$ is defined by Eq. (6.12). The skew-field of quaternions is the unique finite-dimensional real associative non-commutative with respect to the product algebra without divisors of zero [117, 118]. The set of quaternions with the operations of summation between quaternions and multiplication by a scalar form a real vectorial space of size four, of which one basis is given by $(1, \boldsymbol{i}, \boldsymbol{j}, \boldsymbol{k})$ [119].

6.2.2 Unit quaternions and rotations

"Unit quaternions" are quaternions with norm equal to 1. Hereafter, all unit quantities will be represented with the symbol hat above the variables. The set of unit quaternions forms a sphere in a 4-dimensional space. The unit quaternions form a multiplicative non abelian group with

respect to the product. By means of Eq. (6.11) and Eq. (6.12) it can be seen that the conjugate and the inverse of a unit quaternion are equal.

A rotation can be conveniently represented by unit quaternions. A quaternion can indeed contain in its four components information about the angle and the axis [120]. Consider a unit vector axis $\hat{\boldsymbol{s}}$, passing through the origin of the right-hand reference system, and an initial vector $\mathbf{v}_0$: a rotation of $\mathbf{v}_0$ by an angle α around the $\hat{\boldsymbol{s}}$ axis, which results in the vector $\mathbf{v}_1$, is performed by means of the following unit quaternion:

$$\hat{\mathbf{q}}_{\alpha,\hat{s}} = \left(cos\frac{\alpha}{2} + sin\frac{\alpha}{2}\hat{\boldsymbol{s}}\right) \tag{6.14}$$

by applying the formula:

$$\mathbf{v}_1 = \hat{\mathbf{q}}_{\alpha,\hat{\boldsymbol{s}}}\mathbf{v}_0\hat{\mathbf{q}}_{\alpha,\hat{\boldsymbol{s}}}^{-1} . \tag{6.15}$$

Each map defined as in Eq. (6.15) is actually a rotation since it preserves the norm. The combination of two consecutive rotations $\hat{\mathbf{q}}_1$ and $\hat{\mathbf{q}}_2$ is obtained by their quaternion product:

$$\hat{\mathbf{q}}_{1,2} = \hat{\mathbf{q}}_1\hat{\mathbf{q}}_2. \tag{6.16}$$

A backward rotation, relative to a previous rotation represented by quaternion $\hat{\mathbf{q}}_1$, is performed by the conjugate or the inverse of $\hat{\mathbf{q}}_1$.

The use of quaternions offers several advantages [121]: for example, four parameters are considered instead of the nine parameters of a rotational matrix [122].

6.3 Rotational Velocity Verlet

A reliable method of studying the temporal evolution in a rotational motion consists in the direct integration of the angular momentum and the quaternion. The equations of motion are (see Ref. [123] for the derivation):

$$\dot{\mathbf{L}}_i^W(t) = \mathbf{T}_i^W(t), \tag{6.17}$$

$$\dot{\mathbf{q}}_i(t) = \frac{1}{2}\hat{\mathbf{q}}_i(t)\,\boldsymbol{\omega}_i^B(t), \tag{6.18}$$

where $\hat{\mathbf{q}}_i(t)$ is the quaternion which describes the body orientation at time t, $\dot{\mathbf{q}}_i(t)$ is its time derivative, $\boldsymbol{\omega}_i^B(t)$ is the body's angular velocity in the body frame.

In the right hand side of the Eq. (6.18), there is a product of the quaternion $\hat{\mathbf{q}}_i(t)$ and the vector $\boldsymbol{\omega}_i^B(t)$: it is a quaternion product of $\hat{\mathbf{q}}_i(t)$ and the quaternion obtained by the angular velocity vector by Eq. (6.7).

It should be noted that in Eq. (6.18) the quaternion time derivative depends on the uknown quaternion itself at the same time *t* and therefore a self-consistent iterative search is necessary.

The initial time of the first half-step is t=0. The orientation quaternion, the angular momentum and the torque (in the world frame *W*) are considered at this time as initial states. The algorithm consists of the following steps.

1) The angular momentum and the torque are converted from the world frame *W* to the body reference *B* by backward rotations:

$$\mathbf{L}_i^B(0) = \widehat{\mathbf{q}}_i^*(0)\mathbf{L}_i^W(0)\widehat{\mathbf{q}}_i(0), \tag{6.19}$$

$$\mathbf{T}_i^B(0) = \widehat{\mathbf{q}}_i^*(0)\mathbf{T}_i^W(0)\widehat{\mathbf{q}}_i(0). \tag{6.20}$$

2) $\mathbf{L}_i^B$ at time $\frac{\Delta t}{2}$ are evaluated by Euler's equation [120] for the *B* frame torque:

$$\boldsymbol{\omega}_i^B(0) = [\mathbf{I}_i^B]^{-1}\mathbf{L}_i^B(0), \tag{6.21}$$

$$\dot{\mathbf{L}}_i^B(0) = \mathbf{T}_i^B(0) - \boldsymbol{\omega}_i^B(0) \times \mathbf{L}_i^B(0), \tag{6.22}$$

$$\mathbf{L}_i^B\left(\frac{\Delta t}{2}\right) = \mathbf{L}_i^B(0) + \frac{\Delta t}{2}\dot{\mathbf{L}}_i^B(0). \tag{6.23}$$

where $\mathbf{I}_i^B$ is the diagonal inertia tensor of the body in the reference frame *B* (it is therefore a diagonal matrix if *B* is suitably chosen).

3) The known quaternion $\widehat{\mathbf{q}}_i(0)$ and the angular velocity at proper time $\frac{\Delta t}{2}$ are used to estimate the zeroth approximate time derivative at time $\frac{\Delta t}{2}$ of quaternion, indicated by ${}^0\dot{\mathbf{q}}_i\left(\frac{\Delta t}{2}\right)$:

$${}^0\dot{\mathbf{q}}_i\left(\frac{\Delta t}{2}\right) = \frac{1}{2}\widehat{\mathbf{q}}_i(0)\,\boldsymbol{\omega}_i^B\left(\frac{\Delta t}{2}\right) = \frac{1}{2}\widehat{\mathbf{q}}_i(0)\left\{[\mathbf{I}_i^B]^{-1}\mathbf{L}_i^B\left(\frac{\Delta t}{2}\right)\right\}. \tag{6.24}$$

4) The zeroth approximate quaternion at time $\frac{\Delta t}{2}$ is calculated by the following approximation:

$$ {}^{0}\hat{\mathbf{q}}_i\left(\frac{\Delta t}{2}\right) = \hat{\mathbf{q}}_i(0) + \frac{\Delta t}{2}\ {}^{0}\dot{\mathbf{q}}_i\left(\frac{\Delta t}{2}\right). \tag{6.25} $$

5) The angular momentum at time $\frac{\Delta t}{2}$ is calculated as follows:

$$ \mathbf{L}_i^W\left(\frac{\Delta t}{2}\right) = \mathbf{L}_i^W(0) + \frac{\Delta t}{2}\mathbf{T}_i^W(0). \tag{6.26} $$

6) An index k is introduced to denote the approximation number and a tolerance ϵ is defined. The following system of constraining equations is solved self-consistently for $\dot{\mathbf{q}}_i\left(\frac{\Delta t}{2}\right)$ until the difference $\left|{}^{(k+1)}\hat{\mathbf{q}}_i\left(\frac{\Delta t}{2}\right) - {}^{k}\hat{\mathbf{q}}_i\left(\frac{\Delta t}{2}\right)\right|$ is less than ϵ:

$$ {}^{(k+1)}\mathbf{L}_i^M\left(\frac{\Delta t}{2}\right) = {}^{k}\hat{\mathbf{q}}_i^*\left(\frac{\Delta t}{2}\right)\mathbf{L}_i^W(0)\ {}^{k}\hat{\mathbf{q}}_i\left(\frac{\Delta t}{2}\right), \tag{6.27a} $$

$$ {}^{(k+1)}\boldsymbol{\omega}_i\ \left(\frac{\Delta t}{2}\right) = [\mathbf{I}_i^M]^{-1}\,{}^{(k+1)}\mathbf{L}_i^M\left(\frac{\Delta t}{2}\right), \tag{6.27b} $$

$$ {}^{(k+1)}\dot{\mathbf{q}}_i\left(\frac{\Delta t}{2}\right) = \frac{1}{2}\ {}^{k}\hat{\mathbf{q}}_i\left(\frac{\Delta t}{2}\right)\,{}^{(k+1)}\boldsymbol{\omega}_i\ , \tag{6.27c} $$

$$ {}^{(k+1)}\hat{\mathbf{q}}_i\left(\frac{\Delta t}{2}\right) = \hat{\mathbf{q}}_i(0) + \frac{\Delta t}{2}\,{}^{(k+1)}\dot{\mathbf{q}}_i\left(\frac{\Delta t}{2}\right). \tag{6.27d} $$

7) The time derivative found in the point 6) is used to calculate the quaternion at time $t = \Delta t$:

$$\hat{\mathbf{q}}_i(\Delta t) = \hat{\mathbf{q}}_i(0) + \Delta t \dot{\mathbf{q}}_i\left(\frac{\Delta t}{2}\right). \tag{6.28}$$

The first half-step is concluded. The new orientation $\hat{\mathbf{q}}_i(\Delta t)$ can be used to calculate the new torque with a force evaluation:

$$\mathbf{T}_i^W(\Delta t) = \mathbf{T}_i^W[\hat{\mathbf{q}}_i(\Delta t)]. \tag{6.29}$$

8) The velocity Verlet integration step is completed by using $\hat{\mathbf{q}}_i(\Delta t)$, $\mathbf{L}_i^W\left(\frac{\Delta t}{2}\right)$ and $\mathbf{T}_i^W(\Delta t)$ to execute the second half-step which consists in the propagation of angular momentum to the time instant $t = \Delta t$:

$$\mathbf{L}_i^W(\Delta t) = \mathbf{L}_i^W\left(\frac{\Delta t}{2}\right) + \frac{\Delta t}{2}\mathbf{T}_i^W(\Delta t). \tag{6.30}$$

At this point the full integration step is complete: $\hat{\mathbf{q}}_i(\Delta t)$, $\mathbf{T}_i^W(\Delta t)$ and $\mathbf{L}_i^W(\Delta t)$ can be used for a new step.

6.4 Control instructions in simulations of rotational motion of non-spherical particles

The control instructions on particle-wall and steric particle-particle interactions used in the case of colloidal solution of spherical particles, described in section 4.3 and Appendix E.5.2, are not applicable to the case

of general non-spherical particles. It is necessary to develop more complex instructions that take into account the shape of the particles in the checks.

6.4.1 Overlap between particles

Steric forces are modelled as an infinite barrier for the overlapping between particles, as a consequence the check must act so that penetration is prevented. For a particle of arbitrary shape and orientation, the minimum distance has to be evaluated as a minimum of the distance for the surface points of the two bodies. Then when this distance is below a certain threshold value a displacement rule must be applied which generalizes the centers' displacement used in the case of spherical particles (see Chap. 4). The FEM representation of the particles in the mesh allows for a numerical approximate evaluation of this minimum distance since the vertices of the mesh cells at the boundary between two domains (i.e. the particle and the medium) can be selected. The distance function implemented in python and integrated in the Gmsh+FEniCS framework is:

```
def distance(ind_fir,ind_sec) # find the (minimum) distance between two volume elements
    points_fir = []
    points_sec = []
    for facet in facets(mesh):  # it sets the face index of given subdomains intefaces (where jump conditions hold)
        sub_domains = []
        for c in cells(facet):
#           sub_domains.append(markers_subdom[c])
            sub_domains.append(mv[c])
        sub_domains = list(set(sub_domains)) # remove duplicates
        len_list=len(sub_domains)
        if len_list > 1: # it is on the interface between two subdomanins
           ind_list=0
           while ind_lisT < len_list-1 :
             if(sub_domans[ind_lis] = ind_fir) :
                xcnt=0.
                ycnt=0.
                zcnt=0.
                for vert in vertices(facet): # triangular facet are assumed to calculated the center
                  xcnt=xcnt+vert.point().x()
                  ycnt=ycnt+vert.point().y()
                  zcnt=zcnt+vert.point().z()
                xcnt=xcnt/3.0
                ycnt=ycnt/3.0
                zcnt=zcnt/3.0
                point=[xcnt,ycnt,zcnt]
                points_fir.append(point)
             if(sub_domans[ind_lis] = ind_sec) :
                xcnt=0.
                ycnt=0.
                zcnt=0.
                for vert in vertices(facet): # triangular facet are assumed to calculated the center
                  xcnt=xcnt+vert.point().x()
                  ycnt=ycnt+vert.point().y()
                  zcnt=zcnt+vert.point().z()
                xcnt=xcnt/3.0
                ycnt=ycnt/3.0
                zcnt=zcnt/3.0
                point=[xcnt,ycnt,zcnt]
                points_sec.appent(point)
             ind_list +=1
    len_fir=len(points_fir)
    len_sec=len(points_sec)
    ind_fir=0
    ind_sec=0
    distance = 1.e20
    while ind_fir < len_fir-1 :
      while ind_sec < len_sec-1 :
        discur=pow(points_fir[0][ind_fir]-points_sec[0][ind_sec],2)+pow(points_fir[1][ind_fir]-points_sec[1][ind_sec],2)+pow(points_fir[2][ind_fir]-points_sec[2][ind_sec],2)
        if discur < distance : distance = discur
        ind_sec+=1
      ind_fir+=1
    distance=pow(distance,0.5)
    return distance
```

This function also extracts the two eventual “contact” points at the two surfaces (more properly the two points which will be in contact if the distance further decreases). We note the distance evaluation needs a double loop over the surface points, which for meshes with good resolution could be about 1000. The approximatelly 1000000 operations may not be efficient if distances are evaluated for all the N particles in the system. Moreover, the check could be redundant for definitively distant particles. An optimization is also considered introducing a pre-check of “distant” particles. The first step is to build a sphere around each particle, whose diameter is the pre-evaluated maximum distance between surface points of the particles (fixed for identical particles). Considering these spheres, the same control check seen in the previous chapters is performed. In the case of overlapping between spheres, the second check acts by calculating the numerical distance with the Python function reported above.

For the displacement rule in the case of convex non-spherical particles, both the positions and the orientation can be properly changed. In this case, the displacement is a composition of a translation of the center of mass along the normal at the surface in the contact point and a rotation around the axis given by the vector product between this normal and the vector joining the centre of mass and the contact points. For non convex particles, the rotation must be considered with caution since they could generate further overlap in other points of the surface. In this case, the single translation is more efficient although it is a rough approximation of the real steric interactions.

Conclusions

In this Thesis, we proposed a coupled Molecular Dynamics – Finite Element Method technique as a tool for the study of the kinetics of systems where many body particle-particle interactions are mediated by continuum fields that evolve self-consistently with the system configuration. The presence of field-mediated forces cannot be exclusive: indeed, in the systems we have specifically analyzed, the particles are also subjected to forces which can be rightly described using the particle-like formulation of the usual Monte Carlo [14] or MD approach. In this work we have also considered, in addition to the field mediated forces, both single-particle interactions (drag, lift, gravity) and two-particle interactions (steric interactions). In the MD-FEM implementation of this research work, consolidated open source solvers (Gmsh and FEniCS), applying the Finite Element Method technique for the Partial Differential Equations numerical solutions, are integrated in the MD algorithm for the explicit integration of the particle equations of motion [i] [18].

As an explicit application of the method, we have carried out simulations of the kinetics of cells (MDA-MB-231 tumor cells, B-Lymphocites and mixtures of them) in a colloidal solution that flows through a micro-fluidic channel in the presence of a non-uniform electric field [ii], [iii] [5, 6]. In this case, the MD method finds application away from

[i] Michele Cascio, Davide Baroli, Stephane Bordas, Ioannis Deretzis, Giuseppe Falci, Antonino Magliano and Antonino La Magna, submitted to Physical Review E.

[ii] A. Magliano, M. Camarda, S. F. Lombardo, R. Di Martino, M. Cascio, A. Romano, L. Minafra, G. Russo, M. C. Gilardi, F. Di Raimondo, S. Scalese and A. La Magna, Sensing and Bio-Sensing Research **8**, 59-64 (2016).

the atomistic simulation area, which is the one where the MD is typically applied. The field-mediated interactions are dielectrophoretic forces generated by electrodes loaded with AC currents and calculated using the Maxwell Stress Tensor formalism. Using conventional concepts of p-DEP/n-DEP (DEP attraction/repulsion of cells towards the electrodes) we demonstrated that quantitative estimates and qualitative phenomenology of the system evolution can be correctly addressed only with our accurate methodology. In the case of p-DEP only (i.e. a colloidal solution of the MFA-MB-231 cells only), the cells experience an attractive force that traps them close to the electrodes' edges. However, the particle-particle interactions strongly affect the trapping efficiency and, in general, the overall system evolution, leading also to the formation of complexes of cells (chains) moving as single objects after the cells merge due to attractive dipole-dipole interactions.

A simulation of a colloidal solution composed of MDA-MB-231 and B-Lymphocites was also presented. Due to the particular value of AC frequency chosen, the first cell type experienced p-DEP while the second n-DEP, allowing to study the cell capture/separation capability of the simulated device. In the discussion of this particular simulation, we evidenced some effects which can be reproduced only by using non-approximate methods for the calculation of e.m. forces, such as repulsion between different types of particles, stressing the importance of applying

---

[iii] R. Di Martino, M. Camarda, M. Cascio, Michele G., A. Magliano, S. Baldo, A. Romano, L.Minafra, G. I. Forte, G. Russo, M. Gilardi, F. Di Raimondo, S. Scalese and A. La Magna, Sensing and Bio-Sensing Research **7**, 162-167 (2016).

such a method to accurately estimate the capture/separation efficiency of a real device.

The two simulations described have been repeated by changing the size of the electrodes and the gap between them, to demonstrate the ability of simulations to optimize the electrode geometry in a design study aiming at the improvement of the device efficiency.

An extension of our method in the DEP field could be implemented using a similar framework in order to generalize the particle shape, as the spherical approximation could be too stringent to simulate inner motion of e.mec. particles due to torques. To this end, the appropriate formalism, based on the use of quaternions, was presented in the last chapter to describe the rotational motion of rigid-bodies. Moreover, the method can be easily adapted for the numerical evaluation of the medium kinetics, solving self consistently a Navier-Stokes type equation.

In general, we note that a similar continuum/particle approach can be also formulated and implemented to other problems where the conventional force evaluation method used in MD is not applicable or its application is not computationally efficient (e.g. evolution of clusters of bonded particles, interaction between extended defects mediated by the strain field, mesoscopic systems, multiscale simulations etc.).

Appendix A

Electric potential due to a finite dipole.

This appendix shows the calculation of the electric potential generated by a finite dipole [23]. Consider the electrical potential Φ due to a finite dipole immersed in a linear dielectric medium of permittivity ε_m and aligned along the z axis of a Cartesian reference system; the positive charge has z coordinate equal to $d/2$, the negative equal to $-d/2$. Let r_+ and r_- the distances between the point considered and the positive and negative charge respectively. Figure A.1 shows this system.

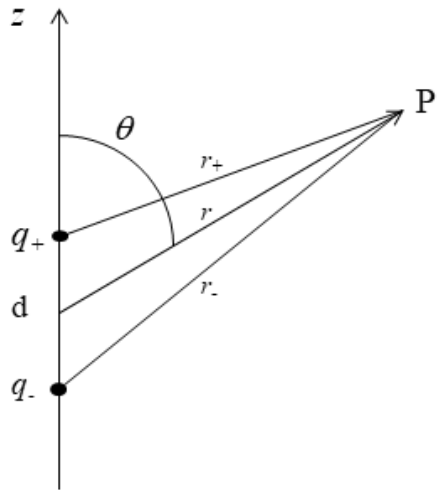

Fig. A.1 Small physical dipole aligned with z axis showing r_+ and r_- defined at an arbitrary point (r, ϑ).

Consider the point with coordinates (r, ϑ), radial and polar respectively. The charge distribution is axisymmetric with respect to point P,

so that $\Phi \equiv \Phi(r, \vartheta)$. Because of the superposition principle, the potential has the following form:

$$\Phi(r, \vartheta) = \frac{q}{4\pi\varepsilon_m r_+} - \frac{q}{4\pi\varepsilon_m r_-}. \quad \text{(A.1)}$$

It is possible to show that the r_+ and r_- are related to d and to couple (r, ϑ) by the following relations:

$$\frac{r}{r_+} = \left[1 + \left(\frac{d}{2r}\right)^2 - \frac{d}{r}cos\vartheta\right]^{-\frac{1}{2}},$$

$$\frac{r}{r_-} = \left[1 + \left(\frac{d}{2r}\right)^2 + \frac{d}{r}cos\vartheta\right]^{-\frac{1}{2}}.$$

By using the McLaurin series:

$$(1+x)^{-\frac{1}{2}} = 1 - \frac{x}{2} + \frac{3}{8}x^2 - \frac{5}{16}x^3 \ldots$$

it is possible to derive the following expressions:

$$\frac{r}{r_+} = P_0 + \frac{d}{2r}P_1 + \left(\frac{d}{2r}\right)^2 P_2 + \left(\frac{d}{2r}\right)^3 P_3 + \ldots \quad \text{(A.2)}$$

$$\frac{r}{r_-} = P_0 - \frac{d}{2r}P_1 + \left(\frac{d}{2r}\right)^2 P_2 - \left(\frac{d}{2r}\right)^3 P_3 + \ldots \quad \text{(A.3)}$$

where P_1, P_2, P_3… are the Legendre polynomials, where the first terms are as follows:

$P_1 = cos\vartheta,\ P_2 = \frac{3cos^2\vartheta - 1}{2}, P_3 = \frac{5cos^3\vartheta - 3cos\vartheta}{2}.$

By Eq. (A.1), (A.2) and (A.3), the expression for the electrostatic potential assumes this form:

$$\Phi(r,\vartheta) = \frac{qdP_1}{4\pi\varepsilon_m r^2} + \frac{qd^3P_3}{16\pi\varepsilon_m r^4} + \cdots \qquad \text{(A.4)}$$

The quantity $\frac{qdP_1}{4\pi\varepsilon_m r^2}$ is the dipole term; the second term refers to n=3 (where n is the subscript of the polynomial of Legendre), this is an octupolar correction; all addition high-order terms are of odd order (n=5,7…). Stopping the expansion at the first order and considering the expression for the first Legendre polynomial, the potential assumes the following form:

$$\Phi(r,\vartheta) = \frac{qdcos\vartheta}{4\pi\varepsilon_m r^2}\,. \qquad \text{(A.5)}$$

Appendix B

Effective dipole moment of a dielectric particle.

The effective dipole moment of a particle suspended in a dielectric medium, indicated with p_{eff}, is defined as the moment of an equivalent, free-charge point dipole that causes the same dipolar electrostatic potential if it is immersed in the same dielectric medium and occupies the same position as the center of the particle. The expression for the electric potential generated by a polarized dielectric particle will contain the effective moment p_{eff}. To determine p_{eff}, one needs to solve the relative boundary problem and to compare the result relative to the term of the electrostatic potential solution to the equation [23]:

$$\Phi(r,\vartheta) = \frac{p_{eff}cos\vartheta}{4\pi\varepsilon_m r^2}. \qquad \text{(B.1)}$$

Let's consider an isolated homogeneous dielectric sphere of radius *R*, permittivity ε_p and conductivity σ_p, immersed in a dielectric fluid medium of permittivity ε_m and conductivity σ_m, subjected to a uniform *z*-directed electric field of magnitude E_0.

Here, the electric potential outside the sphere is called $\Phi_1(r,\vartheta)$ while the one inside the sphere is called $\Phi_2(r,\vartheta)$. The electrostatic potential satisfies Laplace's equation everywhere. $\Phi_1(r,\vartheta)$ will be composed by two terms, the first due to the imposed electric field and the second one due to the induced dipole relative to the particle. $\Phi_2(r,\vartheta)$ will be composed only by

the first type of term. We assume that the solutions for $\Phi_1(r,\vartheta)$ and $\Phi_2(r,\vartheta)$ take the form:

$$\Phi_1(r,\vartheta) = -\mathrm{E}_0\, r\, cos\vartheta + \frac{\tilde{a}\, cos\vartheta}{r^2}, \qquad r > R \tag{B.2}$$

$$\Phi_2(r,\vartheta) = -\tilde{b}\, r\, cos\vartheta, \qquad r < R \tag{B.3}$$

The boundary conditions allow to determine the unknown complex coefficients $\tilde{a}$ and $\tilde{b}$. They are applied on the surface of the particle, this is for $r = R$. In this case there are two type of BC: the first refers to the continuity of the electric potential across the particle-fluid boundary:

$$\Phi_1(r = R,\vartheta) = \Phi_2(r = R,\vartheta); \tag{B.4}$$

the second one refers to a charge continuity conditions because of the finite conductivity results in the time dependent accumulation of free electrical charge on the particle surface $(r = R)$. The instantaneous charge conservation condition is:

$$\sigma_m \frac{\partial \Phi_1}{\partial r} - \sigma_p \frac{\partial \Phi_2}{\partial r} + \frac{\partial}{\partial t}\left[\varepsilon_m \frac{\partial \Phi_1}{\partial r} - \varepsilon_p \frac{\partial \Phi_2}{\partial r}\right] = 0, \tag{B.5}$$

where $\sigma_m \frac{\partial \Phi_1}{\partial r}$ and $\sigma_p \frac{\partial \Phi_2}{\partial r}$ are respectively the normal components of the ohmic current outside and inside the dielectric sphere, and $\varepsilon_m \frac{\partial \Phi_1}{\partial r} - \varepsilon_p \frac{\partial \Phi_2}{\partial r}$ is the free unpaired electric charge on the particle suface. It is assumed that

all variable have an exponential dependence, the time derivative results then to a factor $i\omega$ and the Eq. (B.5) becomes:

$$\sigma_m \frac{\partial \Phi_1}{\partial r} + i\omega\varepsilon_m \frac{\partial \Phi_1}{\partial r} = \sigma_p \frac{\partial \Phi_2}{\partial r} + i\omega \frac{\partial \Phi_2}{\partial r}. \quad \text{(B.6)}$$

From the previous equation the following boundary condition on the normal electric field component can be derived:

$$\tilde{\varepsilon}_m \frac{\partial \Phi_1}{\partial r} = \tilde{\varepsilon}_p \frac{\partial \Phi_2}{\partial r}, \quad \text{(B.7)}$$

where the complex dielectric constants appear defined as follows:

$$\tilde{\varepsilon}_m = \varepsilon_m - i\frac{\sigma_m}{\omega}, \quad \text{(B.8)}$$

$$\tilde{\varepsilon}_p = \varepsilon_p - i\frac{\sigma_p}{\omega}. \quad \text{(B.9)}$$

Combining Eq. (B.2), (B.3), (B.4) and (B.7), $\tilde{a}$ and $\tilde{b}$ assume the following form:

$$\tilde{a} = \frac{\tilde{\varepsilon}_p - \tilde{\varepsilon}_m}{\tilde{\varepsilon}_p + 2\tilde{\varepsilon}_m} R^3 E_0, \quad \text{(B.10)}$$

$$\tilde{b} = \frac{3\tilde{\varepsilon}_m}{\tilde{\varepsilon}_p + 2\tilde{\varepsilon}_m} E_0. \quad \text{(B.11)}$$

By replacing Eq. (B.10) in Eq. (B.2) and comparing with Eq. (B.1):

$$p_{eff} = 4\pi\varepsilon_m\tilde{a} = 4\pi\varepsilon_m f_{CM} R^3 E_0 \quad \text{(B.12)}$$

where the so-called Clausius-Mossotti factor f_{CM} is introducted:

$$f_{CM} = \frac{\tilde{\varepsilon}_p - \tilde{\varepsilon}_m}{\tilde{\varepsilon}_p + 2\tilde{\varepsilon}_m}. \quad \text{(B.13)}$$

Appendix C

Circulating tumor cells and microfluidic technology

C.1 Circulating tumor cells

In recent years it has been shown that the peripheral blood of individuals with solid tumours (such as breast, colorectal, prostatic, ovarian, lung cancer, etc.) contains the so-called circulating tumour cells (CTCs), namely tumor cells that enter the bloodstream, shed from the primary tumor, spontaneously circulating in the peripheral blood or spreading into blood vessels [124, 125] .

The presence of a high number of CTCs in the peripheral blood of patients with epithelial neoplasms (carcinomas) may be related to an unfavourable prognosis, while a reduction in their number is related to a good therapeutic response [126]. Numerous studies also show that there is a close correlation between the amount of CTCs and positivity at radio-diagnostic examinations during therapy's follow-up. The detection of the presence of CTCs therefore allows for an assessment of the prognosis of the tumour and consequently a more focused and effective management of the patient.

C.1.1 Metastasis

The metastatic cascade is not a very clear process, but it was however understood that this is a process related to cell migration and intravasation into the circulation [127, 128]: the cells consequently could spread to distant organs where they may reside and ultimately begin to form metastasis [129]. Solid neoplasms, disseminating CTCs in peripheral blood, can then cause metastases even after complete resection of the neoplasm. Clinical studies have demonstrated a significant correlation between the presence of CTCs and the onset of metastases [130]. Early detection of CTCs, if possible, could bring forward the onset of metastases by several months. In addition, several clinical and molecular studies on disease course and growth rates, as well as genetic analyses of both primary and CTCs cancer, are changing the "serial" evolutionary model describing neoplasia and metastases in favour of a parallel progression model [131], which allows explaining why, for example, 5-10% of patients present with metastases without any signs of primary cancer. This model suggests that cancer cells spread earlier than previously thought and that the metastatic diffusion capacity may be the direct effect of circulating cells. This may indicate that the lymphatic and circulatory system, and not the primary tumour, may be the environment in which tumour cells evolve to more aggressive and proliferating stages.

The parallel progression of diffusion is due to the so-called "tumour dormancy", a phase of tumour progression in which the disease is present in minimal residual disease (MRD) forms, and remains asymptomatic even for long periods.

This underlines the need of a deeper understanding of the role of the CTCs. Several studies are aimed at the characterization of the molecular profile and the identification of genetic-molecular factors able to describe the physiology of CTCs [132]. The genotypic and phenotypic analysis of these cells aims to correlate their molecular characteristics with those of the primary tumour: this last aspect allows to verify whether the alterations of the primary tumour are the same or different from those found in CTCs.

Much effort is also currently devoted to the research of correlations between the phenotypic and biomolecular aspects of CTCs and the response to different therapeutic protocols administered to patients according to the clinical stage of the disease, in order to highlight some subclasses of patients who can benefit from specific treatments depending not only on the characteristics of the primary tumour but also on CTCs. If the results of these studies were to reveal the discriminating value in prognostic and predictive terms of CTCs, research and characterisation of these cells could prove to be a powerful tool for identifying individuals at risk for metastases at a very early stage.

It is worth noting that CTCs analysis has identified patients with sub-millimetric tumours that cannot be identified by current imaging techniques (CTCs generated by dormant tumours) [133]. The synergistic use of cell analysis and imaging would allow for better prognostic capability.

Effective and sensitive instruments capable of anticipating the onset of metastases, particularly in the case of solid tumours, are not yet available in the field of clinical laboratory diagnostics. The use of so-called “tumour markers” is a therapy monitoring tool that is often ineffective because some tumours may not express such markers. It therefore is important that modern

biotechnology aims to build new CTCs capture systems, in order to simplify and standardise the test for CTCs in peripheral blood. Patients suffering from solid neoplasms could find in this type of evaluation a very useful tool for customizing the therapy.

C.1.2 CTCs analysis as a “liquid biopsy”

Diagnosis and monitoring of cancer cells can be currently performed by using different standard methods. Among them, the biopsy is one of the most valid techniques for measuring the presence and the extent of tumors. However, since the biopsy procedure is quite invasive, the tests cannot be repeated several times on the same patient. Other diagnostic methods, such as those related to CTCs, can result in a much less invasive examination, thanks to the fact that it is performed on peripheral blood samples. CTCs analysis can be seen as a form of “liquid biopsy”. CTCs detection relies, in fact, on venipuncture (only 5–10 mL of patient blood), rather than solid tissue biopsy or bone marrow aspiration and it can be performed repeatedly with low risk of side effects [134, 135]. The low volume requirement is advantageous in general but could become decisive for some applications such as pediatric clinical care.

CTCs analysis can effectively monitor the progression of the tumors, enabling a dynamic measurement of cancer and giving an indication on the response to therapy [136, 137, 138] and, as well, on the possible treatments to be applied [139, 140]. The number of CTCs in the patient blood can represent, in fact, a promising and valid indicator in terms of their survival

rates, the outcomes of the applied medical treatments, the monitoring of its progression and for the choice of the correct therapeutic intervention [141]. The interest of the scientific community in the recognition and analysis field of tumoral cells has grown in the last years, achieving important results. For instance, it had observed that the presence of tumoral cells in peripheral blood of patients was related to their clinical progress, and the cancer cells were found in venous blood draining the tumor as well as in peripheral blood [142]. Furthermore, CTCs can provide predictive and prognostic information, in terms of disease relapse, overall survival, and tumor response to therapy in patients with metastatic colorectal [143, 144], breast [145, 146], prostate [147, 148], lung and ovarian cancers [149].

As demonstrated by the literature in the field [150, 151, 152], isolation and detection of the tumoral cells represent a stimulating technological challenge, especially in the cases of procedure based on the biological characterization.

The problem in the use of CTCs for diagnostic and prognostic purposes is linked to the standardisation of CTCs research methodologies, which are very heterogeneous and constantly evolving due to the difficulties encountered in isolating them in peripheral blood, i.e. separating them from healthy cells. The difficulty in separating the CTCs in the bloodstream arises from their low concentration (a few to hundreds per mL of whole blood) among the background population of other hematopoietic components (erythrocytes: ~109 per mL of whole blood, leukocytes: ~106 per mL of whole blood) [153, 154, 155]. CTCs are a small fraction of the circulating mononuclear cells. In patients with advanced solid cancers, concentration of CTCs often is very low, on the order of about 1 per ten

million withe blood cells (WBCs) in a 7.5 mL sample of blood [156, 157, 158]. The extremely low concentration of CTCs poses a challenge for their detection and characterization. In recent years, several methods have been developed for the isolation and detection of CTCs.

The techniques currently used to detect the presence of CTC in blood use marker antibodies (magnetic or fluorescent) to perform separation. It is very difficult accurately identify cells as CTCs using only epithelial biomarkers. These techniques are expensive, slow, used in research and not intended for systematic clinical use. In addition, no markers are known for about 15% of solid tumours, most soft tumours, and all lymphomas [159].

Recently, a possible solution is represented by the use of microfluidics-based technology. Such alternative approach for capturing cancer cells from complex cellular fluids can offer an accessible source for detection, characterization, and monitoring of tumors with high efficiency, sensitivity, and throughput.

C.1.3 CTCs in breast cancer patients. MDA-MB – 231 cell line

Solid breast neoplasms are the most common cause of death for women in developed countries. In recent years, early diagnosis, development of surgery and adjuvant therapy have improved the prognosis of these diseases, but relapses are frequent, with fatal results in the case of metastatic disease. There are statistical studies on the frequency of relapses, whose predictive capacity is ineffective. No other instrument is able to monitor the effect of adjuvant therapy in this type of carcinoma.

Solid neoplasms can disseminate CTCs in peripheral blood and can cause metastases even after complete resection of the neoplasm. The identification of CTCs in patients with localized or metastatic breast neoplasia is the subject of numerous studies in the literature. Studies have shown that the presence of cancer cells can be related to the pre-malignant stages of breast cancer, suggesting early spread to distant organs [160].
Clinical studies have demonstrated a significant correlation between the presence of CTCs and the onset of metastases [161] and have shown that in metastatic breast cancer a high number of CTCs in the blood is related to a worse prognosis [162, 163].

The MDA-MB-231 cell line is an epithelial, human, highly invasive breast cancer cell line. It is one of the most commonly used breast cancer cell lines in medical research laboratories. Understanding the molecular basis of breast cancer is crucial for effective new drug development, and many studies on potentially active agents for this particular type of cancer have been conducted using the MDA -231 cell line, which is well established as a tool for bone metastasis research [164]. In this Thesis, simulations carried out on systems with MDA-MB-231 cell line are presented.

C.1.4 Techniques of CTCs isolation

The importance of CTCs as functional biomarkers of solid cancers is evidenced by the several techniques, strategies and methods that have been developed for their detection and isolation.

The microfluidic devices have applied for CTCs detection [165]. They are designed typically based on the morphological and electrical differences of the CTC properties. Microfluidics-based technologies show an ability to capture a significant percentage of rare cells enabling efficient processing of complex cellular fluids, with minimal damage to cell populations and minimal blood volume. The advantages of microfluidics include its capacity for automatic programming, flexibility in performing a large number of samples [166, 167]. However, currently available technologies still suffer from low purity of the captured cells [168].

The methods rely on differing properties and characteristics of CTCs within the blood [169]. Current CTCs isolation technologies could be classified relating on biological or physical properties of the cells, or on the combination of both. They can be grouped into three main categories [170]:

- **physical properties**: make it possible distinguish CTCs from normal WBCs; permit CTCs isolation without biomarker labelling;

- **biological markers**: make it possible distinguish CTCs from normal WBCs and can be used to identify cells selected by other methods;

- **functional properties**: can be used for downstream characterization of isolated CTCs.

The interest of this Thesis is on physical properties. CTCs generally have several physical characteristics that differ from those of nucleated blood cells, including size, density, deformability or electric behaviour. The

methods of isolation based on physical properties are related to centrifugation, membrane- or filtration-based systems, and DEP. A brief description of isolation methods based on physical properties is given below.

Size exclusion:

epithelial-derived cancer cells are larger than the majority of other normal constituent blood cells. Filters can therefore be used to remove the majority of peripheral blood cells and so to separate CTCs from whole blood [171, 172, 173]. Filters generally consist on parylene membrane layers. The advantage of this technology is in its label-free isolation of CTCs, while the greatest limitation is its sensitivity to size [174, 175].

Deformability:

Metastatic cells are often more deformable than normal blood cells [176, 177, 178]. The data of several studies [179] suggest that differential deformability could be used to separate cancer cells from WBCs.

Density:

Density differences are on the basis of gradient centrifugation to isolate CTCs from other hematopoietic components. The mononuclear cells and CTCs have a density <1.077 g/mL, while the granulocytes and the other blood cells and have a density greater than such value [180]. The gradient

centrifugation generates a layered separation of different cell types based on their cellular density. This method offers a quick and simple way to isolate CTCs, but has a poor sensitivity because of the loss of some CTCs migrating to the plasma layer or the formation of CTCs aggregates.

Electric properties:

By using DEP, the manipulation of cells depends only on dielectric properties of any individual phenotype. DEP separation techniques can reach a single-cell-level purification. They combine synergistically a microsystem that integrates a microelectronic chip with a microfluidics chamber in an automatic platform to select and isolate individual cells with high accuracy and precision [181].

C.2 Microfluidics Technology

Microfluidics is a multidisciplinary field that studies the behaviours of fluids in the microscale. It is defined as the science and technology of systems that process or manipulate small amounts of fluids (10^{-9}-10^{-18} litres), using channels with dimensions of tens to hundreds of micrometers. It is commonly referred to "Micro Total Analysis Systems" (μTAS), that deals with miniaturized devices integrated with all necessary components for the analysis of a sample. Developed since the 1990s from the field of miniaturization and microelectronics [182, 183], μTAS offers the possibility to create a complete analytical microsystem by integrating different

functional components to a single device [184, 185]. Devices typically contain several components: microsensors, micropumps, microvalves. Microfluidic systems have been improved as tools for high-throughput discovery and screening studies in chemistry and materials science [186, 187].

Microfluidic devices, often referred to as microfluidic chips, are fabricated using techniques developed in the semiconductor industry. The first applications of microfluidic technologies have been in chemical analysis, thanks to its several capabilities and abilities [188]:

- to use very small quantities of samples and reagents,
- low cost;
- short time for the analysis;

The microfluidic chips have a typical size of the order of a square centimetre. They are often made of silicon, glass, or polymers. Polydimethylsiloxane (PDMS) is widely used in microfluidic device fabrication using soft lithography techniques [189].

"Lab-on-a-chip" (LOC) devices are microfluidic platforms that can handle complex chemical and biological management and analysis for many practical applications in the fields of life sciences, pharmaceutical research, etc.. These devices integrate on a single chip multiple functions that can be performed in the laboratory. They commonly range from a few millimeters to a few square centimeters in size and are capable of handling extremely small volumes of fluids, under the picolitres.

Along with chemistry, life science is the main field of use of this technology [190], that is promising for biomolecular separations thanks to his ability to manipulate fluids on the cellular length scale. LOC systems allows the manipulation of particles in several diagnostic and clinical applications, such as trapping, sorting, separation, characterization of cells, viruses, proteins, nano- and microparticles [191]. Various techniques have been developed to manipulate particles in microsystems. Among other, the one based on DEP is the most important methods in LOC devices. Recently microfluidic devices have indeed been widely recognized as a powerful technology that will play an important role in future medical analysis as diagnostic tools, and represent a promising approach to isolate cancer cells by processing complex cellular fluids with great simplicity, sensitivity, and throughput [192, 193, 194]. Microfluidic DEP based devices have many advantages over conventional systems to capture tumour cells [195, 196, 197]:

- label-free nature;
- reduced size of operating systems;
- flexibility in design;
- less reagent consumption;
- reduced production of wastes;
- increased speed of analyses;
- favorable scaling effects;
- manageability and simplicity of the instrumentation;
- portability.

These features result in high capture efficiency and cell purity [198, 199]. Figure 5.6, which is presented again below, shows a schematic representation of the microfluidic channel with the geometry used in the simulations.

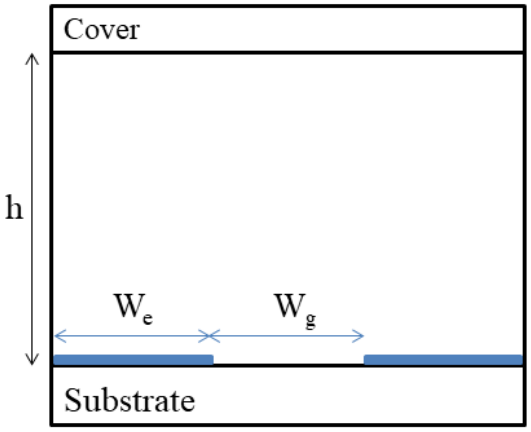

Fig. 5.6 Schematic of the computational domain (limited for simplicity to only two electrodes whilst in the simulation N electrodes are considered). The electrodes (in blue) have a width W_e and are separated by a gap of width W_g.

The following are the materials and measures typically adopted for the prototypes of dielectrophoretic devices with inter-digitated circuit (the Fig. 5.6 is not drawn to scale) [200]:

- the glass in widely used as a substrate, with a thickness of about 500 μm;
- the material used for the cover is typically PDMS, with a thickness of about 1 mm [201];
- the height h of the microchannel is about 100 μm;

- the width of the electrodes and gaps between them are in the range 20-50 μm;
- the thickness of the electrodes is about 100 nm.

Appendix D

Particle model

In the realistic model for cells adopted in this work, the cell is represented by a spherical dielectric core and a spherical dielectric shell to account specifically for the dielectric properties (conductivity and permittivity) of the cytoplasm and of plasma-membrane respectively. Figure D.1 represent this concentric, dielectric shelled model. The permittivity and the conductivity of the liquid medium are ε_m and σ_m and hit complex permittivity therefore is:

$$\tilde{\varepsilon}_m = \varepsilon_m - i\sigma_m/\omega.$$

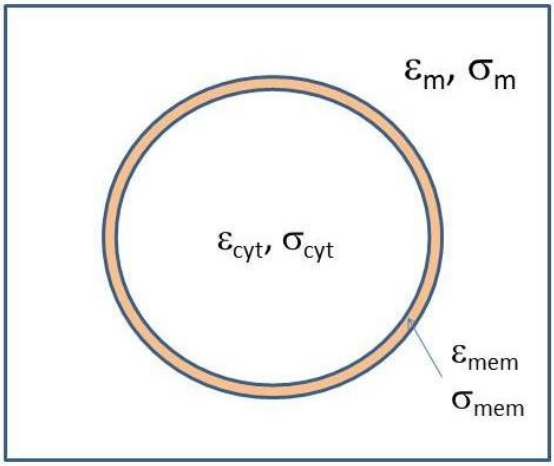

Fig. D.1 Spherical dielectric cell composed of cytoplasm (inner volume) and membrane (light brown shell).

It is possible to find one "effective electrical permittivity" $\tilde{\varepsilon}_{eff}$ taking into account the properties of the two different parts of the cell, cytoplasm and membrane [1, 202].
Consider the electric potential in three regions: Φ_1 in the liquid medium, Φ_2 in the cell membrane, Φ_3 in the cytoplasm. The forms of the potentials are:

$$\Phi_1(r,\vartheta) = -\mathrm{E}_0\, r\, cos\vartheta + \frac{\tilde{a}\, cos\vartheta}{r^2} \qquad r > R,$$

$$\Phi_2(r,\vartheta) = -\tilde{b} r\, cos\vartheta + \frac{\tilde{c}\, cos\vartheta}{r^2} \qquad R - d < r < R,$$

$$\Phi_3(r,\vartheta) = -\tilde{d}\, r\, cos\vartheta \qquad r < R - d.$$

The boundary conditions at the two dielectric interfaces are:

$$\begin{cases} \Phi_1(r = R,\vartheta) = \Phi_2(r = R,\vartheta) \\ \tilde{\varepsilon}_m \frac{\partial \Phi_1}{\partial r} = \tilde{\varepsilon}_{mem} \frac{\partial \Phi_2}{\partial r} \end{cases} \qquad \text{at} \quad r = R;$$

$$\begin{cases} \Phi_2(r = R - d,\vartheta) = \Phi_3(r = R - d,\vartheta) \\ \tilde{\varepsilon}_{mem} \frac{\partial \Phi_2}{\partial r} = \tilde{\varepsilon}_{cyt} \frac{\partial \Phi_3}{\partial r} \end{cases} \qquad \text{at} \quad r = R - d.$$

With a reasoning similar to that of the Appendix B, it appears clear that only the constant $\tilde{a}$ present in the definition of Φ_1 needs for determination of the

effective dipole moment p_{eff}. From the previous conditions, $\tilde{a}$ assumes this form:

$$\tilde{a} = \frac{\tilde{\varepsilon}_{mem}\frac{\left(\frac{R}{R-d}\right)^3 + 2\frac{\tilde{\varepsilon}_{cyt}-\tilde{\varepsilon}_{mem}}{\tilde{\varepsilon}_{cyt}+2\tilde{\varepsilon}_{mem}}}{\left(\frac{R}{R-d}\right)^3 - \frac{\tilde{\varepsilon}_{cyt}-\tilde{\varepsilon}_{mem}}{\tilde{\varepsilon}_{cyt}+2\tilde{\varepsilon}_{mem}}} - \tilde{\varepsilon}_m}{\tilde{\varepsilon}_{mem}\frac{\left(\frac{R}{R-d}\right)^3 + 2\frac{\tilde{\varepsilon}_{cyt}-\tilde{\varepsilon}_{mem}}{\tilde{\varepsilon}_{cyt}+2\tilde{\varepsilon}_{mem}}}{\left(\frac{R}{R-d}\right)^3 - \frac{\tilde{\varepsilon}_{cyt}-\tilde{\varepsilon}_{mem}}{\tilde{\varepsilon}_{cyt}+2\tilde{\varepsilon}_{mem}}} + 2\tilde{\varepsilon}_m} R^3 E_0. \qquad \text{(D.1)}$$

Comparing this expression with the Eq. (B.10), rewritten below for clarity:

$$\tilde{a} = \frac{\tilde{\varepsilon}_p - \tilde{\varepsilon}_m}{\tilde{\varepsilon}_p + 2\tilde{\varepsilon}_m} R^3 E_0, \qquad \text{(B.10)}$$

it can be seen that $\tilde{\varepsilon}_p$ is substituted by a quantity which can be identified with the effective complex dielectric costant $\tilde{\varepsilon}_{eff}$:

$$\tilde{\varepsilon}_{eff} = \tilde{\varepsilon}_{mem}\frac{\left(\frac{R}{R-d}\right)^3 + 2\frac{\tilde{\varepsilon}_{cyt}-\tilde{\varepsilon}_{mem}}{\tilde{\varepsilon}_{cyt}+2\tilde{\varepsilon}_{mem}}}{\left(\frac{R}{R-d}\right)^3 - \frac{\tilde{\varepsilon}_{cyt}-\tilde{\varepsilon}_{mem}}{\tilde{\varepsilon}_{cyt}+2\tilde{\varepsilon}_{mem}}}. \qquad \text{(D.2)}$$

The electrostatic potential outside the layered spherical particle, that is for $r > R$, is therefore indistinguishable from that generated of the equivalent, homogeneous dielectric sphere of radius R with permittivity $\tilde{\varepsilon}_{eff}$. The cell is thus replaced in this model by an equivalent and homogeneous sphere with a radius equal to that of the cell and with dielectric characteristics represented by $\tilde{\varepsilon}_{eff}$, as shown in Fig. D.2.

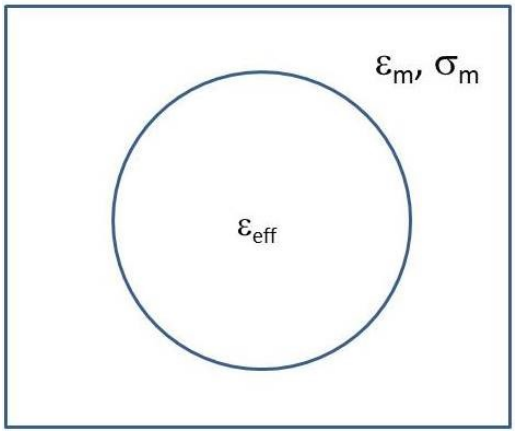

Fig. D.2 Effective equivalent homogeneous sphere model ruled by the dielectric function $\tilde{\varepsilon}_{eff}$.

Appendix E

MD-FEM code details

In this appendix we will describe with some additional details the procedures in the simulation code which are only briefly discussed in the main text of this Thesis work (Section 4.3). The full source can be found at the web page:

https://bitbucket.org/barolidavide/tumor_detection_dolfin/src/master/.

E.1 Mesh generation

A set of initialization and data exchange files is created to support simulations. In particular, the file Particles.xml contains, for each particle, the values of:

- center coordinates;
- velocity components;
- acceleration components;

whereas the Geometry.xml file contains the values of:

- number and width of electrodes and separation gap between them;
- width, depth and heigth of the box;
- particle radius (or radii).

The first step of the simulations is to generate the mesh for the computing domain relative to the initial configuration. Gmsh is used to create the mesh of the box and the spheres. The class "pygmsh" provides a Python interface for the Gmsh scripting language which can be fruitfully used to create the .geo Gmsh driver. Anyhow, a further adaptation must be considered and coded directly in python in order to generate automatically the electrodes' set. To create the mesh, the files Geometry.xml and Particles.xml are recalled to use all the parameters contained in them.
In general, the "subprocess" module provides an interface for working with additional processes and the "call()" function allows to run an external command without interacting with it. In the code, Subprocess.call() has been used to start Gmsh, which creates the mesh by the means of data contained in the cited files. The topological characteristics of the mesh are contained in a function called MeshFunction. We note that contrarily to the rest of the code the mesh generation performed by Gmsh is a serial computing procedure.
As well as the starting cycle of the simulations, the mesh generation is performed with the same procedure here indicated at the times $t = n_{DEP}\Delta t_{DEP}$, as explained in the Section 4.3.

E.2 Finite elements and Function Space generation

The FEniCS command "FiniteElement" creates the finite elements from "Unified Form-assembly Code finite element" (UFC), that is a unified framework assembling finite element variational forms. In the code, Pot_r refers to real part of electric potential scalar field, Pot_i to the imaginary one

and Pot_c (which is the product of Pot_r and Pot_i) to the whole complex potential:

```
Pot_r = FiniteElement("CG", mesh.ufl_cell(), degree_L-1)
Pot_i = FiniteElement("CG", mesh.ufl_cell(), degree_L-1)
Pot_c = Pot_r *Pot_i
```

The command “FunctionSpace” generates a finite element function space in FEniCS, on the base of the mesh and of Pot_c:

```
W = FunctionSpace(mesh,Pot_c)
```

E.3 Boundary conditions

The command “DirichletBC” imposes the Dirichlet boundary conditions. For this purpose, the various parts of the domain must be labelled. In the code, having indicated the number of particles with *N_particelle* we have the following labelling rules: a) integer numbers between 1 and *N_particelle* label the particles, b) the number *N_particelle* +7 labels the top surface of the domain box, c) *N_particelle* +2 the subdomain of its bottom surface consisting of the odd-numbered place electrodes where the electrical signal is applied, d) *N_particelle* +1 the subdomain of the bottom surface consisting of the even-numbered place electrodes where no signal is applied. The other boundaries are indicated by

numbers between *N_particelle* +3 and *N_particelle* +6. The command contains four arguments: the function space, the value to be imposed as a boundary condition, the MeshFunction and the subdomain index. In the code, the command is written as following:

```
bcs = [
       DirichletBC(W.sub(0), 0.0, mf, N_particelle+7),
       DirichletBC(W.sub(0), V_rms, mf, N_particelle+2),
       DirichletBC(W.sub(0), 0.0, mf, N_particelle+1),
       DirichletBC(W.sub(1), 0.0, mf, N_particelle+7),
       DirichletBC(W.sub(1), 0.0, mf, N_particelle+2),
       DirichletBC(W.sub(1), 0.0, mf, N_particelle+1)
       ]
```

where W.sub(0) and W.sub(1) refers to the subspaces relative to the real and imaginary electric potential, respectively, V_rms is the root mean square value of the applied electrical signal, mf is the MeshFunction.

E.4 Solution of Laplace' problem

The linear form *L* and the bilinear form *a* are written as described in the section 3.3.1. The function *u* to be derived and the problem (which has the bilinear and linear forms, the function and the boundary conditions as arguments) are defined and the solution is finally obtained through the specific Fenics command "solve()":

```
u = Function(W)
problem=LinearVariationalProblem(a,L,u,bcs)
solver= LinearVariationalSolver(problem)
solver.solve()
```

Through the “project” command of FEniCS, the vector solution of the electric field is derived from the solution of the scalar field u. The formula of Eq. (1.29) is finally implemented to calculate the e.mec. force due to e.m. field. This force is added vectorially to single particle external forces and the equations of motion are integrated by Velocity Verlet algorithm. Before starting the new cycle, the file Particles.xml is updated with new values of the particle centers, velocities and accelerations. As claimed, unlike the mesh generation, the processes here described here are parallelized.

E.5 Control instructions

The code includes control instructions on particle-wall and steric particle-particle interactions: in fact, particles must never exceed the walls of the simulation box in their dynamics and, moreover, must not penetrate each other. For each MD step, a check is carried out: if one or both of these events occur, it modifies the positions of the particles as explained below.

E.5.1 Particle-wall interactions

The interaction between the particles and the walls is conceived as an elastic impact: if the surface of a particle is found to have crossed a wall of the box in a MD step, its center is associated with new values of speed and position. The problem is addressed in terms of components of the position vector expressed in Cartesian coordinates. The coordinates (x ,y ,z)

are related respectively to length, depth and height of the box. Let's consider the *y* coordinate as an example. The condition is expressed as follows: if in a specific time step the sum of the coordinate *y* of the particle center and the radius is greater than the depth of the simulation box, then the value of the component *y* of the velocity (v_y) is replaced by the opposite value and the coordinate *y* is replaced by that which the particle had at the previous time step (called y_{old}); the same is true if the difference between the coordinate *y* and the radius is less than zero. In formula, if either of these two conditions occurs, the new values of velocity and position are:

$$v_y' = -v_y, \tag{E.1}$$

$$y' = y_{old}. \tag{E.2}$$

E.5.2 Overlapping between particles

In the case of overlapping between particles, the check changes the positions of the particles, so that contact and/or penetration are prevented. Such measures avoid non-physical situations since the particles are impenetrable. Moreover the eventual overlap leads to conflicts in the generation of the mesh at the computational phase.

The minimum physical distance between the centers of two spherical particles is obviously equal to the sum of the radii. A minimum distance has been defined, called *control distance* D_c, equal to the sum of the radii added to a small amount. The purpose of the control check is to avoid that as a

result of a time step of MD the two particles have the centers that are less distant than D_c, in order to prevent the contact between the two. A check is made on each particle pair; it consists of the following points.

Considering the particle 1 with coordinates (x_1, y_1, z_1) and the particle 2 with coordinates (x_2, y_2, z_2), the distance D between the two is calculated:

$$D = \sqrt{(x_1 - x_2)^2 + (y_1 - y_2)^2 + (z_1 - z_2)^2}. \quad \text{(E.3)}$$

The direction cosines are calculated as follows:

$$\cos(\widehat{rx}) = \frac{x_1 - x_2}{\sqrt{(x_1 - x_2)^2 + (y_1 - y_2)^2 + (z_1 - z_2)^2}};$$

$$\cos(\widehat{ry}) = \frac{y_1 - y_2}{\sqrt{(x_1 - x_2)^2 + (y_1 - y_2)^2 + (z_1 - z_2)^2}};$$

$$\cos(\widehat{rz}) = \frac{z_1 - z_2}{\sqrt{(x_1 - x_2)^2 + (y_1 - y_2)^2 + (z_1 - z_2)^2}}.$$

If $x_1 > x_2$, the x-coordinates of the two particles are changed according to the following formulas:

$$x_1' = x_1 + \frac{1}{2}(D_c - D)\ \cos(\widehat{rx}), \quad \text{(E.4)}$$

$$x_2' = x_2 - \frac{1}{2}(D_c - D)\ \cos(\widehat{rx}). \quad \text{(E.5)}$$

If instead $x_1 < x_2$, the new coordinates become:

$$x_1' = x_1 - \frac{1}{2}(D_c - D)\ \cos(\widehat{rx}),$$

$$x_2' = x_2 + \frac{1}{2}(D_c - D)\ \cos(\widehat{rx}).$$

Considering for example the first case, by subtracting Eq. (E.5) from Eq. (E.4), the projection along the *x*-axis of the new distance D' is:

$$x_1' - x_2' = x_1 - x_2 + (D_c - D)\cos(\widehat{rx}). \quad \text{(E.6)}$$

Similar formulas apply to the *y* and *z* coordinates of the two particles, in which $\cos(\widehat{ry})$ e $\cos(\widehat{rz})$ respectively appear:

$$y_1' - y_2' = y_1 - y_2 + (D_c - D)\cos(\widehat{ry}), \quad \text{(E.7)}$$

$$z_1' - z_2' = z_1 - z_2 + (D_c - D)\cos(\widehat{rz}). \quad \text{(E.8)}$$

The new distance is:

$$D' = \sqrt{(x_1' - x_2')^2 + (y_1' - y_2')^2 + (z_1' - z_2')^2}. \quad \text{(E.9)}$$

By replacing the Eq.s (E.6), (E.7) and (E.8) in the Eq. (E.9), D' becomes:

$$D' = D_c. \quad \text{(E.10)}$$

Following a check due to contact or overlap between two particles, the new distance is then equal to D_c.

Appendix F

Re$\{f_{CM}\}$ of MDA-MD-231 cells and B-Lymphocites

In this Appendix, the shapes of the Re$\{f_{CM}\}$ curves of MDA-MD-231 cells and the B-Lymphocites, shown in Fig. 5.12, are commented and explained with particular regard to limit values.
In Chap. 1 the following quantities was been introduced:

- the definition of complex permittivity of a particle and of the liquid medium:

$$\tilde{\varepsilon}_m = \varepsilon_m - i\frac{\sigma_m}{\omega}, \tag{1.10.a}$$

$$\tilde{\varepsilon}_p = \varepsilon_p - i\frac{\sigma_p}{\omega}; \tag{1.10.b}$$

- the CM factor f_{CM}:

$$f_{CM} = \frac{\tilde{\varepsilon}_p - \tilde{\varepsilon}_m}{\tilde{\varepsilon}_p + 2\tilde{\varepsilon}_m} = \frac{\varepsilon_p - \varepsilon_m - i\frac{\sigma p - \sigma m}{\omega}}{\varepsilon_p + 2\varepsilon_m - i\frac{\sigma p + 2\sigma m}{\omega}}; \tag{1.15}$$

- $\mathrm{Re}\{f_{CM}\} = \frac{(\varepsilon_p - \varepsilon_m)(\varepsilon_p + 2\varepsilon_m) - \frac{1}{\omega^2}(\sigma_m - \sigma_p)(\sigma_p + 2\sigma_m)}{(\varepsilon_p + 2\varepsilon_m)^2 + \frac{1}{\omega^2}(\sigma_p + 2\sigma_m)^2}$; (1.16)

- the limits of Re$\{f_{CM}\}$ for low and high frequencies:

$$\lim_{\omega\to\infty} \mathrm{Re}\{f_{CM}\} = \frac{\varepsilon_p - \varepsilon_m}{\varepsilon_p + 2\varepsilon_m}, \tag{1.19}$$

$$\lim_{\omega\to 0} \mathrm{Re}\{f_{CM}\} = \frac{\sigma_p - \sigma_m}{\sigma_p + 2\sigma_m}. \tag{1.20}$$

In the previous equations, if a dielectric particle of a given material is considered, the values ε_p, σ_p, ε_m, σ_m are constant. In Chap. 5, the effective permittivity $\tilde{\varepsilon}_{eff}$ (Eq. (5.7)) was introducted within the shelled model adopted for the cells, explaining that in this case the permittivity $\tilde{\varepsilon}_p$ must be replaced with $\tilde{\varepsilon}_{eff}$. By comparing the Eq. (1.10b) with the expression:

$$\tilde{\varepsilon}_{eff} = \mathrm{Re}\{\tilde{\varepsilon}_{eff}\} + i\mathrm{Im}\{\tilde{\varepsilon}_{eff}\},$$

the following replacements must be carried out:

- $\varepsilon_p \rightarrow \mathrm{Re}\{\tilde{\varepsilon}_{eff}\}$;
- $\sigma_p \rightarrow -\omega\, \mathrm{Im}\{\tilde{\varepsilon}_{eff}\}$.

It is important to note that both $\mathrm{Re}\{\tilde{\varepsilon}_{eff}\}$ and $\mathrm{Im}\{\tilde{\varepsilon}_{eff}\}$ are frequency dependent. Consequently, unlike the case of a dielectric particle of a given material (characterized by constant parameters ε_p and σ_p), within the shell model the quantities concerning the particle depend on the frequency. Figure F.1 and F.2 show $\mathrm{Re}\{\tilde{\varepsilon}_{eff}\}$ and the quantity $-\omega\, \mathrm{Im}\{\tilde{\varepsilon}_{eff}\}$ (which is here called *effective conductivity* and indicated by σ_{eff}) of MDA-MD-231 and of the B-Lymphocities.

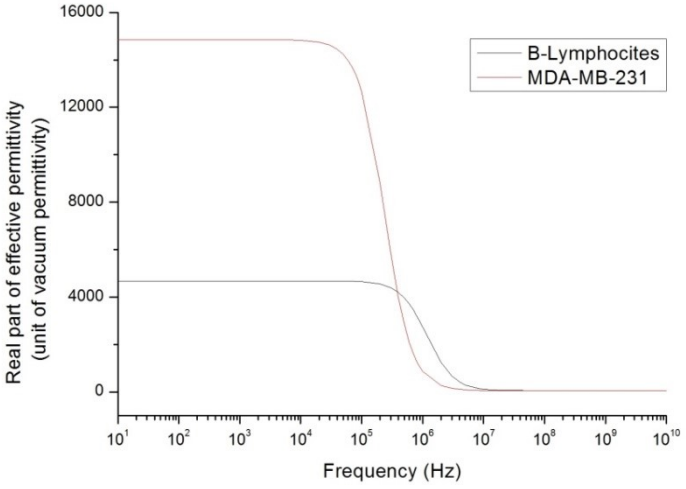

Fig. F.1 Re$\{\tilde{\varepsilon}_{eff}\}$ of MDA-MD-231 and of the B-Lymphocites.

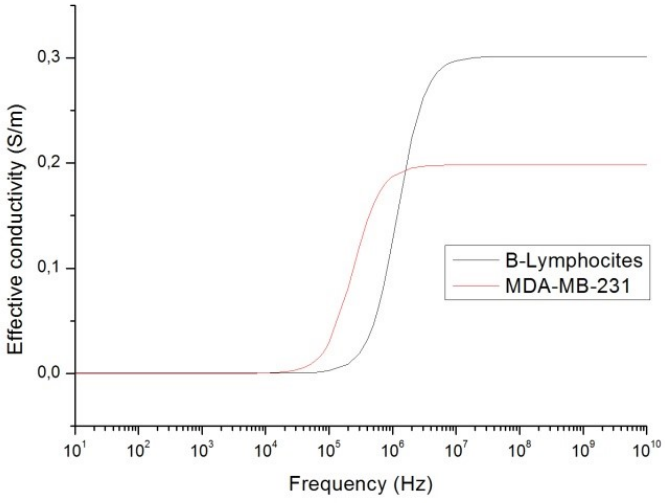

Fig. F.2 σ_{eff} of MDA-MD-231 and of the B-Lymphocites.

To explain the shapes of $\mathrm{Re}\{f_{CM}\}$ of MDA-MB-231 and of B-Lymphocites shown in Fig 5.12, it is necessary to enter the high frequency limit of $\mathrm{Re}\{\tilde{\varepsilon}_{eff}\}$ in Eq. (1.19) in the place of ε_p and the low frequency limit of effective conductivity σ_{eff} in Eq. (1.20) in the place of σ_p (as already highlighted, $\varepsilon_m = 79\,\varepsilon_0$ and $\sigma_m = 0.03\,S/m$ do not depend on the frequency and are constant). These values are:

- MDA-MB-231: $\lim_{\omega\to\infty} \mathrm{Re}\{\tilde{\varepsilon}_{eff}\} \approx 49.8\ \varepsilon_0$
- B-Lymphocites $\lim_{\omega\to\infty} \mathrm{Re}\{\tilde{\varepsilon}_{eff}\} \approx 58.2\ \varepsilon_0$
- MDA-MB-231: $\lim_{\omega\to 0} \sigma_{eff} \approx 6.2 \cdot 10^{-5}$ S/m
- B-Lymphocites $\lim_{\omega\to 0} \sigma_{eff} \approx 3.3 \cdot 10^{-4}$ S/m.

As a result, according to the Fig. 5.12, these replacements give the following results:

- MDA-MB-231:
  $\lim_{\omega\to\infty} \mathrm{Re}\{f_{CM}\} \approx -0.14$;
  $\lim_{\omega\to 0} \mathrm{Re}\{f_{CM}\} \approx -0.096$;

- B-Lymphocites :
  $\lim_{\omega\to\infty} \mathrm{Re}\{f_{CM}\} \approx -0.498$;
  $\lim_{\omega\to 0} \mathrm{Re}\{f_{CM}\} \approx -0.496$.

References

[1] J. Castillo, S. Tanzi, M. Dimaki and W. Svendsen, Electrophoresis **29**, (2008)

[2] B. Cetin and D. Li, Electrophoresis, **32**, (2011)

[3] M. Duchamp, K. Lee, B. Dwir, J. W. Seo, E. Kapon, L. Forro and A. Magrez, ACS Nano **4**, (2010)

[4] Y. Shen, E. Elele and B. Khusid, Electrophoresis **32**, (2011)

[5] A. Magliano, M. Camarda, S. F. Lombardo, R. Di Martino, M. Cascio, A. Romano, L. Minafra, G. Russo, M. C. Gilardi, F. Di Raimondo, S. Scalese and A. La Magna, Sensing and Bio-Sensing Research **8**, 59-64 (2016).

[6] R. Di Martino, M. Camarda, M. Cascio, Michele G., A. Magliano, S. Baldo, A. Romano, L.Minafra, G. I. Forte, G. Russo, M. C. Gilardi, F. Di Raimondo, S. Scalese and A. La Magna, Sensing and Bio-Sensing Research **7**, 162-167 (2016).

[7] T. B. Jones, IEEE Engineering in Medicine and Biology Magazine, (2003)

[8] P. R. C. Gascoyne, J. Noshari, T. J. Anderson, F. F. Becker, Electrophoresis, **30**, (2009)

[9] J. Cao, P. Cheng, F. Hong, Journal of Electrostatics **66**, (2008)

[10] R. Natu and R. Martinez-Duarte, Micromachines **7**, 2016

[11] B. Hwang, D. Lee, B. Kim and J. Lee, Journal of Mechanical Science and Technology **30**, (2016)

[12] D. Lee, D. Kim, Y. Kim, K. Park, E. Oh, Y. Kim and B. Kim, Journal of Laboratory Automation **19**, (2014)

[13] M. Sancho, V. Giner and G. Martinez, Phys. Rew. E **55**, (1997)

[14] A. La Magna, M. Camarda, I. Deretzis, G. Fisicaro, and S. Coffa, Appl. Phys. Lett. 100, (2012);

[15] O. E. Nicotra, A. La Magna, and S. Coffa, Appl. Phys. Lett. 93, 193902 (2008)

[16] O. E. Nicotra, A. La Magna, S. Coffa, Appl. Phys. Lett. **95**, (2009)

[17] M. Camarda, S. Scalese, and A. La Magna, Electrophoresis **36**, (2015)

[18] Michele Cascio, Davide Baroli, Stephane Bordas, Ioannis Deretzis, Giuseppe Falci, Antonino Magliano and Antonino La Magna, submitted to Physical Review E

[19] X. Wang, X. B. Wang, P. R.C. Gascoyne, Journal of Electrostatics **39**, (1997)

[20] Michael P. Allen, *Introduction to Molecular Dynamics Simulation*, Computational Soft Matter, Vol. 23, ISBN 3-00-012641-4, 2004.

[21] https://fenicsproject.org/

[22] http://gmsh.info/

[23] T. B. Jones, Electromechanics of particles, Cambridge University Press, 2005

[24] H. Pohl, The Motion and Precipitation of Suspensoids in Divergent Electric Fields, Applied Physics **22**, 869-871 (1951)

[25] J. D. Jackson, Classical Electrodynamics, Wiley, New York, 1978

[26] A. Gonzalez, A. Ramos, H. Morgan, N.G. Green, A. Castellanos, J. Fluid Mech. **564**, (2006)

[27] L. G. Leal, Advanced Transport Phenomena: Fluid Mechanics and Convective Transport Processes, Artech House, New York, USA 2006.

[28] F. Aldaeus, Y. Lin, J. Roeraade, and G. Amberg, Electrophoresis **26**, 4252 (2005).

[29] Landau L.D. , Lifshi tz E.M., Electrodynamics of continous media, Pergamon Press, 1984.

[30] X. Wang, X.-B. Wang, P. R.C. Gascoyne, General expressions for dielectrophoretic force and electrorotational torque derived using the Maxwell stress tensor method, Journal of Electrostatics **39** (1997) 277-295

[31] A. M. Benselama, P. Pham, P. Atten, Calcul de la force dielectrophoretique dans les microsystemes biologiques: comparaison du modele dipolaire avec le modele du tenseur de Maxwell, Journal of Electrostatics **64**, 437–444 (2006)

[32] Carlos Rosales, Kian Meng Lim, Electrophoresis **26**, 2005, 2057–2065

[33] A Al-Jarro *et al., J. Phys. D: Appl. Phys.* **40**, 2007, 71

[34] S. Kumar, P. J. Hesketh, Interpretation of ac dielectrophoretic behavior of tin oxide nanobelts using Maxwell stress tensor approach modeling, Sensors and Actuators B 161, 1198– 1208 (2012)

[35] Dho-Hyoung Lee, Chengjie Yu, Papazoglou E., Bakhtier F., H. M. Noh, Dielectrophoretic particle–particle interaction under AC electrohydrodynamic flow conditions, Electrophoresis **32**, 2298-2306 (2011)

[36] O. E. Nicotra, A. La Magna, and S. Coffa, Appl. Phys. Lett. 93, 193902 (2008)

[37] R. Landauer, J. Appl. Phys. 23, 779 (1952); A. N. Norris, P. Sheng, and A. J. Callegari, ibid. **57**, 1990 (1985).

[38] A. T. J. Kadaksham, P. Singh, and N. Aubry, Electrophoresis **25**, 3625, (2004)

[39] W. M. Arnold, H. P. Schwan, and U. Zimmermann, J. Phys. Chem. **91**, 5093 (1987).

[40] L. D. Landau and E. M. Lifshitz, *Fluid Mechanics*, Butterworth-Heinemann, Oxford, 1987.

[41] K. H. Kang, Y. Kang, X. Xuan, and D. Li, Electrophoresis **27**, 694 (2006).

[42] V. Giner, M. Sancho, R. S. Lee, G. Martinez, and R. Pethig, J. Phys. D 32, 1182 (1999).

[43] O. E. Nicotra, A. La Magna, and S. Coffa, Appl. Phys. Lett. 95, 073702 (2009);

[44] A. La Magna, G. Fisicaro, G. Mannino, V. Privitera, G. Piccitto, B. G. Svensson, and L. Vines, Mater. Sci. Eng., B 154–155, **35** (2008).

[45] A. La Magna, M. Camarda, I. Deretzis, G. Fisicaro, and S. Coffa, Appl. Phys. Lett. 100, (2012);

[46] M. Sancho, V. Giner, and G. Martinez, Phys. Rev. E **55**, 544 (1997).

[47] K. H. Kang and D. Li, Langmuir **22**, 1602 (2006).

[48] N. Blow, Nat. Methods 6, 683 (2009).

[49] Camarda M., Scalese S., La Magna A., Electrophoresis **36**, (2015).

[50] https://www.comsol.com/

[51] K. F. Riley, M. P. Hobson, S. J. Bence, Mathematical Methods for Physics and Engineering, Cambridge, 2006

[52] M. L. Boas, Mathematical Methods in the Physical Sciences, Wiley, 2005

[53] H. P. Langtangen and K.-A. Mardal, Introduction to Numerical Methods for Variational Problems, 2016, http://hplgit.github.io/fem-book/doc/web/

[54] A. Logg, K.-A. Mardal, and G. N. Wells, Automated Solution of Partial Differential Equations by the Finite Element Method, Springer, 2012.

[55] M. G. Larson, F. Bengzon, *The Finite Element Method: Theory, Implementation, and Applications*, Springer, 2013

[56] https://fenicsproject.org/

[57] https://gmsh.info/

[58] https://www.salome-platform.org/

[59] D. Marx and J. Hutter, *Modern Methods of quantum chemistry*, FZ Julich, 2000

[60] M. P. Allen, *Introduction to Molecular Dynamics Simulation*, Computational Soft Matter, Vol. 23, ISBN 3-00-012641-4, 2004.

[61] Thijs J.H. Vlugt, Jan P.J.M. van der Eerden, Marjolein Dijkstra, Berend Smit, Daan Frenkel, *Introduction to Molecular Simulation and Statistical Thermodynamics*, ISBN: 978-90-9024432-7, The Netherlands, 2008

[62] L. Verlet, *Computer "Experiments" on Classical Fluids. I. Thermodynamical Properties of Lennard−Jones Molecules*, Physical Review 159: 98–103

[63] A. W. Sandvik, *Numerical Solutions of Cassical Equations of Motion*, PY 502, Computational Physics (Fall 2013)

[64] Hairer, Lubich, Wanner, Geometric numerical integration illustrated by the Störmer/Verlet method, Acta Numerica 12: 399–450, 2003

[65] B. J. Alder and T. E. Wainwright, Studies in Molecular Dynamics. I. General Method, The Journal of Chemical Physics **31**, 459 (1959)

[66] F. H. Stillinger and A. Rahman, J. Chern. Phys., Vol. 60, No.4 (1974)

[67] J. Barojas, D. Levesque, and B. Quentrec, Simulation of Diatomic Homonuclear Liquids, Phys. Rev. A 7, 1092 (1973)

[68] J.-P. Ryckaert, A. Bellemans, Molecular dynamics of liquid n-butane near its boiling point, Chemical Physics Letters 30(1):123-125 · January 1975

[69] Pierre Turq, Frédéric Lantelme, Harold L. Friedman, Brownian dynamics: Its application to ionic solutions, The Journal of Chemical Physics **66**, 3039 (1977)

[70] Michael L. Klein and Ian R. McDonald, Structure and dynamics of associated molecular systems. I. Computer simulation of liquid hydrogen fluoride, The Journal of Chemical Physics **71**, 298 (1979)

[71] G. Henkelman et al., J. Chem. Phys. **113**, (2000)

[72] A. Laio and F. Gervaso, Rep. Progr. Phys. **71**, (2008)

[73] F. F. Abraham et al. Phys. Rev. B **60**, 2391, (1999)

[74] Michael P. Allen, Introduction to Molecular Dynamics Simulation, *John von Neumann Institute for Computing, Julich, NIC Series, Vol.* 23*, ISBN 3-00-012641-4*

[75] Martin Karplus, J. Andrew McCammon, Molecular dynamics simulations of biomolecules,*Nature Structural Biology* volume9, pages646–652 (2002)

[76] Adam Hospital, Josep Ramon Goñi, Modesto Orozco, and Josep L Gelpí, ,Molecular dynamics simulations: advances and applications, Adv Appl Bioinform Chem. 8, (2015)

[77] R Car, M Parrinello, Unified approach for molecular dynamics and density-functional theory, Physical review letters 55, 1985

[78] U.M. Ascher e Linda R. Petzold, *Computer Methods for Ordinary Differential Equations and differential-Algebraic Equations*, Philadelphia, Society for Industrial and Applied Mathematics, 1998, ISBN 978-0-89871-412-8.

[79] http://gmsh.info/doc/texinfo/gmsh.html

[80] Peter R. C. Gascoyne and Jody Vykoukal, *Electrophoresis*. 2002 July ; 23(13): 1973–1983.

[81] L. G. Leal, *Advanced Transport Phenomena: Fluid Mechanics and Convective Transport Processes*, Artech House, New York, USA 2006.

[82] Houhui Yi, Chinese Journal of Physics. **52**, (2014)

[83] J. B. McLaughlin, Phys. Fluids A **1**, (1989)

[84] X. Wang, J. Vykoukal, F. F. Becker and P. Gascoyne, Biophysical Journal **74**, (1998)

[85] A. Rosenthal and J. Voldman, Biophysical Journal Volume **88**, (2005)

[86] P. S. Williams, Koch, T. and Giddings, Chem. Eng.Commun. **111**, (1992)

[87] F. F. Becker, X. B. Wang, Y. Huang, R. Pethig, J. Vykoukal, and P. Gascoyne, *Proceedings of the National Academy of Sciences* **92**, 1995

[88] J. Zhang, K. Chen and Z.H. Fan, Adv. Clin Chem. **75**, 2016

[89] M. Sancho, G. Martinez, C. Martin, Journal of Electrostatics **57**, (2003)

[90] P. Litzkas, K. Jha and H. Ozer, molecular and cellular biology 4 (1984).

[91] Pontecorvo, G., Somat Cell Mol Genet (1975) 1: 397. https://doi.org/10.1007/BF01538671

[92] P. Gascoyne, X. Wang, Y. Huang and F. Becker, IEEE Transactions on Industry Applications **33**, (1997)

[93] P. Gascoyne, C. Mahidol, M. Ruchirawat, J. Satayavivad, P. Watcharasit and F. F. Becker, Lab on a Chip **2**, (2002)

[94] P. Gascoyne, S. Shim, J. Noshari, F. F. Becker, K. Stemke-Hale, Electrophoresis **34**, (2013)

[95] S. Shim, P. Gascoyne, J. Noshari and K.S. Hale, Integr Biol (Camb) 3(8), 2011

[96] S. Fan, C. Chiu, and P. Huang, Biomicrofluidics **4**, (2010)

[97] T.B. Jones, Journal of Electrostatics **25** (1990)

[98] B. Yafouz1, N.A. Kadri1, F. Ibrahim, IEEE EMBS International Conference on Biomedical Engineering and Sciences, (2012)

[99] J. Auerswald and H. F. Knapp, Microelectronic engineering **67**, (2003)

[100] X. B. Wang, Y. Huang, X. Wang, F. F. Becker, and P. Gascoyne, Biophysical Journal **72**, (1997)

[101] K. Khoshmanesh, C. Zhang, F. J. T. Lopez, S. Nahavandi, S. Baratchi, K. Kalantar and A. Mitchell, Electrophoresis **30**, (2009)

[102] M. S. Pommer, Y. Zhang, N. Keerthi, D. Chen, J. A. Thomson, C. D. Meinhart, and H. T. Soh, Electrophoresis **29**, (2008)

[103] L. S. Jang, P. H. Huang, and K. C. Lan, Biosensors and Bioelectronics **24**, (2009)

[104] H. O. Fatoyinbo, N. A. Kadri, D. H. Gould, K. F. Hoettges, and F. H. Labeed, Electrophoresis **32**, (2011)

[105] M. P. Hughes and H. Morgan, Journal of Physics D: Applied Physics **31**, (1998)

[106] D.F. Chen, H. Du, Simulation studies on electrothermal fluid flow induced in a dielectrophoretic microelectrode system, Journal of Micromechanics and Microengineering **16**, (2006) 2411–2419

[107] Jun Cao, Ping Cheng, Fangjun Hong, A numerical analysis of forces imposed on particles in conventional dielectrophoresis in microchannels with interdigitated electrodes, Journal of Electrostatics **66**, (2008) 620–626

[108] N. Crews, J. Darabi, P. Voglewede, F. Guo, A. Bayoumi, Sensors and Actuators B **125**, (2007)

[109] M. Camarda, G. Fisicaro, R. Anzalone, S. Scalese S, A. Alberti A, F. La Via, A. La Magna, A. Ballo, G. Giustolisi, L. Minafra, F. P. Cammarata, V. Bravatà, G. I. Forte, G. Russo, M.C. Gilardi, BioMedical Engineering OnLine **13**, (2014)

[110] D. Lee, D. Kim, Y. Kim, K. Park, E. Oh, Y. Kim and B. Kim, A Negative Dielectrophoresis and Gravity-Driven Flow-Based High-Throughput and High-Efficiency Cell-Sorting System, Journal of Laboratory Automation, Vol. 19(1), 2014.

[111] H. Goldstein, *Classical Mechanics*, 2nd ed., Addison-Wesley, London, (1981).

[112] A. Rahman and F. H. Stillinger, J. Chem. Phys. **55**, 3336 (1971).

[113] T.W.B. Kibble, Classical Mechanics, McGraw-Hill International Editions, London, (1973)

[114] D. Rozmanov and P. G. Kusalik, *Robust rotational-velocity-Verlet integration methods*, Physical Review E **81**, (2010)

[115] M. Svanberg, Mol. Phys. **92**, 1085 (1997).

[116] J. B. Kuipers, *Quaternions and Rotation Sequences*, Princeton University Press, Princeton, New Jersey, (1998).

[117] L.A. Kaluzhnin, "Introduction to general algebra" , Moscow (1973)

[118] I.L. Kantor, A.S. Solodovnikov, "Hyperkomplexe Zahlen" , Teubner (1978)

[119] A.G. Kurosh, "Higher algebra" , MIR (1972)

[120] M. Bramanti, C. D. Pagani, S. Salsa, Matematica calcolo infinitesimale e algebra lineare, 2° ed., Zanichelli.

[121] D. J. Evans, Mol. Phys. **34**, 317 (1977).

[122] D. J. Evans and S. Murad, Mol. Phys. **34**, 327 (1977).

[123] M. Svanberg, Mol. Phys. **92**, 1085 (1997)

[124] Bernards R, Weinberg RA, Nature. 2002; 418(6900):823.

[125] Kling J. Beyond counting tumor cells. Nat Biotechnol. 2012; 30(7):578–580.

[126] P. R. C. Gascoyne, J. Noshari, T. J. Anderson, F. F. Becker, Electrophoresis 30 (2009) 1388-98;

[127] Pantel K, Brakenhoff RH, Brandt B. Detection, clinical relevance and specific biological properties of disseminating tumour cells. Nat Rev Cancer. 2008; 8(5):329–340.

[128] Ashworth T. A case of cancer in which cells similar to those in the tumours were seen in the blood after death. Aust Med J. 1869; 14:146–147.

[129] Kaiser J. Cancer's circulation problem. Science. 2010; 327(5969):1072–1074.

[130] van de Stolpe A, et al. Circulating tumor cell isolation and diagnostics: toward routine clinical use. Cancer Res. 2011; 71(18):5955–5960.

[131] Chaffer CL, Weinberg RA. A perspective on cancer cell metastasis. Science. 2011; 331(6024):1559–1564.

[132] Chambers AF, Groom AC, MacDonald IC. Dissemination and growth of cancer cells in metastatic sites. Nat Rev Cancer. 2002; 2: 563-572.

[133] Lam HM, Vessella RL, Morrissey C. The role of the microenvironment-dormant prostate disseminated tumor cells in the bone marrow. Drug Discov Today Technol. 2014; 11: 41-47.

[134] Morgan TM, et al. Disseminated tumor cells in prostate cancer patients after radical prostatectomy and without evidence of disease predicts biochemical recurrence. Clin Cancer Res. 2009; 15(2):677–683.

[135] Fan T, et al. Clinical significance of circulating tumor cells detected by an invasion assay in peripheral blood of patients with ovarian cancer. Gynecol Oncol. 2009; 112(1):185–191

[136] Chaffer CL, Weinberg RA. A perspective on cancer cell metastasis. Science. 2011; 331(6024):1559–1564.

[137] Bernards R, Weinberg RA. Metastasis genes: a progression puzzle. Nature. 2002; 418(6900):823.

[138] Kling J. Beyond counting tumor cells. Nat Biotechnol. 2012; 30(7):578–580.

[139] Crowley E, et al. Liquid biopsy: monitoring cancer-genetics in the blood. Nat Rev Clin Oncol. 2013; 10(8):472–484.

[140] Helo P, et al. Circulating prostate tumor cells detected by reverse transcription-PCR in men with localized or castration-refractory prostate cancer: concordance with Cel-lSearch assay and association with bone metastases and with survival. Clin Chem. 2009; 55(4):765–773.

[141] Maheswaran S, et al. Detection of mutations in EGFR in circulating lung-cancer cells. N Engl J Med. 2008; 359(4):366–377

[142] Dharmasiri U, et al. Microsystems for the capture of low-abundance cells. Annu Rev Anal Chem. 2010;

[143] Cohen SJ, et al. Relationship of circulating tumor cells to tumor response, progression-free survival, and overall survival in patients with metastatic colorectal cancer. J Clin Oncol. 2008; 26(19):3213–3221.

[144] Wong SCC, et al. Clinical significance of cytokeratin 20-positive circulating tumor cells detected by a refined immunomagnetic enrichment assay in colorectal cancer patients. Clin Cancer Res. 2009; 15(3):1005–1012.

[145] Cristofanilli M, et al. Circulating tumor cells, disease progression, and survival in met-astatic breast cancer. N Engl J Med. 2004; 351(8):781–791.

[146] Pachmann K, et al. Monitoring the response of circulating epithelial tumor cells to adjuvant chemotherapy in breast cancer allows detection of patients at risk of early relapse. J Clin Oncol. 2008; 26(8):1208–1215.

[147] Danila DC, et al. Circulating tumor cell number and prognosis in progressive castration-resistant prostate cancer. Clin Cancer Res. 2007; 13(23):7053–7058.

[148] Morgan TM, et al. Disseminated tumor cells in prostate cancer patients after radical prostatectomy and without evidence of disease predicts biochemical recurrence. Clin Cancer Res. 2009; 15(2):677–683.

[149] Uen YH, et al. Persistent presence of postoperative circulating tumor cells is a poor prognostic factor for patients with stage I-III colorectal cancer after curative resection. Ann Surg Oncol. 2008; 15(8):2120–2128.

[150] Helo P, et al. Circulating prostate tumor cells detected by reverse transcription-PCR in men with localized or castration-refractory prostate cancer: concordance with Cel-lSearch assay and association with bone metastases and with survival. Clin Chem. 2009; 55(4):765–773.

[151] Guo J, et al. Detecting carcinoma cells in peripheral blood of patients with hepato-cellular carcinoma by immunomagnetic beads and rt-PCR. J Clin Gastroenterol. 2007; 41(8):783–788.

[152] Riethdorf S, et al. Detection of circulating tumor cells in peripheral blood of patients with metastatic breast cancer: a validation study of the Cell Search system. Clin Cancer Res. 2007; 13(3):920–928

[153] Krivacic RT, et al. A rare-cell detector for cancer. Proc Natl Acad Sci USA. 2004; 101(29):10501–10504.

[154] Zieglschmid V, Hollmann C, Bocher O. Detection of disseminated tumor cells in peripheral blood. Crit Rev Clin Lab Sci. 2005; 42(2):155–196.

[155] Racila E, et al. Detection and characterization of carcinoma cells in the blood. Proc Natl Acad Sci USA. 1998; 95(8):4589–4594

[156] Alix-Panabieres C, Pantel K. Challenges in circulatingtumour cell research. Nat Rev Cancer. 2014; 14: 623-631.

[157] Barradas AM, Terstappen LW. Towards the biological understanding of CTC: capture technologies, definitions and potential to create metastasis. Cancers (Basel). 2013; 5: 1619-1642.

[158] Gross HJ, Verwer B, Houck D, Hoffman RA, Recktenwald D. Model study detecting breast cancer cells in peripheral
blood mononuclear cells at frequencies as low as 10(-7). Proc Natl Acad Sci U S A. 1995

[159] Sangio Shim, Gascoyne P., Noshari J., Hale K., Integrative Biology, 8 (2013)

[160] M. P. Huges, Strategies for dielectrophoretic separation in laboratory-on-a-chip systems, Electrophoresis 23 (2002) 2569

[161] M. Duchamp, K. Lee, B. Dwir, J. W. Seo, E. Kapon, L. Forro and A. Magrez, Controlled positioning of Carbon Nanotubes by dielectrophoresis, ACS Nano 4 (2010) 279

[162] Manz A, et al. Planar chips technology for miniaturization and integration of separation techniques into monitoring systems—capillary electrophoresis on a chip. J Chromatogr. 1992; 593(1–2):253–258.

[163] Sia SK, Whitesides GM. Microfluidic devices fabricated in poly(dimethylsiloxane) for biological studies. Electrophoresis. 2003; 24(21):3563–3576

[164] Simmons JK, Hildreth BE, Supsavhad W, Elshafae SM, Hassan BB, Dirksen WP, Toribio RE, Rosol TJ. Animal Models of Bone Metastasis. Vet Pathol, 2015. 52(5): 827-841.

[165] Adams AA, et al. Highly efficient circulating tumor cell isolation from whole blood and label-free enumeration using polymer-based microfluidics with an integrated conductivity sensor. J Am Chem Soc. 2008; 130(27):8633–8641

[166] Nagrath S, et al. Isolation of rare circulating tumour cells in cancer patients by micro-chip technology. Nature. 2007; 450(7173):1235–1239

[167] Gleghorn JP, et al. Capture of circulating tumor cells from whole blood of prostate cancer patients using geometrically enhanced differential immunocapture (GEDI) and a prostate-specific antibody. Lab Chip. 2010; 10(1):27–29.

[168] Stott SL, et al. Isolation of circulating tumor cells using a microvortex-generating herringbone-chip. Proc Natl Acad Sci USA. 2010;
[169] Sheng W, et al. Capture, release and culture of circulating tumor cells from pancreatic cancer patients using an enhanced mixing chip. Lab Chip. 2014
[170] Emma E. van der Toom, James E. Verdone, Michael A. Gorin and Kenneth J. Pienta, Oncotarget, Vol. 7, No. 38
[171] Vona G, et al. Isolation by size of epithelial tumor cells—a new method for the immunomorphological and molecular characterization of circulating tumor cells. Am J Pathol. 2000; 156(1):57–63
[172] Zheng S, et al. Membrane microfilter device for selective capture, electrolysis and genomic analysis of human circulating tumor cells. J Chromatogr A. 2007; 1162(2):154–161.
[173] Tan SJ, et al. Microdevice for the isolation and enumeration of cancer cells from blood. Biomed Microdevices. 2009; 11(4):883–892
[174] Tan SJ, et al. Versatile label free biochip for the detection of circulating tumor cells from peripheral blood in cancer patients. Biosens Bioelectron. 2010; 26(4):1701–1705
[175] Lecharpentier A, et al. Detection of circulating tumour cells with a hybrid (epithelial/ mesenchymal) phenotype in patients with metastatic non-small cell lung cancer. Br J Cancer. 2011; 105(9):1338–1341
[176] Dharmasiri U, et al. Microsystems for the capture of low-abundance cells. Annu Rev Anal Chem. 2010; 3:409–431
[177] Krivacic RT, et al. A rare-cell detector for cancer. Proc Natl Acad Sci USA. 2004; 101(29):10501–10504

[178] Zieglschmid V, Hollmann C, Bocher O. Detection of disseminated tumor cells in peripheral blood. Crit Rev Clin Lab Sci. 2005

[179] Racila E, et al. Detection and characterization of carcinoma cells in the blood. Proc Natl Acad Sci USA. 1998; 95(8):4589–4594

[180] Morgan TM, Lange PH, Vessella RL. Detection and characterization of circulating and disseminated prostate cancer cells. Front Biosci. 2007; 12:3000–3009

[181] Gupta V, Jafferji I, Garza M, Melnikova VO, Hasegawa DK, Pethig R, Davis DW. ApoStream(TM), a new dielectrophoretic device for antibody independent isolation and recovery of viable cancer cells from blood. Biomicrofluidics. 2012; 6: 24133.

[182] Whitesides GM. The 'right' size in nanobiotechnology. Nat Biotechnol. 2003; 21(10):1161–1165.

[183] Moore GE. Cramming more components onto integrated circuits. Electronics

[184] Reyes DR, et al. Micro total analysis systems. 1. Introduction, theory, and technology. Anal Chem. 2002; 74(12):2623–2636.

[185] Lee SJ, Lee SY. Micro total analysis system (μ-TAS) in biotechnology. Appl Microbiol Biotechnol. 2004; 64(3):289–299

[186] Hansen CL, et al. A robust and scalable microfluidic metering method that allows protein crystal growth by free interface diffusion. Proc Natl Acad Sci USA. 2002; 99(26):16531–16536.

[187] Kobayashi J, et al. A microfluidic device for conducting gas-liquid-solid hydrogenation reactions. Science. 2004; 304(5675):1305–1308

[188] Manz A, et al. Planar chips technology for miniaturization and integration of separation techniques into monitoring systems—capillary electrophoresis on a chip. J Chromatogr. 1992; 593(1–2):253–258.
[189] Sia SK, Whitesides GM. Microfluidic devices fabricated in poly(dimethylsiloxane) for biological studies. Electrophoresis. 2003; 24(21)
[190] Nguyen, N-T.; Wereley, Steven T. Fundamentals and Applications of Microfluidics. Artech House; Boston/London: 2002
[191] Manz A, Graber N, Widmer HM. Miniaturized total chemical analysis systems: a novel concept for chemical sensing. Sensors Actuators B1. 1990
[192] Wang ST, et al. Highly efficient capture of circulating tumor cells by using nano-structured silicon substrates with integrated chaotic micromixers. Angew Chem Int Ed. 2011; 50(13):3084–3088.
[193] Dharmasiri U, et al. High-throughput selection, enumeration, electrokinetic manipulation, and molecular profiling of low-abundance circulating tumor cells using a microfluidic system. Anal Chem. 2011; 83(6):2301–2309
[194] Zheng X, et al. A high-performance microsystem for isolating circulating tumor cells. Lab Chip. 2011; 11(19):3269–3276.
[195] Wang S, Owens GE, Tseng HR. Nano “fly paper” technology for the capture of circulating tumor cells. Methods Mol Biol. 2011; 726:141–150.
[196] Saliba et al. Microfluidic sorting and multimodal typing of cancer cells in self-assembled magnetic arrays. Proc Natl Acad Sci USA. 2010; 107(33):14524–14529.
[197] Mikolajczyk SD, et al. Detection of EpCAM-negative and cytokeratin-negative circulating tumor cells in peripheral blood. J Oncol. 2011; 2011:252361

[198] Hoshino K, et al. Microchip-based immunomagnetic detection of circulating tumor cells. Lab Chip. 2011; 11(20):3449–3457.

[199] Adams AA, et al. Highly efficient circulating tumor cell isolation from whole blood and label-free enumeration using polymer-based microfluidics with an integrated conductivity sensor. J Am Chem Soc. 2008; 130(27):8633–8641.

[200] Wang S, et al. Three-dimensional nanostructured substrates toward efficient capture of circulating tumor cells. Angew Chem Int Ed. 2009; 48(47):8970–8973

[201] D. Chen, H. Du, C. Yong Tay, Nanoscale Res Lett (2010) 5:55–60

[202] M. Sancho, G. Martinez, C. Martin, Journal of Electrostatics 57, (2003)

List of pubblications

- A. Magliano, M. Camarda, S. F. Lombardo, R. Di Martino, M. Cascio, A. Romano, L. Minafra, G. Russo, M. C. Gilardi, F. Di Raimondo, S. Scalese and A. La Magna,

  Elution time changes due to anomalous DEP effects in microchannels under uniform and non-uniform electric fields,

  Sensing and Bio-Sensing Research **8**, 59-64 (2016).

- R. Di Martino, M. Camarda, M. Cascio, Michele G., A. Magliano, S. Baldo, A. Romano, L.Minafra, G. I. Forte, G. Russo, M. C. Gilardi, F. Di Raimondo, S. Scalese and A. La Magna,

  Analysis of the role of elution buffers on the separation capabilities of dielectrophoretic devices,

  Sensing and Bio-Sensing Research **7**, 162-167 (2016).

- M. Cascio, G. Falci, S. F. Lombardo, A. Magliano, I. Deretzis, S. Scalese and A. La Magna,

  MD-FEM Force Field Simulations of Particle Subjected to Dielectrophoresis Interactions,

  https://www.simula.no/file/fenics17v2pdf/download (2017).

- A. La Magna, A. Alberti, E. Barbagiovanni, C. Bongiorno, M. Cascio, I. Deretzis, F. La Via, E. Smecca,

  Simulation of the growth kinetics in group IVcompound semiconductors

  Phys.S. Sol. a in press

- Michele Cascio, Davide Baroli, Stephane Bordas, Ioannis Deretzis, Giuseppe Falci, Antonino Magliano and Antonino La Magna,

  Coupled Molecular Dynamics and Finite Element Method simulations for the kinetics of particles subjected to field mediated forces,

  submitted to Physical Review E.

List of conference participations

Poster presentation

- **Materials 2016**, December 12-16, Acicastello, Italy

  Force field simulations of particle subjected to dielectrophoresis interactions.

  Michele Cascio, I. Dereztis, G. Falci, S.F. Lombardo, A. Magliano, S. Scalese and A. La Magna;

- **FEniCS 2017**, June 12-14, 2017, Luxembourg

  MD-FEM Force Field Simulations of Particle Subjected to Dielectrophoresis Interactions.

  Michele Cascio, G. Falci, S. F. Lombardo, A. Magliano, I. Deretzis, S. Scalese and A. La Magna

- **11th Italian Quantum Information Science conference 2018,** September 17-20, 2018, Catania, Italy;

  Coupled Molecular Dynamics and Finite Element Methods for the study of the evolution of large systems of electromechanical particles.

  M. Cascio, D. Baroli, G. Falci, I. Deretzis and A. La Magna

- **12th International Conference on Scientific Computing in Electrical Engineering**, September 23-27, 2018, Taormina, Italy

  MD-FEM Force Field Simulations of Particle Subjected to Dielectrophoresis Interactions.

  M. Cascio, G. Falci, S. F. Lombardo, I. Deretzis and A. La Magna;

- **Materials 2018**, October 22-26, Bologna, Italy;

  Coupled Molecular Dynamics and Finite Element Methods for the study of the evolution of large systems of electromechanical particles.

  Michele Cascio, G. Falci, S.F. Lombardo, I. Dereztis and A. La Magna.

Oral communication

- **2018 E-MRS Fall Meeting**, September 17-20, 2018, Varsavia, Poland;

  Atomistic simulations of the defects evolution during the growth of group IV crystals.

  M. Cascio, I. Deretzis, G. Falci and A. La Magna.

Acknowledgements

I would like to express my sincere gratitude to my tutors, Prof. Giuseppe Falci and Dr. Antonino La Magna, for their continuous support of my Ph.D. study and related research, and for always providing resourceful help, great knowledge, and interesting insights to physical phenomena.

Many thanks to Dr. Ioannis Deretzis for his help, suggestions and discussions.

Thank-you to Dr. Silvia Scalese for her support.

I would also like to acknowledge my Referee, Prof. G.G.N. Angilella, and the Coordinator, Prof. Vincenzo Bellini, for their attentive work.